Title
High-Performance Aluminum Nitride Lamb Wave Resonators for RF Front-End Technology

Author
Zou, Jie

Publication Date
2015

Peer reviewed|Thesis/dissertation

High-Performance Aluminum Nitride Lamb Wave Resonators for RF Front-End Technology

by

Jie Zou

A dissertation submitted in partial satisfaction of the

requirements for the degree of

Doctor of Philosophy

in

Engineering – Mechanical Engineering

in the

Graduate Division

of the

University of California, Berkeley

Committee in charge:

Professor Albert P. Pisano, Chair
Professor Liwei Lin
Professor Clark T.-C. Nguyen

Summer 2015

High-Performance Aluminum Nitride Lamb Wave Resonators and for RF Front-End Technology

By

Jie Zou

Abstract

High-Performance Aluminum Nitride Lamb Wave Resonators and for RF Front-End Technology

by

Jie Zou

Doctor of Philosophy in Mechanical Engineering

University of California, Berkeley

Professor Albert P. Pisano, Chair

The explosive development of wireless and mobile communication systems has continuously driven rapid technology innovation in component performance and system integration. In order to obtain faster signal processing and reduce integration complexity, the miniaturized and Complementary metal–oxide–semiconductor (CMOS) compatible micro-electromechanical system (MEMS) resonators are likely to be the driving core of a new generation of devices such as radio frequency (RF) filters and oscillators which are the main building blocks in the RF front-end. Thus, a high-performance MEMS resonator technology is highly in demand as the fundamental components in the RF front-end for an advanced wireless communication system.

Among various microelectromechanical resonator technologies, aluminum nitride (AlN) Lamb wave resonators (LWRs) have attracted great attention since it combines the advantages of surface acoustic wave (SAW) and bulk acoustic wave (BAW): the ability of high resonance frequency (f_s) and multi-frequency on a single chip. The AlN-based structure provides for CMOS compatibility, and the lowest order symmetric (S_0) Lamb wave mode exhibits high phase velocity up to 10000 m/s, weak phase velocity dispersion, small temperature coefficient of frequency (*TCF*), high quality factor (*Q*), and moderate electromechanical coupling coefficient (k^2). However, the performance parameters needs to be further improved to enable the low-loss filters and stable oscillators. This dissertation addresses a number of issues and demonstrated the high-performance (high-f_s., large-k^2, high-*Q*, low-*TCF*, and low-resonance impedance (Z_{min})) piezoelectric AlN LWRs to fulfill the technical requests for the RF front-end.

The k^2 and f_s optimization of the AlN LWR using the S_0 Lamb wave mode is achieved by choosing electrode materials and thicknesses for specific electrode configurations. This study adopts the finite element analysis (FEA) to investigate the influence of electrodes on the dispersive characteristics of the S_0 mode propagating in the multi-membranes. From the theoretical study, it is found that the phase velocity is directly related to the density (ρ) and equivalent phase velocity in the metal, while the coupling coefficients depend on ρ and acoustic impedance (*Z*) of the metal. Large-*Z*

material is preferred for the IDT and light material is favored for the bottom electrode to optimize the k^2. Thicker metal for the IDT loads the k^2 more when AlN is thin and enhance k^2 more when AlN is relatively thick.

In order to boost the *Q*, a new class of the AlN LWRs using butterfly-shaped plates is introduced in this dissertation for the first time. The butterfly-shape plates can effectively suppress the vibration in the tether location and reduce anchor loss. The 59˚ butterfly-shaped resonator enables an unloaded *Q* up to 4,758, showing a 1.42× enhancement over the conventional resonator. The experimental results are in good agreement with the simulated predictions by the 3D perfectly matched layer (PML)-based FEA model, confirming that the butterfly-shaped AlN thin plate can efficiently eliminate the anchor dissipation. What's more, by employing the butterfly-shape AlN plates with rounded tether-to-plate transition which has smaller tether-to-plate angle, the suppression in the anchor loss and enhancement in the *Q* is even more effective, which is also demonstrate by the simulations. The fabricated butterfly-shaped resonator with 45˚ beveled tether-to-plate transition yields a *Q* of 1,979 which upwards 30% over a conventional rectangular resonator; while another AlN LWR on the butterfly-shaped plate with rounded tether-to-plate transition yields a *Q* of 2,531, representing a 67% improvement. In addition, the butterfly-shaped plate didn't introduce spurious modes on a wide spectrum, compared to other *Q* increase techniques.

The *TCF* reduction along with the k^2 and f_s optimization is demonstrated by introducing the symmetrical SiO_2/AlN/SiO_2 sandwiched structure to replace the conventional temperature compensation structure AlN/SiO_2. The symmetrical SiO_2/AlN/SiO_2 sandwiched plate experiences the less temperature-induced bending deformation than the conventional AlN/SiO_2 bilayer plate when the operation temperature arises from room temperature to 600°C. The symmetrical SiO_2/AlN/SiO_2 sandwiched plate also enables the pure S_0 mode which shows the higher v_p and larger k^2 than the QS_0 mode in the AlN/SiO_2 bilayer plate. In the SiO2/AlN/SiO2 sandwiched membrane, the single IDT with the bottom electrode configuration offers a simple process flow and a large k^2 at the relatively thin h_{AlN} region ($h_{AlN} = 0.1\lambda$). The double-sided IDTs configuration provides a large k^2 up to 4% at the relatively thick hAlN region ($h_{AlN}/\lambda = 0.4\lambda$) even when the thick SiO_2 layers are employed for thermal compensation at high temperatures. Based on the correct choices of the AlN and SiO2 thicknesses in the symmetrical SiO_2/AlN/SiO_2 sandwiched membrane, the LWRs can be thermally stable and retain a large k^2 at high temperatures.

The low-Z_{min} and high-f_s AlN LWR is studied by utilizing the first order symmetric (S_1) mode propagating in a specific thickness of AlN. In order to achieve the larger electromechanical coupling coefficient and high phase velocity as well as avoid the negative group velocity in the S_1 Lamb wave mode, the 4-μm-thick AlN layer and 3-μm-wide finger electrodes are employed in the Lamb wave resonator design. The experimental results show the S_1 mode presents a Z_{min} of 94 Ω at 1.34 GHz, lower than the Z_{min} equal to 224 Ω of the S_0 mode at 878.3 MHz.

To my parents and Pucong.

LIST OF ABBREVIATIONS

AC	Alternating Current
Al	Aluminum
AlN	Aluminum Nitride
Au	Gold
BAW	Bulk Acoustic Wave
BCC	Body-Centered Cubic
BE	Bottom Electrode
BVD	Butterworth-Van Dyke
C	Capacitor
C_m	Motional Capacitor
CMOS	Complementary Metal-Oxide Semiconductor
Cr	Chromium
Cu	Copper
DC	Direct Current
f_s	Series Resonance Frequency
f_p	Parallel Resonance Frequency
FBAR	Film Bulk Acoustic Resonator
FCC	Face-Centered Cubic
FEA	Finite Element Analysis
FPAR	Film Plate Acoustic Resonator
GaN	Gallium Nitride
GHz	Gigahertz
GSM	Global System for Mobile Communications
IDT	Interdigital Transducer
IF	Intermediate Frequency
Ir	Irridium
kHz	Kilohertz
L	Inductor
LFE	Lateral-Field-Excited
LGS	Langasite

$LiNbO_3$	Lithium Niobate
$LiTaO_3$	Lithium Tantalate
L_m	Motional Inductor
LFE	Lateral Field Excitation
LNA	Low Noise Amplifier
LPCVD	Low Pressure Chemical Vapor Deposition
LSN	Low Stress Nitride
LTO	Low Temperature Oxide
LWR	Lamb Wave Resonator
MBVD	Modified Butterworth-Van Dyke
MEMS	Microelectromechanical systems
MHz	Megahertz
Mo	Molybdenum
MOCVD	Metal Organic Chemical Vapor Deposition
OCXO	Oven-Controlled Crystal Oscillator
PECVD	Plasma Enhanced Chemical Vapor Deposition
PML	Perfectly Matched Layer
ppm	Parts-Per-Million
Pt	Platinum
PZT	Lead Zirconium Titanate
Q	Quality Factor
R	Resistor
R_m	Motional Resistor
RF	Radio Frequency
Ru	Ruthenium
Rx	Receiver
SAW	Surface Acoustic Wave
SDR	Software Defined Radio
SEM	Scanning Electron Micrograph
SiO_2	Silicon Dioxide
SiOF	Fluorine-Doped Silicon Oxide

SMR	Solidly Mounted Resonator
TCE	Temperature Coefficient of Elasticity
TCF	Temperature Coefficient of Frequency
TCXO	Temperature-Compensated Crystal Oscillator
TE	Thickness Extension
TeO_2	Tellurium Dioxide
TFE	Thickness-Field-Excited
Ti	Titanium
Tx	Transmitter
UHF	Ultra High Frequency
VCXO	Voltage-Controlled Crystal Oscillator
VHF	Very High Frequency
W	Tungsten
XO	Crystal Oscillator
ZnO	Zinc Oxide

ACKNOWLEDGEMENTS

First and foremost, I would like to express my deepest appreciation to my advisor, Prof. Albert P. Pisano. He gave me insightful suggestions in the research direction and large freedom to follow my own interest. He also gave me complete support and every opportunity in keep trying experiments and attending conferences to discuss with other researchers in the field. He is so warm and humorous that everybody likes him. His insights and personality are an excellent example of a great scientist and a great leader, and will benefit my whole life.

I give my sincerest gratitude to Professor Clark T.-C. Nguyen for agree being reader of this research report. I always admire his research on MEMS, analog circuits and RF communication. This report is also motivated from the theory he put forward. I would also like to express my sincere gratitude to Professor Liwei Lin, Prof. Richard M. White and Prof. Tsu-Jae King Liu for their valuable technical suggestions on this work.

I own my heartfelt appreciation to Dr. Chih-Ming Lin for his professional guidance on the AlN Lamb wave resonators, teaching me nanofabrication and all the invaluable discussions. It was great joy to work in the Pisano Research for Integrated Micromechanical & Electrical (PRIME) Systems Laboratory and I remain indebted to my former and current colleagues, Dr. Debbie Senesky and Dr. Jim C. Cheng, Dr. Ayden Maralani, Dr. Kristen Dorsey, Dr. Mitsutoshi Makihata, Dr. Nuo Zhang, Dr. Matilda Yun-Ju Lai, Dr. Fabian Goericke, Dr. Wei-Cheng Lien, Dr. Earnest Ting-Ta Yen, Dr. Matthew Chan, Dr. Sarah Wodin-Schwartz, Dr. Yegân Erdem, Kirti Mansukhani, Hongyun So, Anju Toor, Lilla Smith, Shiqian Shao, David Rolfe, Gordon Hoople, Maria Pace, Joy Xiaoyue Jiang, Levent Beker Ben Eovino, and John Herr for all the helpful discussions and your support.

All devices studied in this report were fabricated at the Berkeley Marvell Nanofabrication Laboratory. I would like to thank all Nanolab staff for assisting me through these years.
At the same time, I wish to thank Ruonan Liu, Hanyu Zhu, Zeying Ren, Xianling Liu, Chuang Qian, Bo Lv, Yang Yang, Yuping Zeng, and Zheng Cheng for giving me invaluable help and suggestions on MEMS fabrication.

Outside the academic environment, I would like to thank Yifan Jiang, Jun Xie, Wenwen Jiang, Weixi Zhong, Minghui Zheng, Meng Cai, Xuance Zhou, Siyuan Xin, Chang Liu, Ming Tin, Junkai Lu, Bo Xu, Fan Yang, Qianyi Li, and Qi Wang. With their company in the United States, I have a wonderful and enjoyable life outside the work environment.

Last but not the least, I owe more than words can describe to my parents and my fiancé, Guanbin Zou, Fenglian Zeng and Pucong Han, for their never ending love and unequivocal dedication. I reserve my sincere gratitude to your patience, your companionship, and your steadfast encouragement.

TABLE OF CONTENTS

Chapter 1

Introduction

Microelectromechanical systems (MEMS), inspired by microelectronics and benefited from the development of microfabrication technology, have been recently intensively researched and successfully commercialized in many fields of technology. The conventional MEMS technology which converts energy from mechanical to electrical domain or vice versa - sensors and actuators, play an irreplaceable role in people's modern life and are offered by many suppliers today. In contrast to their unique function, radio frequency microelectromechanical systems (RF MEMS) process electrical signal just like electronics using mechanically vibrating structure, and have replaced on-chip electrical RF devices to provide frequency control functions due to their extraordinary performance compared to on-chip electrical counterparts. With small size, high performance and Complementary metal–oxide–semiconductor (CMOS) compatibility, RF MEMS resonators offer promising building blocks for frequency control and timing reference in contemporary RF front-end in wireless communication systems.

This chapter starts by introducing the potential application of MEMS resonators in band-pass filters and oscillators in the current RF front-end transceivers and novel reconfigurable channel-select RF front-end architectures. Technical requirements for MEMS resonators will be summarized followed by short descriptions of existing MEMS resonator technologies.

1.1 MEMS Resonators for RF Front-End Technology

1.1.1 Current and Future RF Front-End Transceivers

Modern RF front-end architectures for wireless communication are mainly based on super-heterodyne and direct conversion approaches. The super-heterodyne or heterodyne receiver is the most widely and extensively used reception technique for a long time. The direct conversion receiver was impractical around the time of its invention (1930's) but recently resurrected for its intriguing qualities such as low power, small form factor, low cost and reduced bill of materials especially for mobile communications.

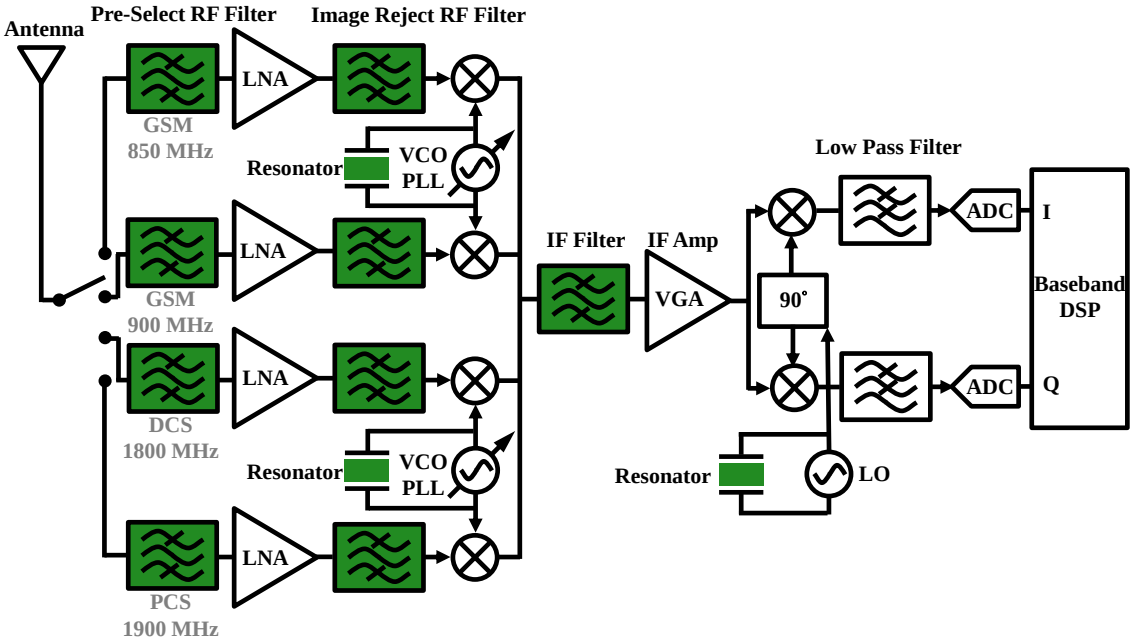

Figure 1-1. System block diagram of a quad-band super-heterodyne receiver (potential MEMS resonator replacements are shaded).

In the super-heterodyne architecture, the RF signal is first amplified in a frequency selective low noise stage, then translated to a lower intermediate frequency (IF) with significant amplification and additional filtering, and finally down-converted to baseband with either a phase discriminator or straight mixer. Figure 1–1 shows a system block diagram of a state-of-art quad-band super-heterodyne receiver (Rx) architecture applicable to RF front-end in cellular phones. The off-chip bulky filters and quartz crystal resonators are the main components for frequency selection and time reference.

The direct conversion approach, also known as homodyne, or zero-IF, is the most natural solution to receiving information transmitted by a carrier, which mixes the RF carrier frequency directly to the baseband. Direct conversion reception is very suitable for integration as well as multi-band, multi-standard operation. This approach eliminates the use of bulky IF SAW filters and thus offers size miniaturization and reduction of components [1]-[3]. However, the direct conversion architecture still needs the use of the off-chip bulky RF filters and oscillators, and the strong requirements for band integration has increased the number of filters in a handset tremendously. For example, the Black Berry in 2010 has 3 Duplexers, 4 Global System for Mobile Communications (GSM) filters, 6 point filter, comparing to 2 filters in 1990s.

With the development of MEMS technology, mechanical vibrating structures used for frequency control and time keeping can be fabricated on Si wafers with excellent performance, tiny size, low power consumption, and CMOS compatibility [4]-[8]. In order to reduce complexity of integration, cost and power consumption in next-generation communication systems, CMOS compatible MEMS resonators are considered as direct

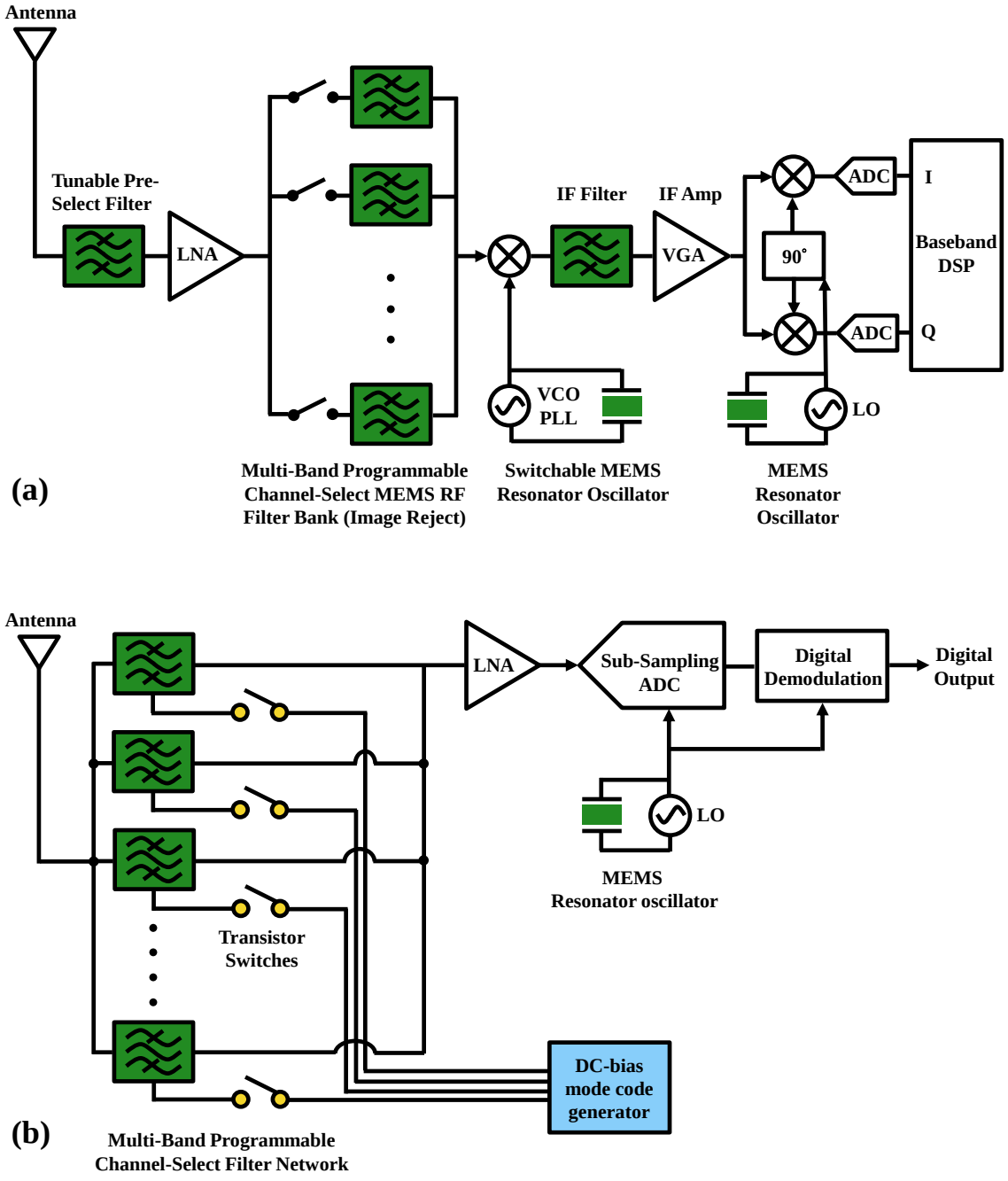

Figure 1-2. System block diagrams for (a) a channel-select receiver architecture using integrated MEMS filter bank and resonators, and (b) a highly-reconfigurable, low-power SDR front-end receiver utilizing a network of large numbers of MEMS RF filters to realize a frequency gating function. (RF MEMS devices are shaded in green).

replacements of these discrete components. As is indicated in the shaded area in Figure 1-1, the receiver front-end architecture can adapt MEMS resonator technology to realize a highly integrated system [9]-[15].

In addition, novel RF frond-end channel-select architecture is proposed by Nguyen to use the high *Q* MEMS resonator technology to eliminate the use of the RF low noise amplifiers (LNAs) and transistor mixers, thereby significantly reduce the complexity of integrated circuit (IC) and lower the power consumption [16]. In the circuit of Figure 1–2 (a), the key feature of the RF channel-select architecture is the closely spaced filter bank paired with low loss switched to eliminate not only out-of-band interferers but also out of channel interferers [17]. For a narrowband filter, the insertion loss heavily depends on the resonator *Q* while a small percent bandwidth is needed [18], [19].

One step further, as the increasing desire for reconfigurable radios capable of adapting to any communication standard has spurred great interest in the concept of a software defined radio (SDR), Nguyen pointed out that MEMS devices can be used in massive numbers as the way of transistors in 2008. He put forward the software defined radio front-end utilizing a micromechanical RF channel-select filter network to realize a frequency gating function, as is shown in Figure 1-2 (b). Large numbers (>100) of switchable MEMS filters are used to realize the programmable frequency gate instead of restricting the implementation of a programmable frequency gate to a single tunable filter.

All the above information reveals that CMOS compatible, high-*Q*, large-coupling coefficient, thermally stable and small-resonance-impedance micromechanical resonators are essential to construct single-chip transceiver in the near future and the highly configurable SDR front-end in the long run.

1.1.2 Resonator Performance Parameters

Before talking about specific applications, a brief introduction to the general parameters of a resonator is given here. As shown in Figure 1-3, a typical frequency response of the admittance has a resonance and an anti-resonance peak, and the definitions of important parameters are listed below:

The Series Resonance Frequency, f_s

The series resonance occurs at frequency when the impedance value of the resonator shows a pronounced minimum and an electrical phase of zero degrees:

$$f_s = f(Z_{\min}, or\ Y_{\max}) = f(\phi = 0°). \tag{1.1}$$

The Quality Factor, *Q*

The quality factor is a measure for what fraction of the stored energy is lost per resonance cycle. It characterizes the sharpness of the resonance peak and is usually defined by the ration of the 3dB bandwidth to the resonance frequency:

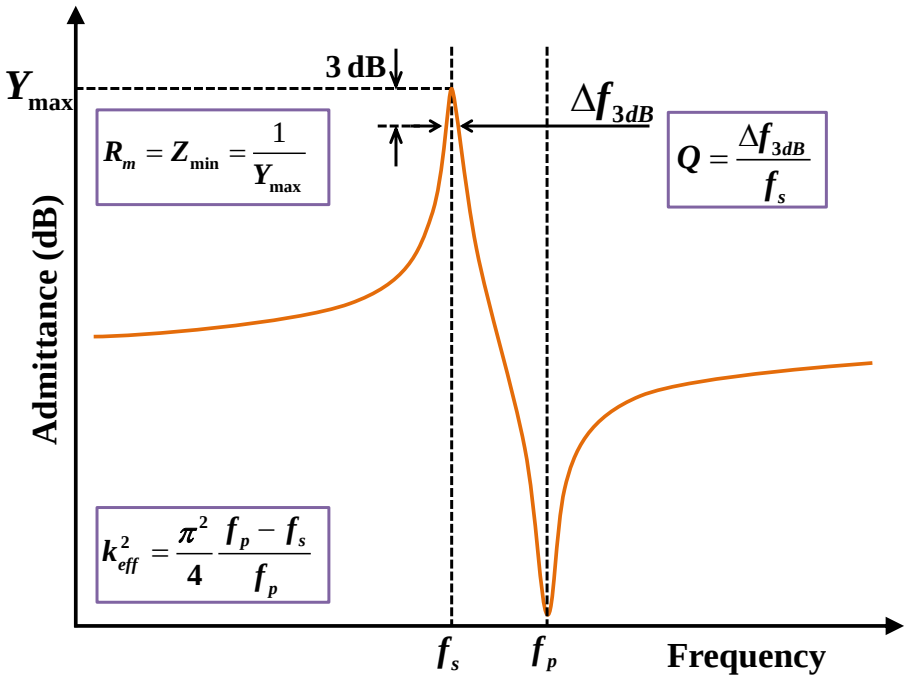

Figure 1-3. A typical frequency response of a resonator with definitions of important parameters.

$$Q = \frac{\Delta f_{3dB}}{f_s}. \tag{1.2}$$

The Effective Coupling Coefficient, k^2_{eff}

The coupling coefficient is a measure for the efficiency of a resonator to convert electrical to mechanical energy and vice versa. Higher k^2_{eff} enables filters with a wider relative bandwidth. It is usually defined by the distance between the resonance and anti-resonance peaks:

$$k^2_{eff} = \frac{\pi^2}{4}\frac{f_p - f_s}{f_p}. \tag{1.3}$$

The Motional Impedance, R_{m}

The motional impedance represents the loss level when the device is in resonance. A small R_{m} is usually highly desirable to enable low-insertion-loss filters and low-phase-noise oscillators, and can be achieved by increasing the Q and k^2_{eff}. It is usually about the same as the resonance impedance (Z_{min}) when the electrode resistance is ignored:

$$R_m = Z_{\min} = \frac{1}{Y_{\max}}. \tag{1.4}$$

The Temperature Coefficient of Frequency, *TCF*

The temperature coefficient of frequency (*TCF*) represents the relative shift in frequency over temperature for a resonator, usually stated in ppm/K or ppm/℃:

$$TCF = \frac{df}{dT}\frac{1}{f}. \tag{1.5}$$

More introductions of these important parameters will be given in detail in the later chapters when analyzing specific ones. The other key parameters for a resonator include power handling ability and nonlinearity, spurious modes levels, the size, CMOS compatibility, the easiness for manufacture, the easiness for frequency trimming, and so forth.

1.1.3 Frequency Selection Techniques

Passive LC Filters

Since the inductor *Q*-values rarely exceed 50, leading to high losses, making it impossible to realize steep transitions and low-loss. The size for LC filters at radio frequency range is also extremely large compared to other type of filters.

Active Filters

Active filters have large noise-figure, high intermodulation, high current drain, so they are not useful near antenna. Also, above 20 MHz or so, most commercial-grade operational amplifiers have insufficient open-loop gain for the average active filter requirement, and the cost increase to make active filters at high frequencies.

Electromagnetic Filters

Since these types of filters are based on electromagnetic waves, they tend to be very large below 3GHz and not applicable to portable devices.

MEMS Resonator Filters

In the MEMS resonator filters, energy conversion back and forth between electrical and mechanical energy is very efficient in piezoelectric materials. Acoustic waves represents electrical signal. Acoustic waves have relatively slow velocity, short

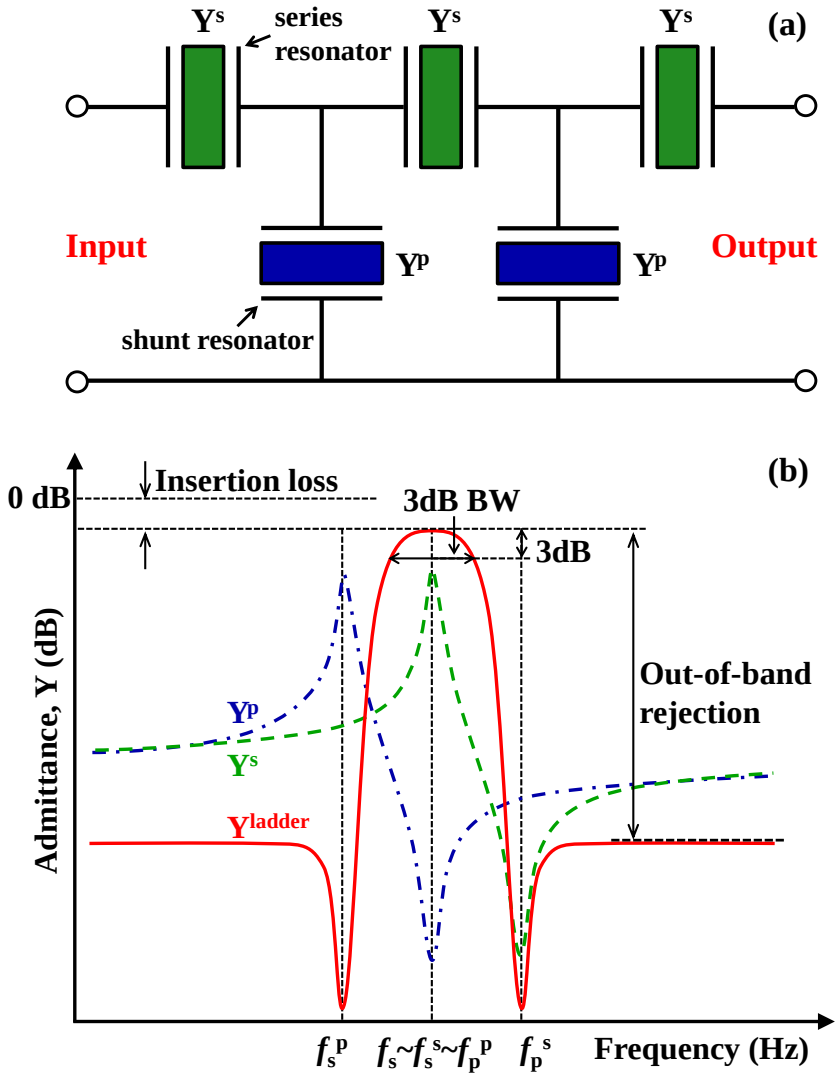

Figure 1-4. (a) Simple ladder filter with micromechanical resonators in the series and shunt branches and (b) the typical frequency spectrum of the synthesized ladder filter and common parameters for evaluating the filter.

wavelength, so small filters, making this type of filter especially applicable to RF front-ends.

In the front-end of wireless communication systems, band-pass filters are used to block out the unwanted signals. Figure 1–4 (a) shows a common electrically coupled filter, a ladder filter configuration, employing resonators in both series and shunt branches [1]-[3], [20]. All the resonators in the series branch have the same series and parallel resonance frequencies (f_s and f_p). Similarly, the resonators in the shunt branch have the identical series resonance frequency differing from the series resonance frequency of the resonators in the series branch.

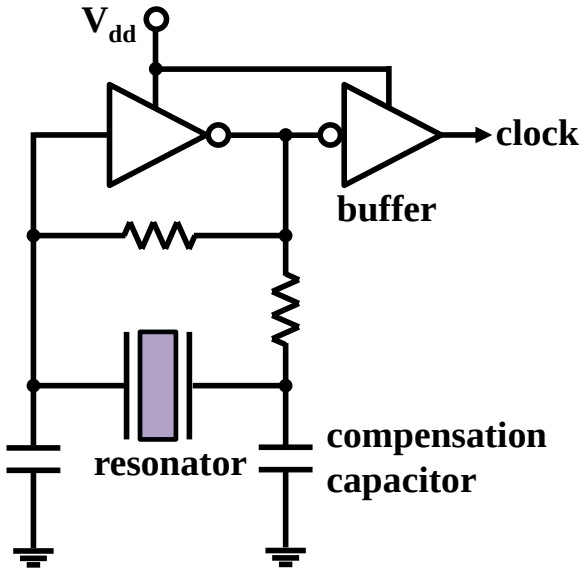

Figure 1-5. Simple illustration of a Pierce oscillator using crystal or ceramic resonators.

A typical frequency response of the ladder filter is shown in Figure 1–4 (b). Of special interest are the in-band insertion loss, 3dB bandwidth (BW), out-of-band rejection, the skirts, and the shape factor. As is indicated in Figure 1-4 (b), the 3dB BW is usually set by the effective coupling coefficient (k_{eff}^2) of the series and shunt resonators. To minimize the insertion loss of the ladder filter, the shunt resonators should have high Q and large impedance at their parallel resonance frequency f_p^p and the series resonators have high Q and low impedance at their series resonance frequency f_s.

1.1.4 Frequency References

Time references are employed in almost all electronic systems to keep track of real time and set precise clock frequency for digital data transmission. There are electrical and mechanical reference oscillators. In the electrical reference oscillators, the RLC frequency elements are integrated on the chip and comprise a network for clocking, logic, or frequency synthesizer applications [15]. In the mechanical reference oscillators, the mechanical vibrating devices are used as frequency elements to provide the stable natural resonance frequencies and the vibrating element is usually quartz resonators since it intrinsically exhibits a high Q and ultra-low TCF. The quartz crystal oscillator has dominated the market and been widely used in many electronic systems for decades.

As shown in Figure 1–5, a simple Pierce mechanical oscillator consists of a mechanical vibrating resonator, a positive feedback transistor, and an output buffer amplifier. The oscillator circuit locks oscillation by taking a voltage signal from the resonator, amplifying it, and then feeding it back to the resonator. So for the employed resonator the low loss (high Q) and temperature stability (low TCF) are of special importance for this application.

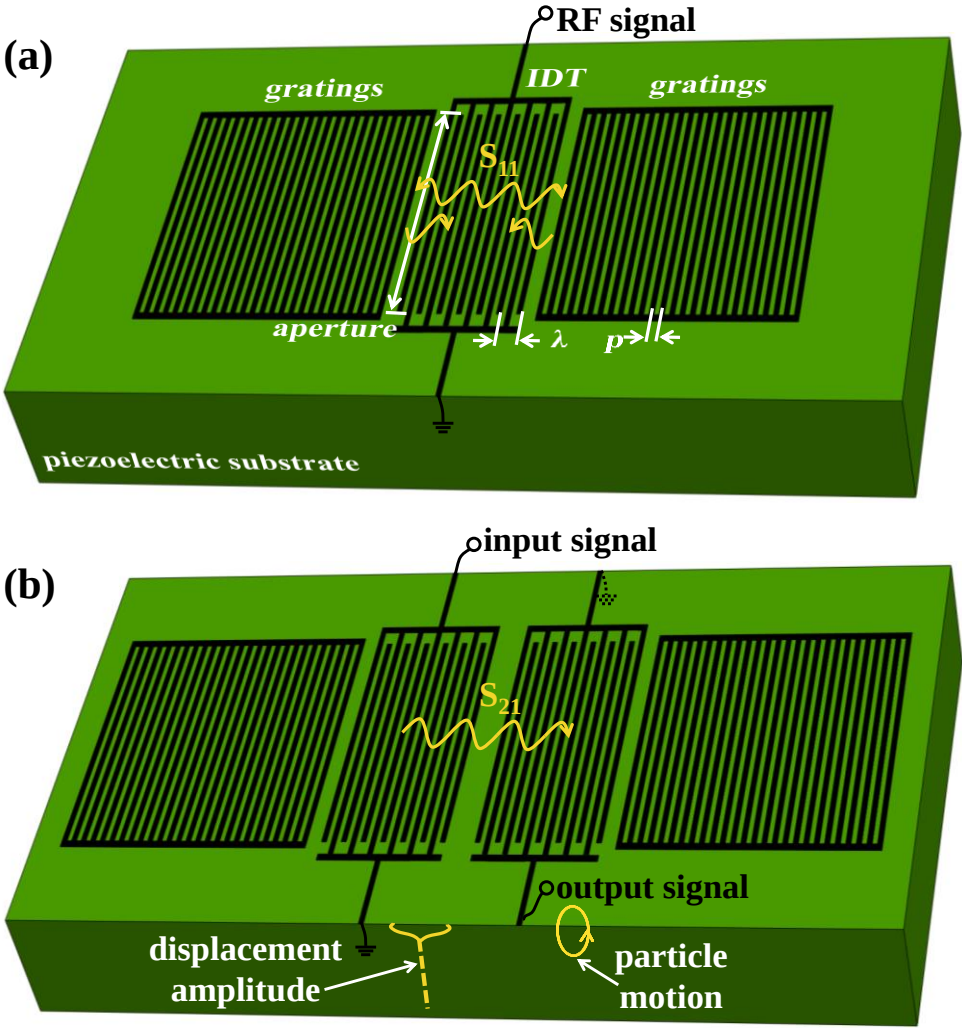

Figure 1-6. Illustration of (a) one-port and (b) two-port SAW resonators.

To summarize, high *Q* is a universally highly desirable property in the MEMS resonators for RF front-end applications to further enable low-loss and stable filters and low-phase-noise oscillators. Besides that, large k_{eff}^2, low R_m, ability of high frequency are special important technical challenges for filters and low *TCF*, impedance matching and capability of high frequency are essential for oscillator applications.

1.2 MEMS Resonators

MEMS resonators can be sorted into piezoelectric and capacitive transduced ones. Generally, the piezoelectric MEMS resonators tend to show a large coupling coefficient and the capacitive resonators have a super high *Q* but a small coupling coefficient. We will introduce the piezoelectric resonators in detail here: the Surface acoustic wave (SAW)

resonator, the Bulk acoustic wave (BAW) resonator, and the Lamb wave resonator (LWR), and then a brief introduction to the capacitive resonators.

1.2.1 Surface Acoustic Wave (SAW) Resonator

SAW resonators have been dominating the market for RF filters for several decades. A lot of research has been done in the 19th and 20th centuries after Rayleigh discovered surface acoustic waves propagating in solids in 1885 [21]. Although it remained a scientific curiosity with very few applications for a long time, the direct generation and detection of surface elastic waves through the piezoelectric effect led to a breakthrough in SAW devices after the invention of an interdigital transducer (IDT) by White and Voltmer in 1965 [22]. An intermediate frequency (IF) bandpass filter for television receivers was first developed and put into application as early as 1970s [23]. SAW devices have been widely used as IF and RF filters in wireless transmission systems for several decades because of their small size, low cost, and great performance.

Figure 1-6 shows the schematic of one-port and two-port SAW resonators composed from piezoelectric substrate, IDT pairs, and gratings. The IDT finger width is usually equal to quarter wavelength ($\lambda/4$) so the interdigital electrode pitch (p) as well as the grating period equal half wavelength ($\lambda/2$). SAWs can be generated by applying RF signals to the IDT and propagate on the surface of the substrate along the direction perpendicular to the fingers. The generated SAWs would be reflected by the gratings at both sides to reduce the energy loss.

The most severe limitation for SAW devices is that they can hardly achieve frequencies above 2.5 GHz. SAW phase velocities of common piezoelectric substrates, such as quartz, $LiNbO_3$, and $LiTaO_3$, are below 4,000 m/s, and the optical lithography today can only achieve 0.25um line-width. Even when the frequency approaches 2 GHz, the shrinkage of the IDT comb-fingers makes SAW resonators vulnerable to electrostatic discharge. Therefore, the Q factor is typically lower than 400. What's more, the required piezoelectric substrate is not compatible with standard microelectronic manufacturing.

1.2.2 Bulk Acoustic Resonator (BAW)

BAW resonators utilize the acoustic waves propagating through the bulk of a material, including longitudinal wave, shear horizontal (SH) wave, and shear vertical (SV) wave. The longitudinal acoustic wave is also called P-wave (primary wave) and has the highest phase velocity. BAW resonators mostly utilize the longitudinal mode or the thickness shear mode.

A thin-film BAW resonator is a device composed mainly from a piezoelectric thin film surrounded by two metal electrodes that generate the longitudinal wave propagating according to a thickness extension mode (TE). There are mainly two ways for the wave to be trapped in the resonator, which differentiates the two types of devices that have

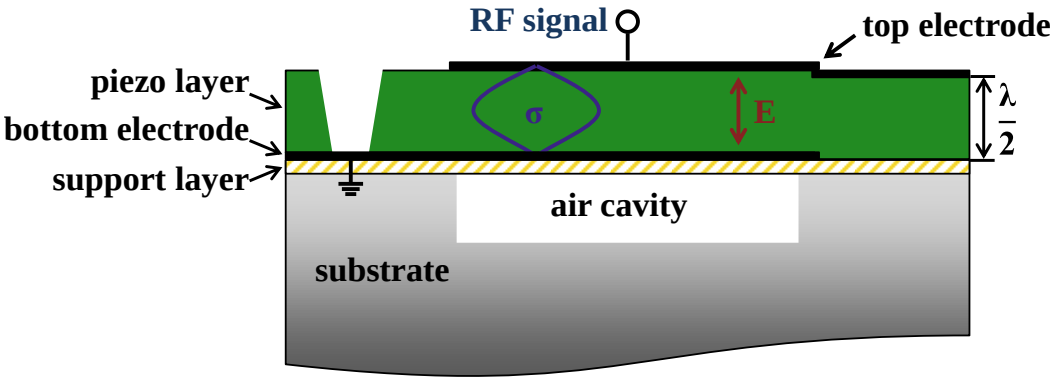

Figure 1-7. Illustration of the cross section of a simple FBAR.

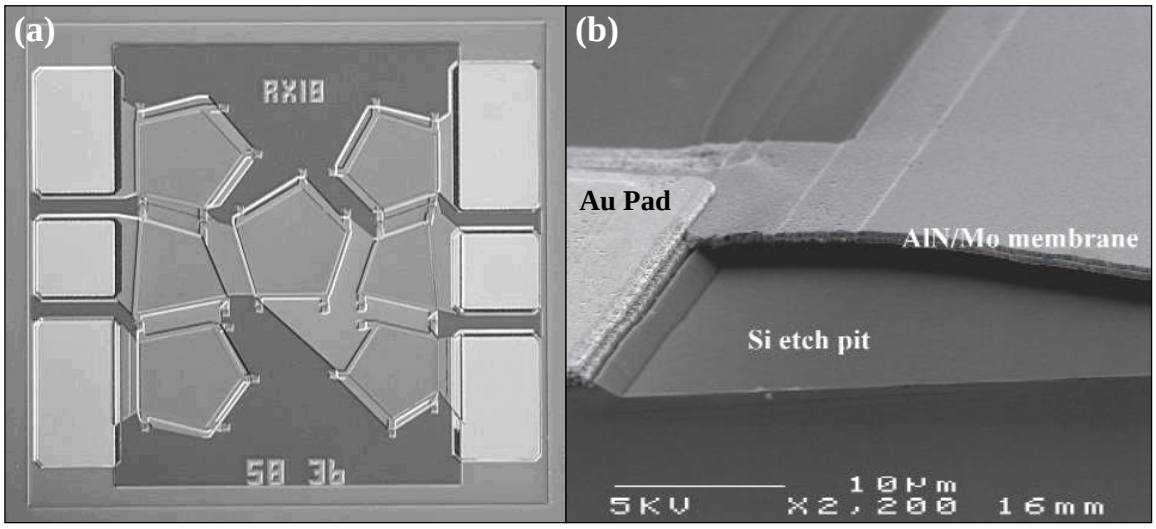

Figure 1-8. (a) A top view of a filter composed of three series and four shunt FBARs [24] and (b) the side view of the AIN membrane stretching over a micro-machined silicon pit [25].

reached volume manufacturing today: the Film Bulk Acoustic Resonator (FBAR) and Solidly Mounted Resonator (SMR).

Film Bulk Acoustic Resonator (FBAR)

As is shown in Figure 1-7, the FBAR is a free-standing piezoelectric membrane sandwiched between top and bottom electrodes. It uses air-solid interfaces both over and underneath the resonating film, and the air gap enables a high reflectance of the acoustic waves and thus a high *Q*. It can be manufactured over a sacrificial layer, released through isotropic etching, or by etching part of the substrate underneath the resonator. Common applications using FBAR technology are filters and duplexers at 1.9 GHz for cellular phones.

Figure 1-8(a) shows the top view of a filter composed of three series and four shunt FBARs and Figure 1-8(b) shows the side view of the AIN membrane stretching over a

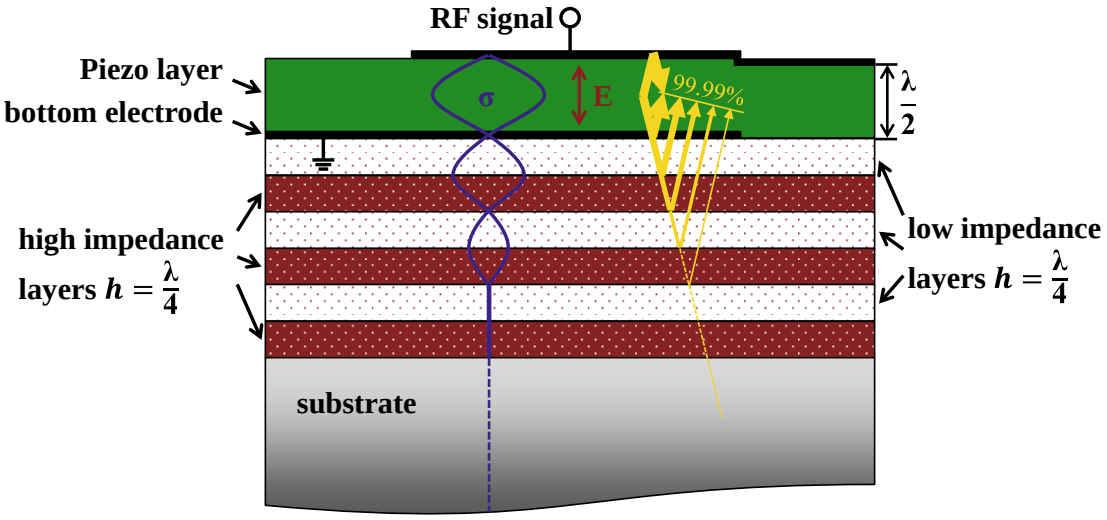

Figure 1-9. Schematic of the cross section view of a SMR.

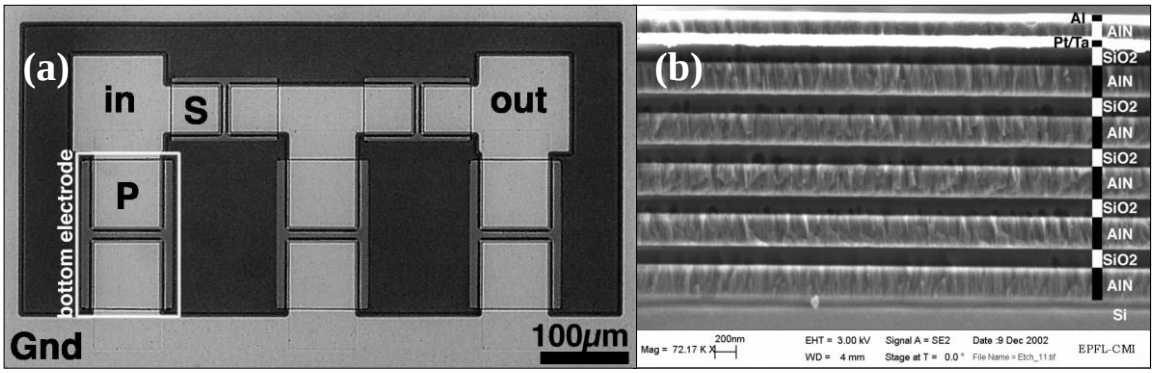

Figure 1-10. (a)Top view of a 2-stage π ladder filter and the (b) cross-section view of five reflector stacks of the SMR [26].

micro-machined silicon pit.

Solidly Mounted Resonator (SMR)

The SMR is a more robust structure where the top interface is also of the air-solid type, but solidly mounted to the substrate using a Bragg reflector stack, as is shown in Figure 1-9. An efficient isolation is performed by a set of quarter-wavelength sections of materials with different acoustic impedance, called the Bragg reflector [27]. The Bragg reflector diminishes the acoustic wave amplitude with the depth into itself [28], [29]. The larger the difference, the more efficient is the reflection. For example, the use of AlN and silicon dioxide (SiO_2) requires at least nine alternating layers, whereas replacing AlN by tungsten (W) allows this number to be reduced down to five as W has relatively high acoustic impedance. This non-free-standing structure provides physical robustness and good power handling capability.

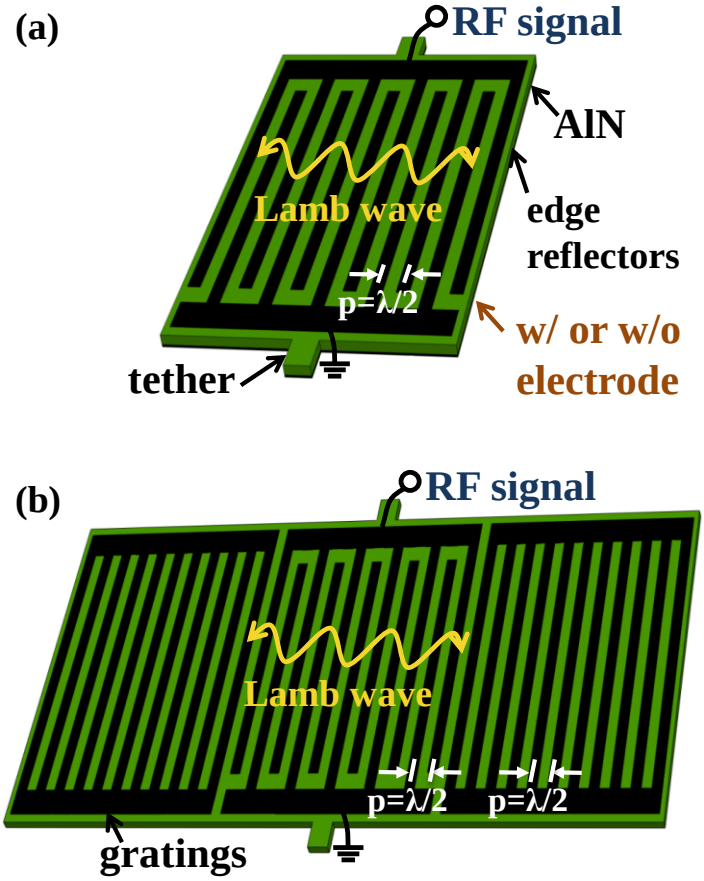

Figure 1-11. Schematic of one-port Lamb wave resonators with (a) edge type reflectors and (b) grating reflectors.

The top view and cross-section view of a 2-stage π ladder filter based on five reflector stacks of the SMR are shown in Figure 1-10.

1.2.3 Lamb Wave Resonator (LWR)

In 1973, Toda first demonstrated a Lamb wave device using PZT [30]. Then, the lowest-order antisymmetric (A_0) Lamb wave mode propagation in ZnO thin plate was widely studied for the liquid mass and density sensing, [31] since the A_0 mode has lower phase velocity than the compressional wave in most liquids and thus the A_0 Lamb wave cannot radiate energy into the surrounding liquid [32].

Recently, AlN Lamb wave resonator (Contour mode resonator) technology was brought up by Piazza and Yantchev since 2005 [35], [46]. Ever since, AlN Lamb wave resonators have attracted great attention for the designs of micro-acoustic resonators since it combines the advantages of BAW and SAW. The structure of Lamb wave resonator combines SAW resonator and FBAR, so it enjoys both advantages from these two mature technologies: it is transduced by IDTs so the frequency is lithography

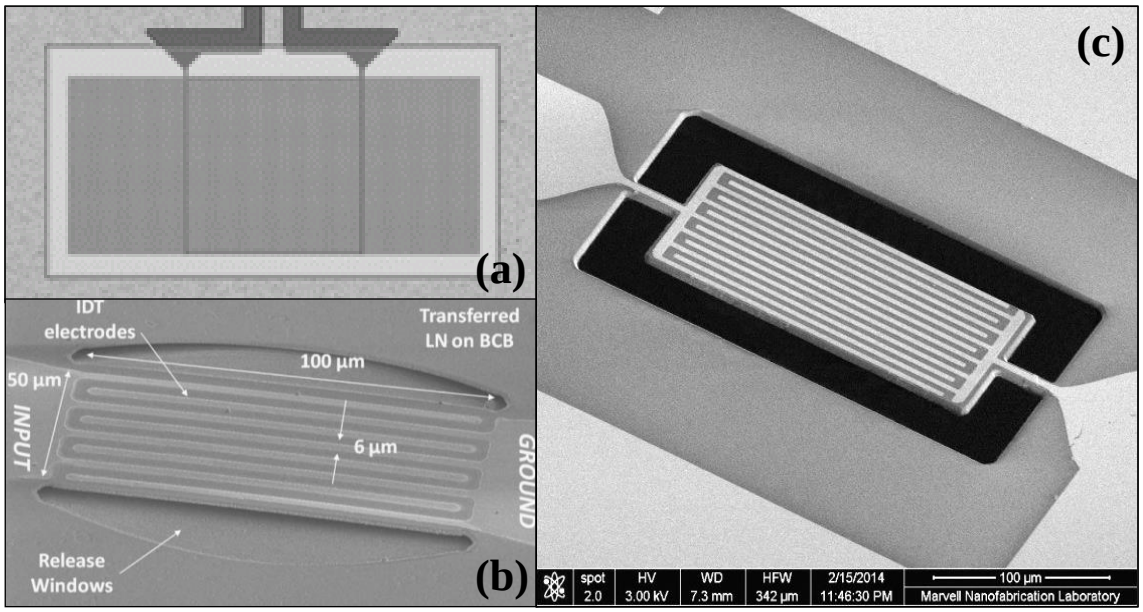

Figure 1-12. Lamb wave resonators (a) with reflectors [6] , (b) using edge reflectors on $LiNbO_3$ [33] and on (c) AlN membranes [34].

defined; the suspended structure enables a higher *Q* and larger phase velocity. What's more, AlN process technology can be CMOS compatible and can employ the maturity developed for FBAR and SMR. From the acoustic perspective, the lowest-order symmetric (S_0) Lamb wave mode in an AlN thin plate exhibits its phase velocity close to 10,000 m/s, a low dispersive phase velocity characteristic, and a moderate electromechanical coupling coefficient [35]-[45]. That is to say, the AlN LWRs are able to solve the low resonance frequency limitation and integration problem faced by SAW resonators, and the multiple frequency capability problem faced by piezoelectric BAW resonators.

As shown in Figure 1-11(a), a conventional Lamb wave resonator usually consists of one IDT with two suspended flat edges employed as the acoustic wave reflectors [39]-[47]. If the periodic gratings are used as the reflector to reflect Lamb wave in the thin plate, as shown in Figure 1-11(b) the grating number is usually more than 50 electrodes in order to have effective reflection of the periodic gratings. So the resonators using gratings are usually large [35]-[38]. Although Lamb wave has mode conversion upon the reflection at the free edges, the fundamental Lamb wave modes (A_0 and S_0 modes) mostly used in Lamb wave resonators do not have this problem at the suspended free edges [48], [49]. Therefore, the free edges are widely chosen as the reflectors since they make a smaller device in contrast to using the gratings. Lamb wave modes are generated by IDTs and then propagate in the AlN thin plate until reflection at both sides.

The Lamb wave resonators usually have the IDT electrodes on top of the AlN layer, and can be with or without the bottom electrodes. Different electrode configurations and the effects will be discussed in detail in Chapter 3, and how to choose the electrode materials and thicknesses will be analyzed in Chapter 4.

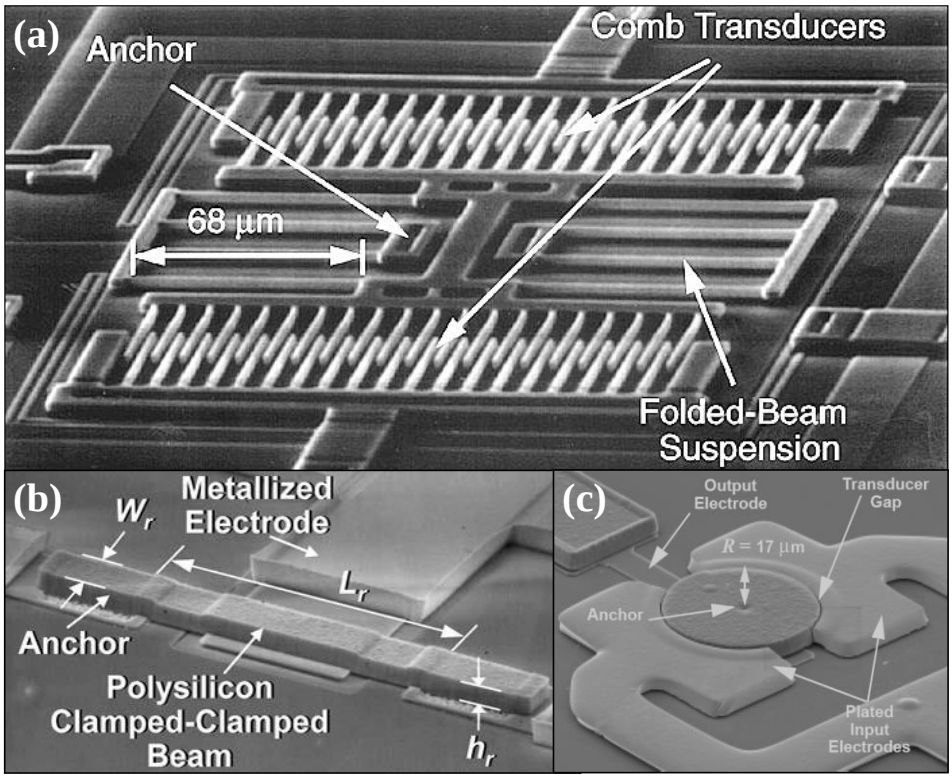

Figure 1-13. SEM image of (a) a capacitively transduced comb-drive resonator [51], (b) a poly-Si clamped-clamped beam flexural-mode resonator [52], and (c) an electrostatic disk micromechanical resonator [54].

Lamb wave resonators based on other materials other than AlN are also studied recently, like the $LiNbO_3$ and GaN. $LiNbO_3$ is a piezoelectric material that exhibits stronger piezoelectric effects than AlN, leading to higher coupling coefficients that can potentially enable ultra wide-BW filters. However, they are difficult to deposit directly and are usually implemented by micromachining. GaN Lamb wave devices are mostly for sensor applications and not much used for RF frequency selection since GaN has small piezoelectric constants.

As presented in Figure 1–12 (a), one topology of the LWR is based on the reflection from periodic grating reflectors like used in SAW devices. The topology based on the reflection from suspended free edges of the thin plate as depicted in Figure 1–12 (b).and (c), where (b) shows LWR based on transferred $LiNbO_3$ film and (c) presents LWR based on sputtered AlN film and released by XeF_2.

1.2.4 Electrostatic Resonators

The capacitively transduced electrostatic resonators are driven by parallel-plate electrostatic forces using various micromechanical structures, like cantilevers or

clamped-clamped beams [4], [50]. The first electrostatic vibrating comb-driven resonator on poly crystalline was reported by Tang *et al.* in 1989 [51]. As shown in Figure 1–13 (a), the capacitive-comb transduced resonator consists of a finger-supporting shuttle mass suspended above the substrate by folded flexures, which are anchored to a ground plane on the substrate. The resonance frequency of the comb-drive vibrating resonator is determined by material properties and lateral geometries [51], [53]. However, the resonance frequency of the vibrating comb-drive resonator is usually below 1 MHz due to the low spring constant of the long folded beam structure. In 2000, as shown in Figure 1–13 (b), Clark *et al.* proposed a new micromechanically vibrating disk resonator. Based on the radial contour mode, the micromechanical disk structure can attain very high frequencies while retaining relatively large dimensions because the high stiffness of the disk structure. The fundamental contour mode of the disk resonator offers a Q as high as 23,000 at 193 MHz since energy losses to the substrate are minimized by anchoring the resonator at its center which is the nodal point of the vibration mode [54], [55].

The transduction is based on the electrostatic force across a sub-micron dielectric gap. These electrostatic resonators typically have very high quality factors so they are among the excellent solutions to replace quartz resonators in reference clock circuits. However their electromechanical coupling is usually small and motional impedance is too high (up to several thousand ohms) that their interface with 50-ohm systems is very difficult for applications for RF filters.

1.3 Dissertation Outline

This dissertation is organized into eight chapters discussing about the AlN Lamb wave telemetry components. Chapter 1 contains the research motivation, technical challenges, and existing solutions. Chapter 2 provides the fundamentals of propagating characteristics of Lamb wave modes in AlN membranes. Resonator basics, design, modeling, and fabrication process are presented in Chapter 3.

Chapter 4 contains the theoretical simulations and analysis on the impact of electrode materials and thicknesses on the resonator performance. Specifically, rules will be given on choosing electrodes to optimize the k^2_{eff}.

Chapter 5 focuses on the analysis, design, simulation and testing result of high Q AlN LWRs using butterfly-shaped plates. Theoretical analysis and experimental demonstration will be provided to explain how the new design suppresses the anchor loss and boost the Q. Designs of the beveled and rounded tether-to-plate transitions will also be compared.

Chapter 6 focuses on the new temperature compensation technique that uses the symmetric SiO_2/AlN/SiO_2 sandwiched structure to replace the conventional AlN/SiO_2 asymmetric structure. The symmetrical SiO_2/AlN/SiO_2 sandwiched plate experiences the less temperature-induced bending deformation and can also enables the pure S_0 mode which shows the higher v_p and larger k^2 than the QS_0 mode in the AlN/SiO_2 bilayer plate.

Chapter 7 presents the demonstration of a low-Z_{min} and high-f_s AlN LWR by utilizing the first order symmetric (S_1) mode propagating in a specific thickness of AlN. Theoretical analysis and experimental result will be given to demonstrate that S_1 mode can exhibit higher f_s and lower Z_{min} the S_0 mode, which is desirable for enabling high-frequency and low-loss filters.

Chapter 8 will conclude this dissertation with the achievements and impacts of these research works, and discuss the potential research directions.

Chapter 2
Lamb Waves Propagating in AlN Piezoelectric Films

Piezoelectric thin films have been utilized in SAW and BAW filters mainly because of the efficient electromechanical transduction. Lamb wave in piezoelectric thin plates has drawn great attentions due to its high phase velocity. In this chapter, a study of the lowest-order Lamb wave modes (S_0 modes) in an AlN plate is presented. Phase velocities, electromechanical coupling coefficients, and dispersion characteristics of *TCF* of Lamb waves will be included in the theoretical studies.

2.1 Why AlN

After the piezoelectric effect was first discovered in quartz crystal, many materials

Table 2-1. Physical properties of ZnO, AlN, and $LiNbO_3$ [28], [56], [57].

	ZnO	AlN	$LiNbO_3$	Units
Density	5680	3260	4700	(kg/m^3)
Longitudinal acoustic wave velocity	~6350	~11300	~6550	(m/s)
Shear acoustic wave velocity	~2720	~6000	~3590	(m/s)
Lattice constant, *c*	3.249	3.112	13.863	(Å)
Lattice constant, *a*	5.206	4.982	5.150	(Å)
Piezoelectric coefficient, e_{15}	–0.48	–0.48	3.69	(C/m^2)
Piezoelectric coefficient, e_{31}	–0.57	–0.58	0.3	(C/m^2)
Piezoelectric coefficient, e_{33}	1.32	1.55	1.77	(C/m^2)
Thermal expansion (300 K)	2.92	4.15	5~15	(10^{-6}/°C)
Thermal conductivity	60	280	5.6	(W/mK)
TCF	–60	–25	–58~-90	(ppm/°C)

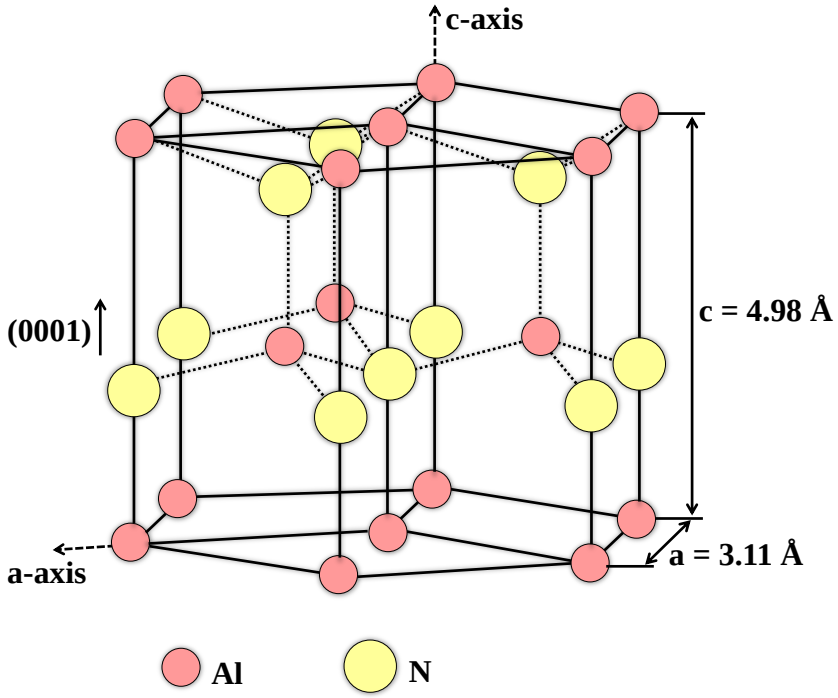

Figure 2-1. Hexagonal wurtzite crystal structure of AlN.

exhibiting piezoelectric properties are discovered and studied. Although some ceramics such as lead zircomium titanate (PZT, $Pb[Zr_xTi_{1-x}]O_3$, $0 \leq x \leq 1$]) have strong piezoelectric coefficients, they are difficult to be deposited as thin films and also suffer from large acoustic loss, so they are seldom used in MEMS acoustic devices. Normally, high electromechanical coupling coefficients, low electromechanical losses, good thermal stability, and CMOS compatibility are main concerns for developing and adopting new piezoelectric materials.

AlN emerged as the most suitable technology for the transduction of acoustic waves for RF applications because it is an excellent compromise between performance and manufacturability. Although its coupling coefficient is not as high as that of ZnO and $LiNbO_3$ that are also widely used in piezoelectric MEMS devices, it has high acoustic velocity, high thermal conductivity, low acoustic loss, chemical stability and relatively low *TCF*, as is shown in Table 2-1. On the contrary, the high acoustic loss and large TCF of ZnO limit its application as resonators and filters, and $LiNbO_3$ cannot be deposited as film directly currently and need complicated micromachining process. These properties enable the AlN MEMS resonators featuring the ability of high frequency, excellent power handling capability, high *Q*, functionality in harsh environment, and limited drift with temperature [28], [56], [57].

AlN can crystallize in both wurtzite and zinc-blende structures [3]. As illustrated in Figure 2–1, the AlN employed in resonators is wurtzite-structured material with *c*-axis, belonging to hexagonal crystal system, with polarized direction along the *c*-axis (0001) which is usually normal to the substrate.

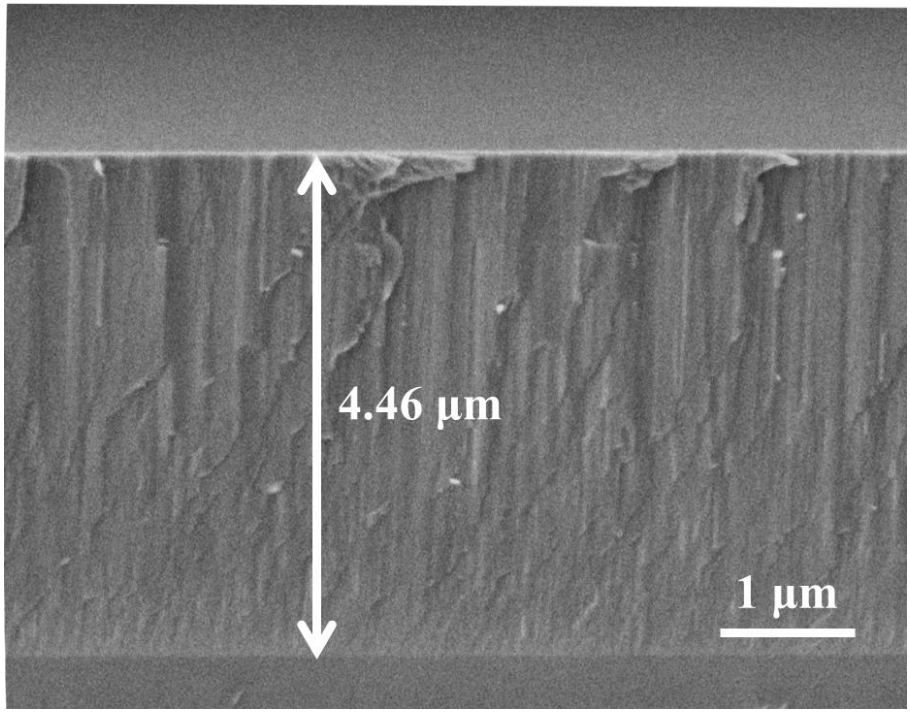

Figure 2-2. Hexagonal wurtzite crystal structure of AlN.

Another advantage of AlN is the low process temperature and the fact that it does not contain any contaminating elements harmful for semiconductor devices, unlike most other piezoelectric materials. This is essential in the case of monolithic integration of MEMS resonators with microelectronic integrated circuits. Reactive sputtering from a pure Al target in a plasma containing nitrogen is the most suitable method to obtain crystalline AlN films with sufficient quality for MEMS resonator applications at a deposition temperature lower than 400℃. Figure 2-2 shows the cross section of such an AlN film grown in pulsed DC mode. The microstructure is typical, with very densely packed columnar grains. The parameters of the AlN deposition process have to be optimized in order to ensure that a vast majority of grains are oriented along the c-axis since the spontaneous polarization of AlN, and hence the maximum piezoelectric effect, is parallel to that direction.

2.2 Piezoelectric Effect and its Constitutive Equations

2.2.1 The Piezoelectric Constants

“Piezoelectricity” is derived from the Greek word “piezein”, meaning “to press”, meaning that crystal that acquire charge when being compressed, twisted, or distorted are said to be piezoelectric. Piezoelectricity is described as the formation of the electric polarization or electric charges induced by a mechanical strain. Conversely, the inverse

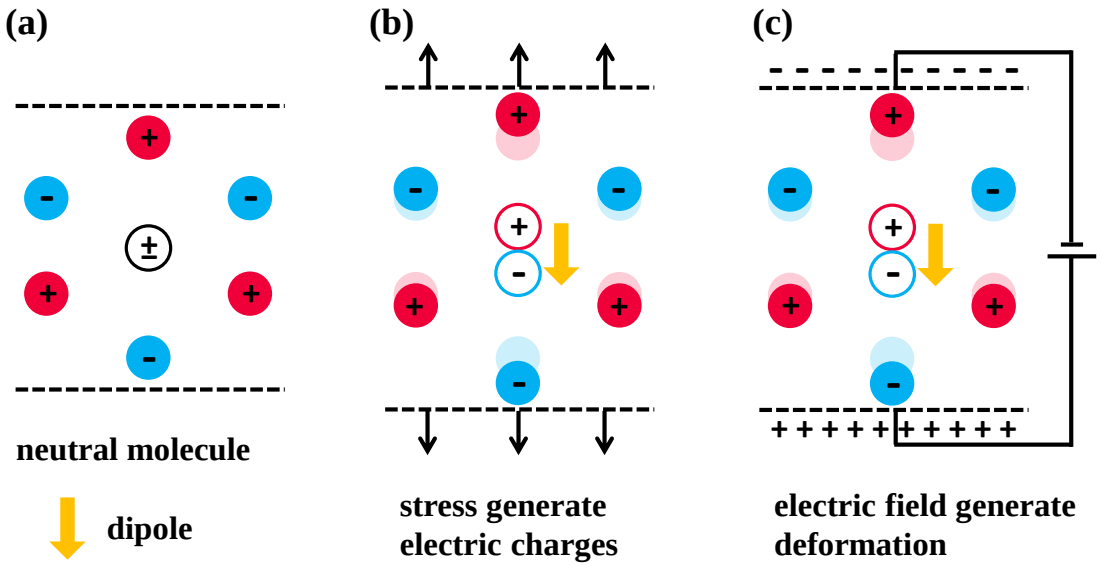

Figure 2-3. Schematic plot of (a) a piezoelectric material crystal structure explaining (b) the piezoelectric effect and (c) the reverse piezoelectric effect.

piezoelectric effect is a mechanical deformation produced when an electric field is applied to a piezoelectric substance, as shown in Figure 2-3. This is an inherent property of a material that has a non-symmetric crystallographic structure with respect to the center. The physical origin of piezoelectricity comes from the charge asymmetry within the primitive unit cell which results in the formation of a net electric dipole. The polar axis is an imaginary line pointing through the center of the negative and positive charge in the dipole. Crystals with a center of symmetry, such as cubic crystals, are not piezoelectric because the net electric dipole within the primitive cell is always zero, no matter how the structure deforms.

2.2.2 Piezoelectric Constants

Normally there are four types of piezoelectric coefficient: *d*, e, *g*, and *h*. These four piezoelectric constants are all related but each represents a different aspect of the piezoelectric relationship and is useful for a different set of conditions. *d* measures the strain in a free crystal for a given applied field, *e* the stress developed by a given field when the crystal is clamped, *g* the open-circuit voltage for a given stress, and *h* the open-circuit voltage for a given strain [58]. Piezoelectric coefficients *d*, *e*, *g*, and *h* can be converted into each other. Equation (2.1) relates these four piezoelectric coefficients with *T*, *S*, *D*, and *E* , in which the first set of four terms correspond to the direct piezoelectric effect and the second set of four terms describe the reverse piezoelectric effect [3]:

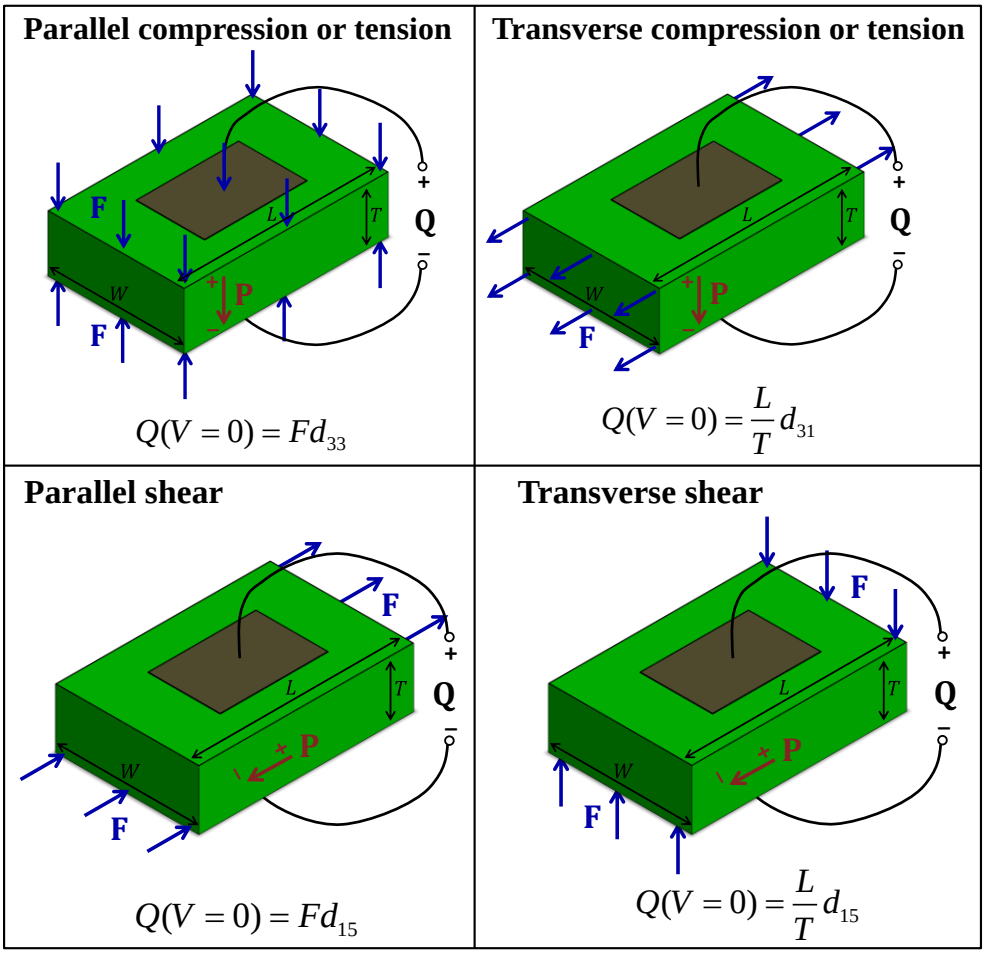

Figure 2-4. A piezoelectric brick with different piezoelectric actuation modes (d_{33}. d_{31}, d_{15} actuation with different pole and force direction).

$$
\begin{aligned}
d_{ij} &= (\frac{\partial D_i}{\partial T_j})^E = (\frac{\partial S_j}{\partial E_i})^T \\
e_{ij} &= (\frac{\partial D_i}{\partial S_j})^E = -(\frac{\partial T_j}{\partial E_i})^S \\
g_{ij} &= -(\frac{\partial E_i}{\partial T_j})^D = (\frac{\partial S_j}{\partial D_i})^T \\
h_{ij} &= -(\frac{\partial E_i}{\partial S_j})^D = -(\frac{\partial T_j}{\partial D_i})^S
\end{aligned}
\quad . \tag{2.1}
$$

The piezoelectric charge constant, d, is the mostly widely used to characterize piezoelectric materials. It is defined as the polarization generated per mechanical stress (T) applied to a piezoelectric material or, alternatively, the mechanical strain (S)

experienced by a piezoelectric material per electric field applied. The first subscript to *d* indicates the direction of polarization generated in the material or the direction of the applied field. The second subscript is the direction of the applied stress or the induced strain, respectively. Because the strain induced in a piezoelectric material is the product of the value for the electric field and the value of *d*, *d* is an important measure for strain-dependent actuator applications. As is shown in Figure 2-4 is examples of how the piezoelectricity (here the piezoelectric strain parameter *d*-coefficients are used) relates the force and charge of a piezoelectric block. Therefore, for the BAW resonators only the d_{33} coefficient is involved, for the SAW resonators the d_{31} coefficient is dominant, and for the Lamb wave resonators the piezoelectric constants d_{31}, d_{33}, and d_{15} all play parts.

2.2.3 Constitutive Equations

In the mechanical domain of a linear elastic material the Hooke's Law dominates:

$$T = cS \text{ or } S = sT, \tag{2.2}$$

where *c* is the elastic stiffness constant, *s* is the elastic compliance constant, *T* is the stress tensor, and *S* is the strain tensor.

In the electrical domain, the dielectric constant relates the charge density displacement vector *D* and electric field vector *E*,

$$D = \varepsilon E \text{ or } E = \beta D, \tag{2.3}$$

where ε is the dielectric permittivity constant and β is the dielectric impermittivity constant.

Like mentioned before, piezoelectricity combine the mechanical and electrical behavior of the material. As mentioned before, there are four types of piezoelectric coefficient: *h*, *d*, *g*, *e*, among which *d* and *e* form are most widely used because they directly relate the stress and strain tensors. We have talked about the *d*-piezoelectric coefficient before, and the *e* form equations are used for calculation in this report. The *e*-form constitutive equation is [59]:

$$\begin{cases} T = c^E S - e^T E \\ D = \varepsilon^S E - eS \end{cases}, \tag{2.4}$$

where the superscripts *E* and *S* in the stiffness constant and the dielectric constant denote that they are measured at constant electric field and constant strain, but the superscript *T* in the piezoelectric constant e denotes the transport of the matrix.

Since AlN like most piezoelectric medium is with hexagonal symmetry, the constitutive equations can be simplified to:

$$\begin{bmatrix} T_1 \\ T_2 \\ T_3 \\ T_4 \\ T_5 \\ T_6 \end{bmatrix} = \begin{bmatrix} c_{11} & c_{12} & c_{13} & 0 & 0 & 0 \\ c_{12} & c_{22} & c_{23} & 0 & 0 & 0 \\ c_{13} & c_{23} & c_{33} & 0 & 0 & 0 \\ 0 & 0 & 0 & c_{44} & 0 & 0 \\ 0 & 0 & 0 & 0 & c_{44} & 0 \\ 0 & 0 & 0 & 0 & 0 & c_{44} \end{bmatrix} \begin{bmatrix} S_1 \\ S_2 \\ S_3 \\ S_4 \\ S_5 \\ S_6 \end{bmatrix} - \begin{bmatrix} 0 & 0 & e_{31} \\ 0 & 0 & e_{31} \\ 0 & 0 & e_{33} \\ 0 & e_{15} & 0 \\ e_{15} & 0 & 0 \\ 0 & 0 & 0 \end{bmatrix} \begin{bmatrix} E_1 \\ E_2 \\ E_3 \end{bmatrix}, \tag{2.5}$$

$$\begin{bmatrix} D_1 \\ D_2 \\ D_3 \end{bmatrix} = \begin{bmatrix} \varepsilon_1 & 0 & 0 \\ 0 & \varepsilon_2 & 0 \\ 0 & 0 & \varepsilon_3 \end{bmatrix} \begin{bmatrix} E_1 \\ E_2 \\ E_3 \end{bmatrix} + \begin{bmatrix} 0 & 0 & 0 & 0 & e_{15} & 0 \\ 0 & 0 & 0 & e_{15} & 0 & 0 \\ e_{31} & e_{32} & e_{33} & 0 & 0 & 0 \end{bmatrix} \begin{bmatrix} S_1 \\ S_2 \\ S_3 \\ S_4 \\ S_5 \\ S_6 \end{bmatrix}. \tag{2.6}$$

Similar to the *d*-coefficient described previously, the e_{3l} term maps the thickness electric field to contour stress or maps the contour train to thickness charge flux, and e_{33} maps thickness electric field to thickness stress or thickness strain to thickness charge flux.

The coefficient of stiffness matrix (*c*), piezoelectric stress (*e*) matric, piezoelectric strain matrix (*d*), and the dielectric matrix of the AlN film used in calculation in this report are listed below [59], [60]:

$$[c] = \begin{bmatrix} 3.45 & 1.25 & 1.20 & 0 & 0 & 0 \\ 1.25 & 3.45 & 1.20 & 0 & 0 & 0 \\ 1.20 & 1.20 & 3.95 & 0 & 0 & 0 \\ 0 & 0 & 0 & 1.18 & 0 & 0 \\ 0 & 0 & 0 & 0 & 1.18 & 0 \\ 0 & 0 & 0 & 0 & 0 & 1.18 \end{bmatrix} (10^{11}\ \mathrm{N/m^2}), \tag{2.7}$$

$$[e] = \begin{bmatrix} 0 & 0 & 0 & 0 & -0.48 & 0 \\ 0 & 0 & 0 & -0.48 & 0 & 0 \\ -0.58 & -0.58 & 1.55 & 0 & 0 & 0 \end{bmatrix} (\mathrm{C/m^2}), \tag{2.8}$$

$$[d] = \begin{bmatrix} 0 & 0 & 0 & 0 & -4.068 & 0 \\ 0 & 0 & 0 & -4.068 & 0 & 0 \\ -2.646 & -2.646 & 5.532 & 0 & 0 & 0 \end{bmatrix} (10^{-12}\ \mathrm{m/V}) \tag{2.9}$$

$$[\varepsilon] = \begin{bmatrix} 8.0 & 0 & 0 \\ 0 & 8.0 & 0 \\ 0 & 0 & 9.5 \end{bmatrix} (10^{-11}\text{F/m}). \quad (2.10)$$

2.3 Solid Acoustic Wave Propagation

2.3.1 Solid Acoustic Wave Fundamentals

The acoustic wave propagating in solids are generally two types: bulk acoustic wave and surface acoustic wave. Bulk acoustic waves travel in the bulk of solid materials, including longitudinal waves and shear waves, while surface acoustic wave can only travel along the surface of materials. The longitudinal wave is when the particle vibration is in the direction of wave propagation. The shear velocity is when the vibration is perpendicular to the propagation direction of the wave.

Given the material properties of piezoelectric materials and the propagation direction of acoustic waves, the stiffen Christoffel matrix approach can be utilized to solve for the

Table 2-2. Material constants of AlN used in the calculations [61], [62].

	Symbol	AlN	Units
Stiffness constants	c_{11}	345	$(10^9\ \text{N/m}^2)$
	c_{12}	125	
	c_{13}	120	
	c_{33}	395	
	c_{44}	118	
	c_{66}	110	
Mass density	ρ	3260	(kg/m^3)
Piezoelectric constants	e_{15}	–0.48	(C/m^2)
	e_{31}	–0.58	
	e_{33}	1.55	
Dielectric constants	ε_{11}	8.0	$(10^{-11}\ \text{F/m})$
	ε_{33}	9.5	

phase velocity and piezoelectric coupling constant (k^2) of a specific acoustic wave mode.

By solving the Christoffel equation, we can obtain the longitudinal wave with phase velocity:

$$v_l = \sqrt{\frac{c_{11}}{\rho}}. \tag{2.11}$$

For AlN with the material properties listed in Table 2-2, the v_L=10287.28 m/s. we can also obtain one pure shear mode with phase velocity:

$$v_{ps} = \sqrt{\frac{c_{66}}{\rho}}, \tag{2.12}$$

and one stiffen shear mode with phase velocity:

$$v_{ss} = \sqrt{\frac{c_{44} + \frac{e_{15}}{\varepsilon_{11}}}{\rho}}, \tag{2.13}$$

$$k^2 = \frac{e_{15}^2}{c_{44}\varepsilon_{11}}. \tag{2.14}$$

For AlN with properties listed in Table 2-2, the pure slow shear mode has the phase velocity 5597 m/s, and the fast shear mode has the phase velocity 5867 m/s with k^2 2.45%. Therefore, the (2000) AlN membranes provide a pure fast shear mode.

Following the similar approach as developed by Campbell, the matrix method is effectively employed. The Rayleigh wave only propagates at surfaces. The Rayleigh velocity is often approximated by:

$$v_R \cong \frac{0.87 + 1.12\gamma}{1+\gamma} v_S, \tag{2.15}$$

where γ is the Poisson ration, and

$$\frac{v_L}{v_S} = \sqrt{\frac{c_{11}}{c_{44}}} = \sqrt{\frac{1-\gamma}{\frac{1}{2}-\gamma}}. \tag{2.16}$$

For piezoelectric materials the phase velocity of propagation of acoustic waves is higher than that in the non-piezoelectric case, since the effective stiffness is enhanced by the piezoelectric stress term, namely piezoelectric stiffening:

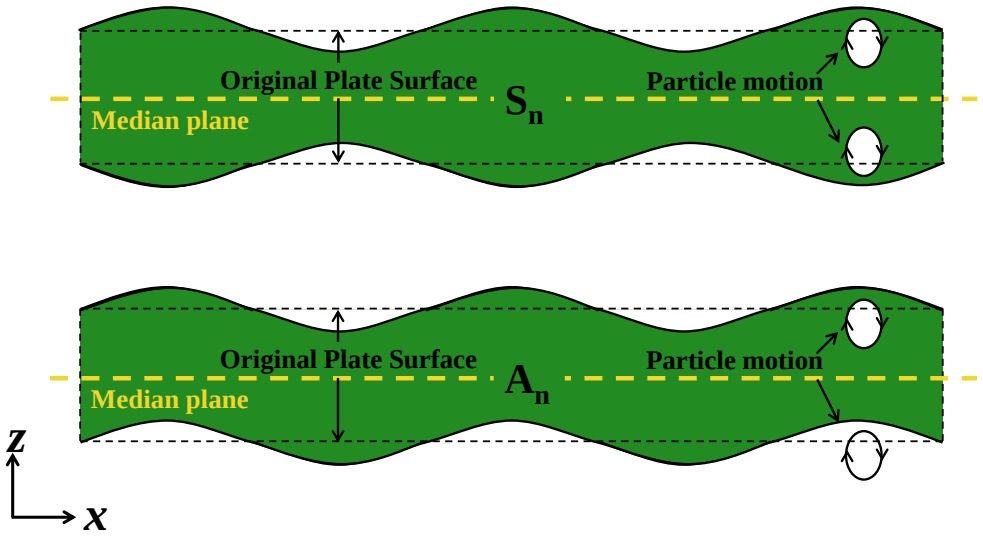

Figure 2-5. Schematic of symmetric and asymmetric Lamb wave modes.

$$c_{eff}^{E} = c^{E} + \frac{e^2}{\varepsilon^2}. \tag{2.17}$$

Therefore, the unstiffened phase velocity and piezoelectric stiffened phase velocity of a material are:

$$v_{unstiffened} = \sqrt{\frac{c^E}{\rho}}, \tag{2.18}$$

$$v_{stiffened} = \sqrt{\frac{c_{eff}^E}{\rho}} = \sqrt{\frac{c^E + \frac{e^2}{\varepsilon^2}}{\rho}} = v_n \sqrt{\frac{1}{1-k^2}}, \tag{2.19}$$

where the k^2 is the electromechanical coupling coefficient [63], [64]:

$$k^2 = \frac{e^2}{\varepsilon^S c^D}. \tag{2.20}$$

2.3.2 The Lamb Wave

When surface acoustic waves are guided laterally into a sufficiently thin enough ($h < 10\lambda$) plate, they are referred to as Rayleigh-Lamb waves or Lamb wave. Lamb wave modes generally only have displacements in the x- and z- directions, so depending on the symmetry of the particle displacements associated with the wave relative to the median

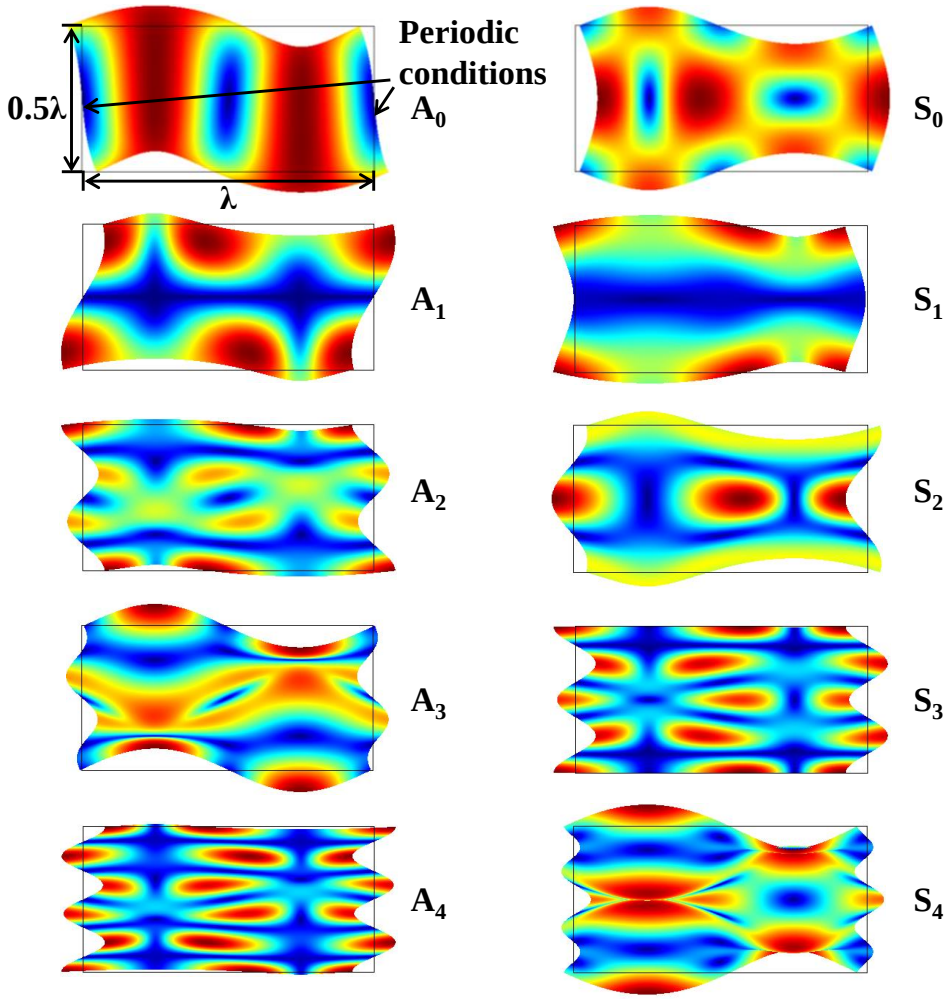

Figure 2-6. Displacement fields of different Lamb wave modes from FEA simulation.

plane of the plate, Lamb waves are sorted into symmetric and anti-symmetric modes, as illustrated in Figure 2-5.

Generally, the different plate modes are denoted as S_n or A_n, representing the nth order symmetric or asymmetric Lamb wave modes, where 'n' is an integer ranging from 0 to infinity and represents the number of standing waves along the plate thickness.

The two sets of S_n and A_n modes can be expressed as:

$$S_n: \frac{\tan(\frac{\beta h}{2})}{\tan(\frac{\alpha h}{2})} = -\frac{4\alpha\beta k^2}{(k^2-\beta^2)}, \tag{2.21}$$

$$A_n: \frac{\tan(\frac{\beta h}{2})}{\tan(\frac{\alpha h}{2})} = -\frac{(k^2-\beta^2)}{4\alpha\beta k^2}, \quad (2.22)$$

where $\alpha^2 = \frac{\omega^2}{v_l^2} - k^2$ and $\beta^2 = \frac{\omega^2}{v_t^2} - k^2$, where h is the thickness of the membrane, ω is the angular frequency, k the wave number, v_l and v_t the longitudinal and transverse velocities of the material, respectively.

Figure 2-6 shows the displacement fields of different Lamb wave modes from COMSOL. The fundamental symmetric mode is sometimes referred to as contour modes, and anti-symmetric modes sometimes referred to as flexural modes. For single AlN thin films, the high modes are difficult to be observed because of their smaller coupling coefficient compared to fundamental modes.

Among the Lamb wave modes, the lowest-order (fundamental) symmetric (S_0) mode is being most widely explored in AlN Lamb wave resonators since the S_0 mode propagating in the AlN thin plate exhibits weak phase velocity dispersion, high quality factor, and large electromechanical coupling coefficient compared to the other Lamb wave modes.

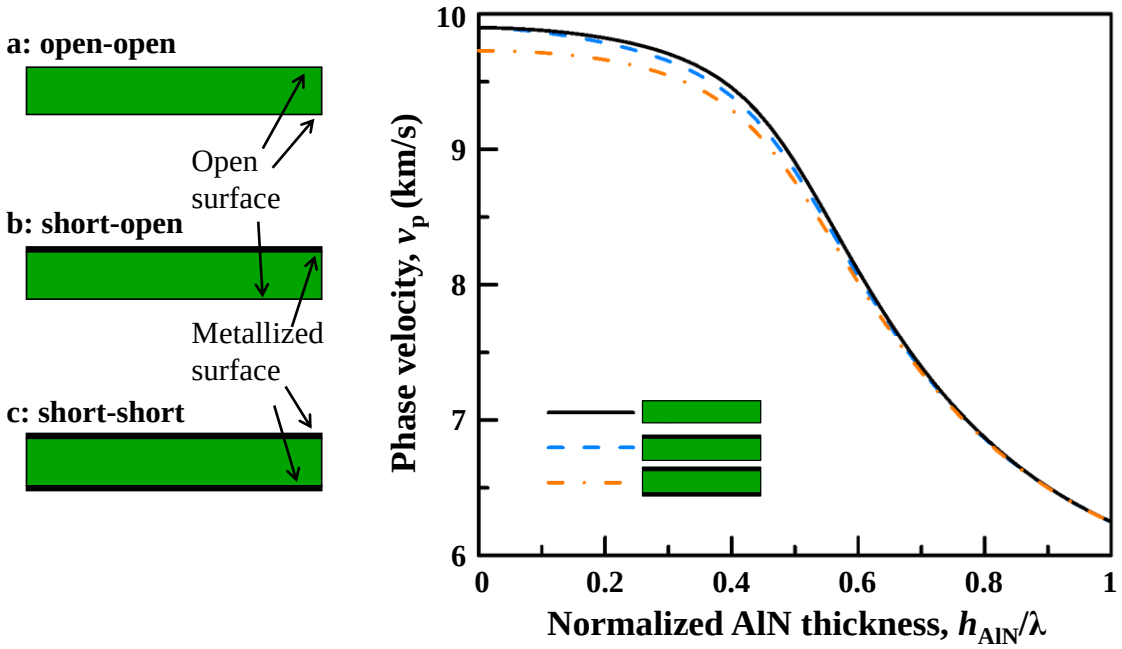

Figure 2-7. Dispersion of the phase velocity for the three basic boundary conditions for AlN Lamb wave devices using the lowest symmetric Lamb wave mode S_0.

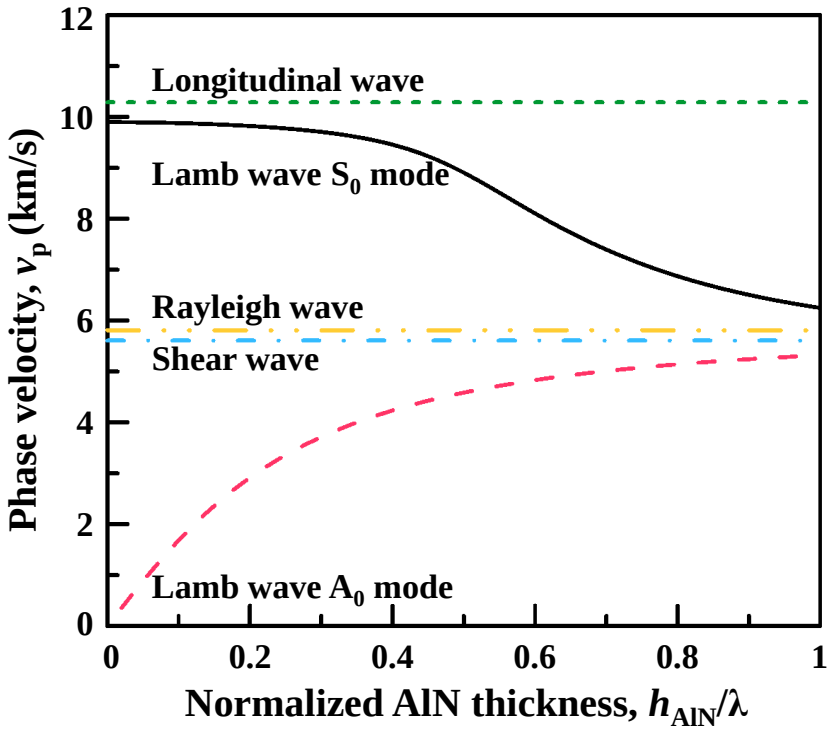

Figure 2-8. Calculated phase velocities of the first two Lamb wave modes comparing with the phase velocities of longitudinal, Rayleigh and shear waves propagating in an AlN membrane.

2.4 Characteristics of the S_0 Lamb Wave Mode in an AlN Film

2.4.1 The v_p of the S_0 Lamb Wave Mode

There are three fundamental boundary conditions (BCs) for AlN membranes: both surfaces free (open-circuited), one surface metallized (short-circuited) and the other free (open-circuited), and both surface metallized (short-circuited), as illustrated in Figure 2-7: BCs a, b and c. Here the mechanical effect of the metallization is ignored, in other words the metallization is assumed to be infinitely thin.

The phase velocities of the symmetric fundamental (S_0) mode are computed for these three boundary conditions based on the approach by Nassar [18] and using the materials data for AlN listed in Table 2-2. The acoustic propagation properties are dispersive and are generally characterized by the normalized AlN thickness. The metallization slightly lowers the phase velocity (Figure 2-7), and the difference is actually determined by the intrinsic coupling coefficient (k^2), which will be introduced later. Otherwise, since the phase velocities of the three scenarios are very close, we will use the open-open phase velocity when discuss phase velocities for simplicity later in this thesis.

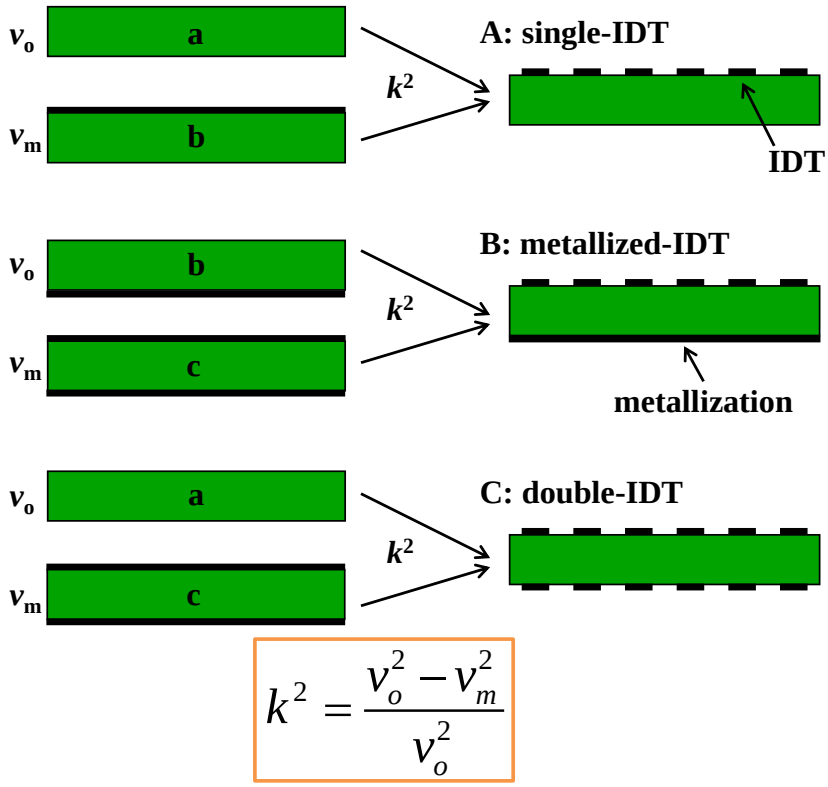

Figure 2-9. Three basic surface electrical boundary conditions for Lamb wave devices: (a) single-IDT, (b) metallized-IDT, and (c) double-IDT.

Figure 2–8 shows the calculated phase velocity dispersions of the first two Lamb wave modes propagating in an AlN membrane, comparing with the phase velocities of longitudinal, Rayleigh and shear waves in AlN. The S_0 Lamb wave mode shows a phase velocity near 10,000 m/s which is close to the phase velocity of longitudinal wave (BAW), and it exhibits much weaker phase velocity dispersion than the A_0 Lamb wave mode. The high phase velocity of the S_0 mode in an AlN plate is suitable for high frequency devices and the weak phase velocity dispersion is preferred for fabrication robustness. When the plate is becoming thick, both the phase velocities of the A_0 and S_0 Lamb wave modes approaches that of Rayleigh mode.

2.4.2 The k^2 of the S_0 Lamb Wave Mode

The intrinsic electromechanical coupling coefficient of Lamb waves is estimated based on the difference of the phase velocities for a free surface v_o and metallized surface v_m, as [66], [68]:

$$k^2 = \frac{v_o^2 - v_m^2}{v_o^2}. \qquad (2.23)$$

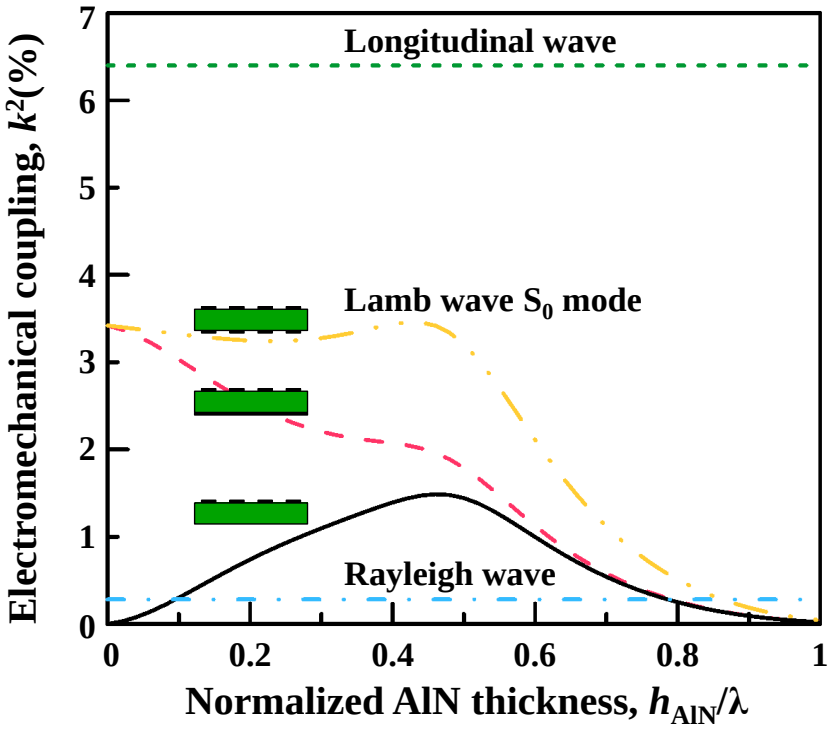

Figure 2-10. Comparison of the calculated k^2 of Lamb wave S_0 mode with different electrical surface boundary conditions and also the k^2 of longitudinal and Rayleigh waves.

For more exact simulations, the Green's function method can be adopted to calculate the electromechanical coupling coefficient in the piezoelectric membrane [65]-[67].

This method of estimating k^2 is valid as long as the plate thickness h is smaller than the wavelength λ, which is the case for all computed results presented in this chapter. More complicated cases will be discussed next chapter considering the potential of electrodes using Finite Element Analysis (FEA). The intrinsic coupling coefficients k^2 for the three configurations are based on the respective configurations (a, b and c) for v_o and v_m illustrated for each of the cases in Figure 2-9 and shown in Figure 2-7. The results of the coupling for the three electrode configurations A, B and C are shown in Figure 2-10, with comparison to longitudinal wave and Rayleigh wave.

Generally, the double-IDT configuration exhibits the largest k^2 and single-IDT the smallest. Particularly, the single-IDT case has a peak k^2 when λ~0.5 and is limited to 1.5%, the metallized-IDT electrode configuration enables k^2 as large as 3% when AlN is thin ($h_{AlN} < 0.2\lambda$), and the double-IDT gives k^2 above 3% as long as $h_{AlN} < 0.6\,\lambda$.

The intrinsic coupling coefficients for the Lamb wave under different surface boundary conditions are mostly much larger than the Rayleigh wave, showing advantage in the application of enabling filters than the SAW devices in the AlN piezoelectric material. Although the k^2 are smaller than the longitudinal wave used in BAW resonators, they are sufficient in the applications of oscillators and narrow-band filters. In addition,

Table 2-3. Temperature coefficients of material constants of AlN used in the calculations. [69]

	Symbol	AlN	Units
Temperature coefficients of stiffness constants	TC_{11}	–37	(10^{-6} 1/°C)
	TC_{12}	–1.8	
	TC_{13}	–1.8	
	TC_{33}	–65	
	TC_{44}	–50	
	TC_{66}	–57	
Thermal expansion coefficients	α_{11}	5.27	(10^{-6} 1/°C)
	α_{33}	4.15	

the dispersive characteristics in k^2 of the S_0 Lamb wave mode give more engineering freedom comparing to the Rayleigh wave and Longitudinal wave.

2.4.3 The *TCF* of the S_0 Lamb Wave Mode

Most materials become softer when temperature increases, meaning that they have negative *TCE*s, including the AlN. This will lead to a decrease in frequency when temperature rises and an increase in frequency when temperature cools down. Table 2–3 lists the temperature coefficients of AlN which are used to predict the frequency-temperature behavior of the AlN LWR using the S_0 mode.

The frequency drift of the AlN LWR not only dependent on the changes in the stiffness constants with temperature and but also the thermal expansion coefficients. Under linear approximation of the temperature dependence of the stiffness constants, the *TCF* of the AlN LWR is [68]:

$$TCF_{1st} = \frac{1}{v_p}\frac{\partial v_p}{\partial T} - \alpha_x = \frac{1}{v_p}\frac{v_p(T_0+\Delta T) - v_p(T_0)}{\Delta T} - \alpha_x, \tag{2.24}$$

where $v_p(T_0)$ is calculated from the material constants in Table 2-3, α_x corresponds to the effective thermal expansion coefficient along the wave propagation direction (x direction) in this case. and $v_p(T_0+\Delta T)$ is calculated based on the new stiffness matrix $c_{ij}(T_0+\Delta T)$:

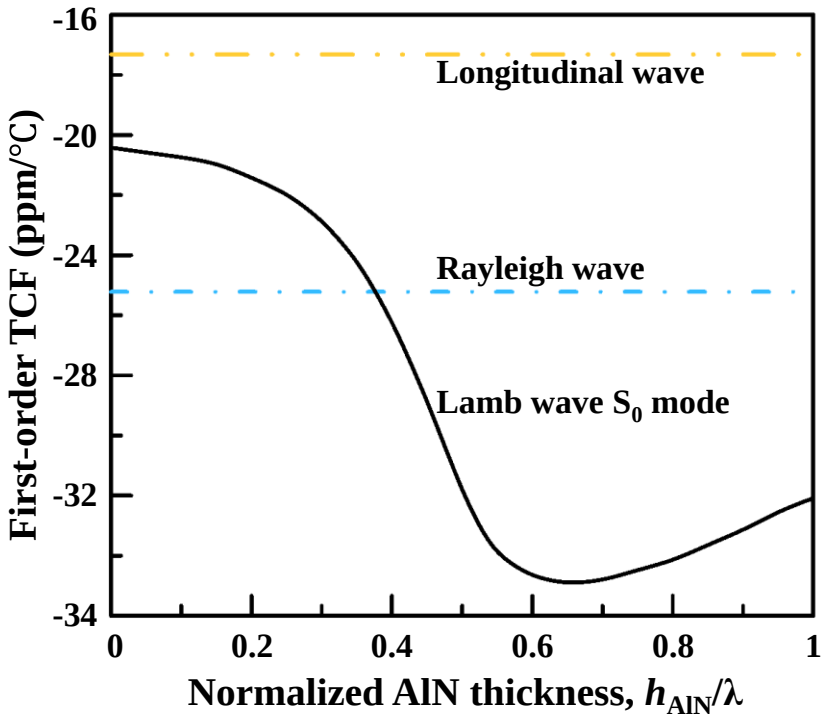

Figure 2-11. Calculated first-order *TCF*s of the Lamb wave S_0 modes comparing with longitudinal and Rayleigh waves in AlN.

$$c_{ij}(T_0+\Delta T)=c_{ij}(T_0)(1+TCE_{ij})\,. \tag{2.25}$$

The ΔT is assumed to be 10 ˚C in this dissertation.

Therefore, the *TCF* of the AlN LWR can be theoretically predicted using the above formulas and the temperature dependence of material coefficients listed in Table 2–3. Since there are only first-order temperature coefficients of stiffness constants available in the literature, all theoretical calculations only considers the first-order effect on the *TCF* in this study. The calculated first-order *TCF*s of the Lamb wave S_0 modes comparing with longitudinal and Rayleigh waves in AlN are shown in Fig. 2–11. The AlN LWR using the S_0 mode shows a theoretical *TCF* range from -33 to –22 ppm/°C which is close to the experimental results [68]. What's more, it is interesting to note that the first-order *TCF* shows a dispersive characteristic and reaches the worst case when the AlN membrane thickness is around 0.62λ.

Chapter 3
Design of AlN Lamb Wave Resonators Utilizing S_0 Mode

3.1 Equivalent Circuit and Typical Frequency Response

As illustrated in Figure 3-1, a Lamb wave resonator usually consists of the AlN plate as the resonant cavity, the supporting tethers providing the rigid attachment to the substrate, and the IDT transducer that is two sets of electrodes connected alternatively to two bus bars placed on a piezoelectric substrate. The space *p* between two adjacent electrode fingers and their overlap length W are called pitch and aperture. The metallization ratio (η) is usually 0.5 and the IDT finger width is equal to quarter wavelength ($\lambda/4$) in this case. The resonance frequency is equal to the ratio of the phase velocity of the wave mode and the wavelength, thus determined by the wave characteristics and the IDT width:

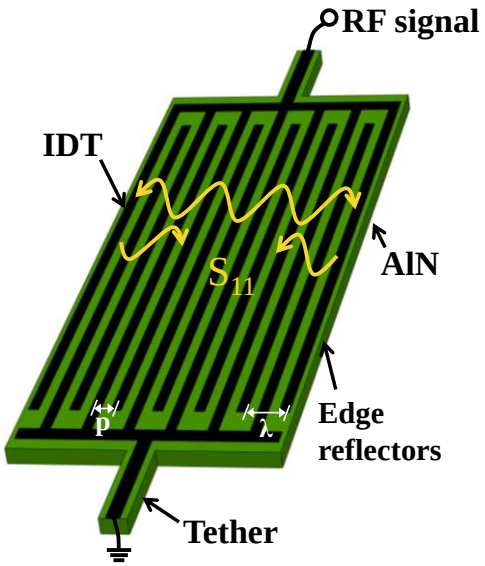

Figure 3-1. Illustration of one-port AlN Lamb wave resonator employing the edge-type reflector.

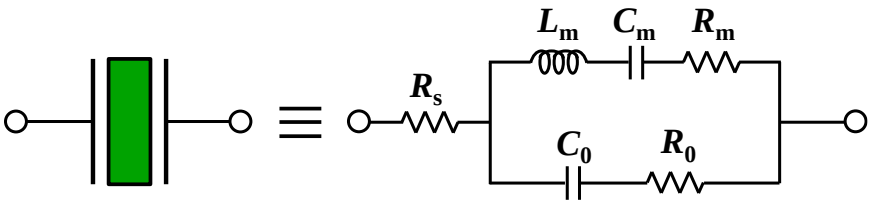

Figure 3-2. Modified Butterworth-Van Dyke (MBVD) equivalent circuit model

$$f_s = \frac{v_p}{\lambda} = \frac{v_p}{2p}. \tag{3.1}$$

A piezoelectric resonator usually can be described using the Butterworth-Van Dyke (BVD) equivalent circuit which consists of a mechanical resonance branch including a motional resistance (R_m), a motional capacitance (C_m), and a motional inductance (L_m) in series and a static capacitance (C_0) in parallel, as depicted in Figure 3-2. The static capacitance C_0 is simply formed by the capacitance between the IDT finger electrodes and the plate capacitance sandwiched between the top and bottom electrodes. As shown in Figure 3-2, a modified Butterworth-Van Dyke (MBVD) equivalent circuit model including two loss resistors, R_s and R_0, was proposed to improve matching for real piezoelectric BAW resonators [70]. Nominally, the series resistor R_s describes the resistance of routing pads and electrodes, and the parallel resistor R_0 represents the parasitic resistance in the Si substrate [28]. Based on the six parameters in the MBVD equivalent circuit, the series and parallel resonance frequencies, f_s and f_p, the impedance $Z(\omega)$, and the quality factors at the series and parallel frequencies, Q_s and Q_p, can be expressed as [28], [70], [72]

$$f_s = \frac{\omega_s}{2\pi} = \frac{1}{2\pi}\sqrt{\frac{1}{L_m C_m}}, \tag{3.2}$$

$$f_p = \frac{\omega_p}{2\pi} = \frac{1}{2\pi}\sqrt{\frac{1}{L_m C_m}\left(1+\frac{C_m}{C_0}\right)}, \tag{3.3}$$

$$Z(\omega) = R_s + \frac{\left(R_0 + \frac{1}{j\omega C_0}\right)\left(R_m + \frac{1}{j\omega C_m} + j\omega L_m\right)}{R_0 + \frac{1}{j\omega C_0} + R_m + \frac{1}{j\omega C_m} + j\omega L_m}, \tag{3.4}$$

$$Q_s = \frac{1}{\omega_s (R_m + R_s) C_m}, \tag{3.5}$$

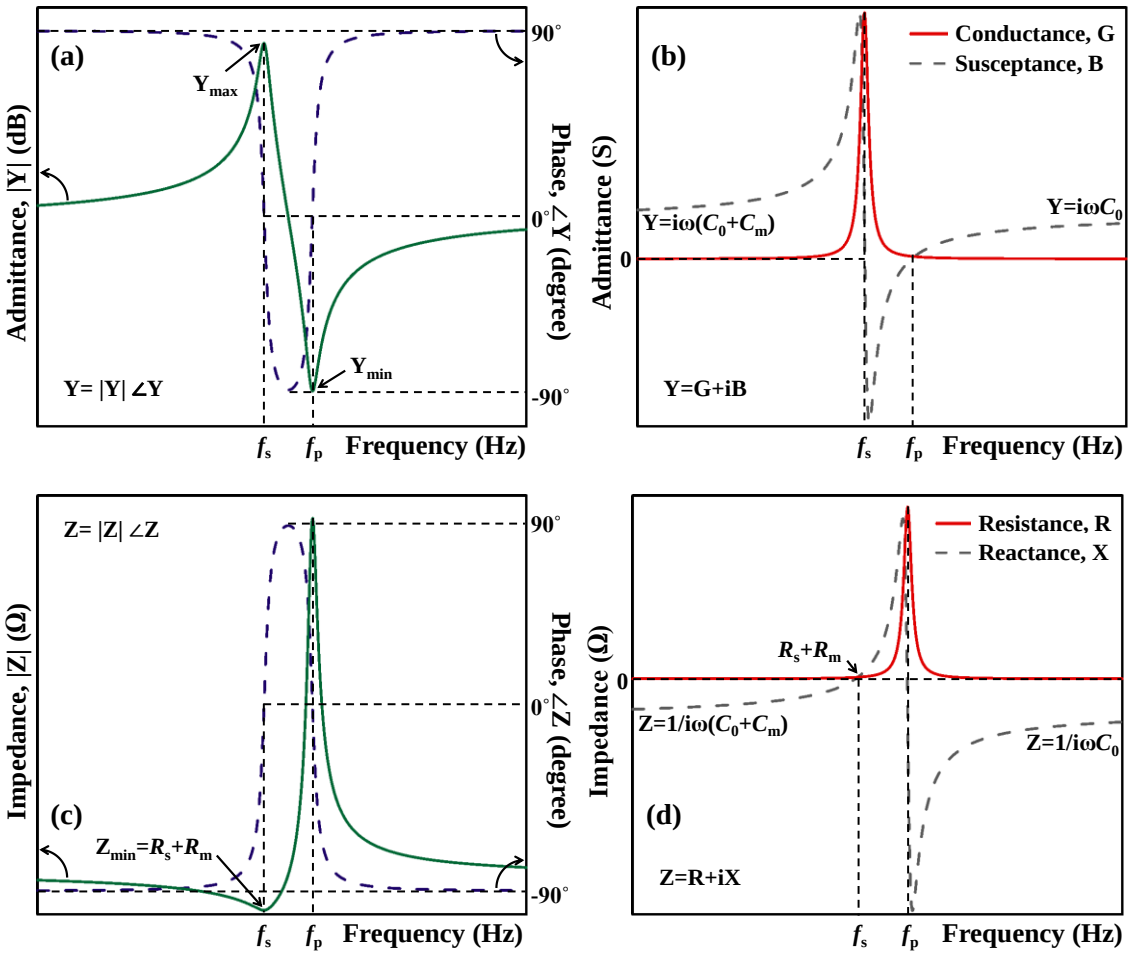

Figure 3-3. Typical frequency responses of a Lamb wave resonator.

$$Q_{\mathrm{p}} = \frac{1}{\omega_{\mathrm{p}}\left(R_{\mathrm{m}} + R_0\right)C_{\mathrm{m}}}, \tag{3.6}$$

$$k_{\mathrm{eff}}^2 = \frac{\pi^2}{8}\left(\frac{C_{\mathrm{m}}}{C_0}\right), \tag{3.7}$$

where ω_{s} and ω_{p} are the angular frequencies at the series and parallel resonance frequencies, respectively. It should be noted that the expressions of the Q_{s} and Q_{p} are loaded quality factors at f_{s} and f_{p}, respectively, since the parasitic R_{s} and R_0 are included and hence lower the intrinsic mechanical quality factors.

Figure 3-3 presents the typical frequency response of a resonator with associated MBVD parameters. At resonance the spectrum shows the maximum admittance and a 0 degree phase, and at anti-resonance it exhibits the minimum admittance and a 0 degree phase. The real part of admittance (conductance) is near 0 at frequencies off resonance

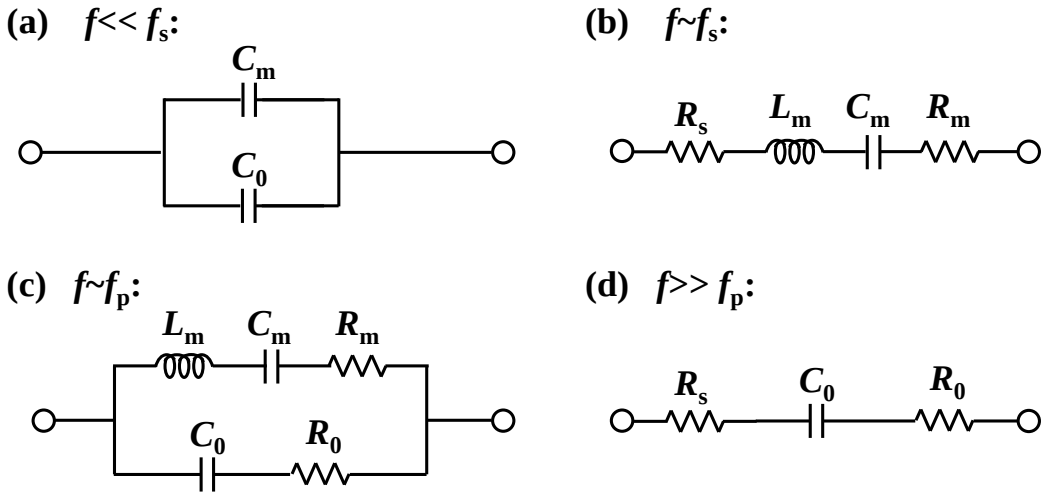

Figure 3-4. Modified Butterworth-Van Dyke (MBVD) equivalent circuit model for the acoustic resonator at different frequency ranges.

and the imaginary part (susceptance) is highly dependent on the static capacitance. The opposite can be observed for the impedance spectrum of the frequency response.

Figure 3-4 shows the approximated MBVD model at different frequency ranges. When off resonance, the resonator exhibits like a capacitor. When the resonator is at resonance, the current only goes through the motional branch. When the resonator is at anti-resonance, the current circulates in the motional and static branches and no signal out to be detected.

3.2 Electrode Configurations of Lamb Wave Resonators

3.2.1 The Resonance Frequency f_s

The short boundary condition on the surface of the piezoelectric membrane reduces the phase velocity, as discussed in the previous chapter and presented again in Figure 3-5(b). Therefore, the electrical loading effect for different configurations of devices is very similar and the corresponding phase velocity for the different electrode configurations can be simulated and shown in Figure 3-5(a). The grounded-BE, floating-BE and double-IDT electrode configurations show similar phase velocity, or normalized resonance frequency, and are only slightly lower than the single-IDT type. Thus, the phase velocities for different electrode configurations are assumed to be the same in the later discussions in this dissertation.

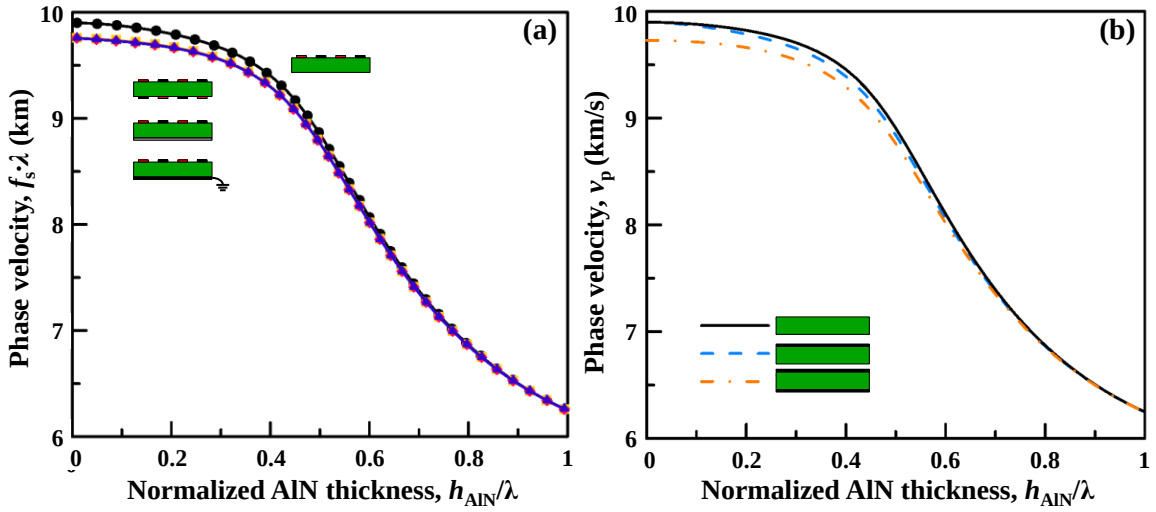

Figure 3-5. Comparison of the (a) simulated effective coupling coefficient k_{eff}^2 using FEA for four electrode configurations (single-IDT, IDT-grounded BE, IDT-floating BE and double-IDTs) and (b) numerically calculated electromechanical coupling coefficients for three metallization conditions (single-IDT, metalized-IDT, and double-IDTs).

3.2.2 The Effective Coupling Coefficient k_{eff}^2

As introduced in the previous chapter, the intrinsic electromechanical coupling coefficient k^2 is a measure of the energy transduction efficiency between the electrical and mechanical domains, and can be calculated by the velocity difference equation. Nevertheless, the effective coupling coefficient k_{eff}^2 for resonator devices from the measured results can be evaluated in several ways, among which the most often used definitions, is IEEE standard definition [71], [72].

$$k_{eff}^2 = \frac{\pi}{2}\frac{f_s}{f_p}\left[\tan\left(\frac{\pi}{2}\frac{f_s}{f_p}\right)\right]^{-1}. \tag{3.7}$$

The most used approximation for the effective coupling coefficient is

$$k_{eff}^2 = \frac{\pi^2}{4}\left(\frac{f_p - f_s}{f_p}\right). \tag{3.8}$$

The k_{eff}^2 is in fully consistent with the k^2 for BAW resonators by this definition. But for Lamb wave resonators there are small difference between these two measures. What's more, although different metallization configurations are considered for the k^2 as shown in Figure 3-6, the difference between grounded and floating bottom electrode should be considered for the k_{eff}^2 from the device perspective.

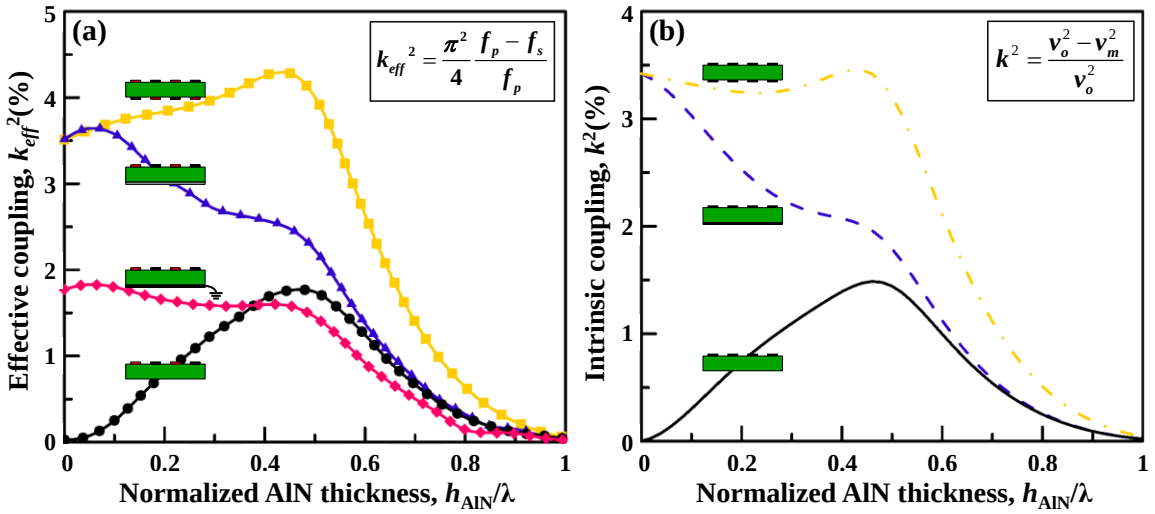

Figure 3-6. Comparison of the (a) simulated effective coupling coefficient k_{eff}^2 using FEA for four electrode configurations (single-IDT, IDT-grounded BE, IDT-floating BE and double-IDTs) and (b) numerically calculated electromechanical coupling coefficients for three metallization conditions (single-IDT, metalized-IDT, and double-IDTs).

The comparison between Figure 3-6(a) and Figure 3-6(b) reveals that the IDT-metallization case for the calculation of k^2 corresponds to the floating bottom electrode case for the simulation of k_{eff}^2, and the difference between the corresponding k^2 and k_{eff}^2 are within 10%. It should also be noted that in practice the measured k_{eff}^2 is always smaller than the theoretical value, simply because the static capacitance causes a degradation of f_p to be closer to f_s.

3.2.3 The Static Capacitance C_0

Figure 3-7 illustrates a simple physical model which can be used to describe the capacitive feedthrough to ground in the one-port AlN Lamb wave resonators and the corresponding C_0 in the MBVD equivalent circuits for the resonators with the electrically single-IDT, grounded-bottom-electrode, floating-bottom-electrode, and double-IDT surface conditions, respectively. As depicted in Figure 3-7(a), the electric potentials in the IDT finger electrodes are presumed to be U and 0, and then the static capacitance C_{01} is simply equal to the lateral in-line capacitance C_l in the single-IDT topology. For the grounded-bottom-electrode topology shown in Figure 3-7(b), the lateral and vertical electric fields induce the inline capacitance C_l and the cross-field capacitance C_v so the static capacitance C_{02} is simply assumed to be the summation of C_l and C_v. As for the floating-bottom-electrode topology presented in Figure 3-7(c), the electric potential in the bottom electrode is not set, and the C_{03} is assumed to be the summation of C_1 and $C_2/2$ [72]. For the double-IDT topology shown in Figure 3-7(d), the lateral and vertical electric

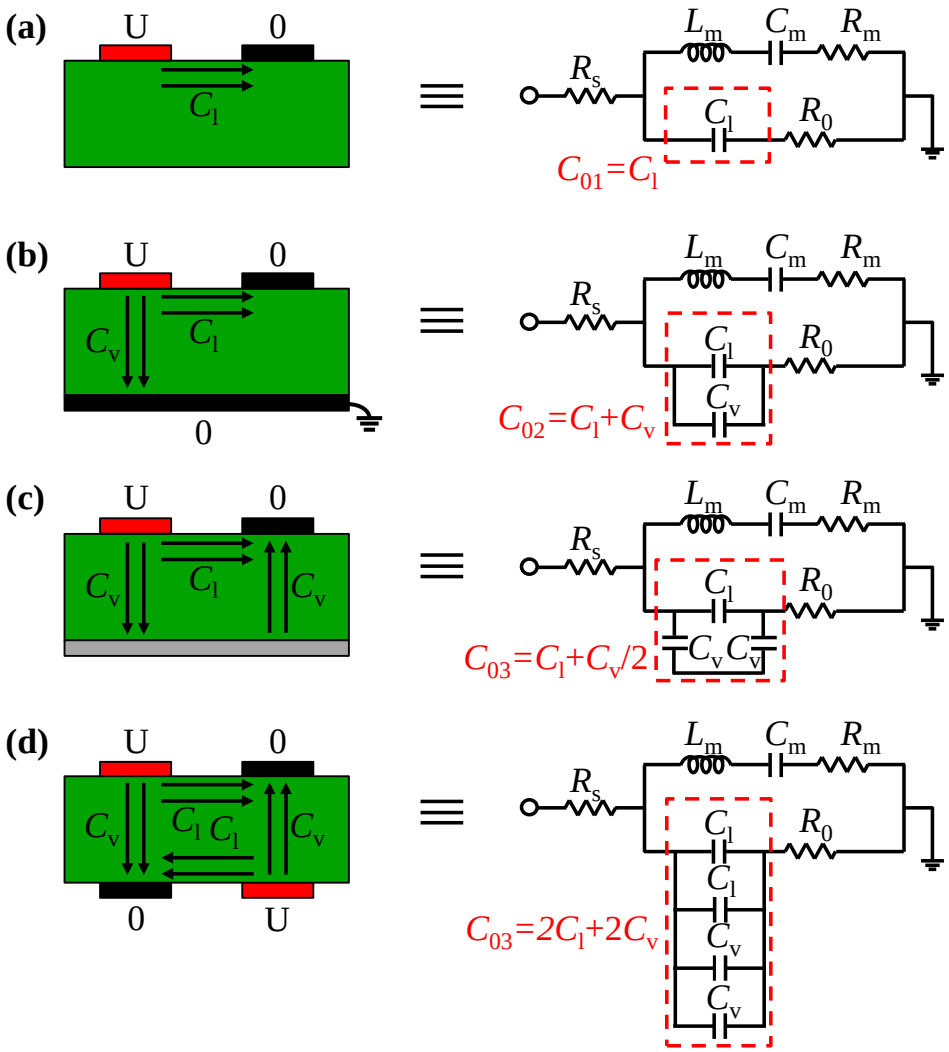

Figure 3-7. Simple physical models for the capacitive feedthrough to ground in the one-port Lamb wave resonators with one pair of IDT under different bottom surface conditions and the equivalent static capacitances in the MBVD equivalent circuits for the resonators with the (a) single-IDT, (b) grounded-BE, (c) floating-BE, and (d) double-IDT surface topologies, respectively.

fields happen in both ways and the static capacitance C_{04} is assumed to be the summation of $2C_l$ and $2C_v$.

The single-IDT topology would show weakest excitation efficiency and the double-IDT configuration the strongest. The excitation efficiency would be the same for the grounded-bottom-electrode and the floating-bottom-electrode topologies, but the static capacitance C_{03} for the floating-bottom-electrode case is smaller than the C_{02} for the grounded-bottom-electrode topology, resulting in a larger k^2_{eff} in the resonator with the floating bottom electrode.

As shown in Figure 3-8, when 0.2λ-thick AlN thin plates with periodic lateral boundary conditions are employed with different electrical configurations, the 2D FEA

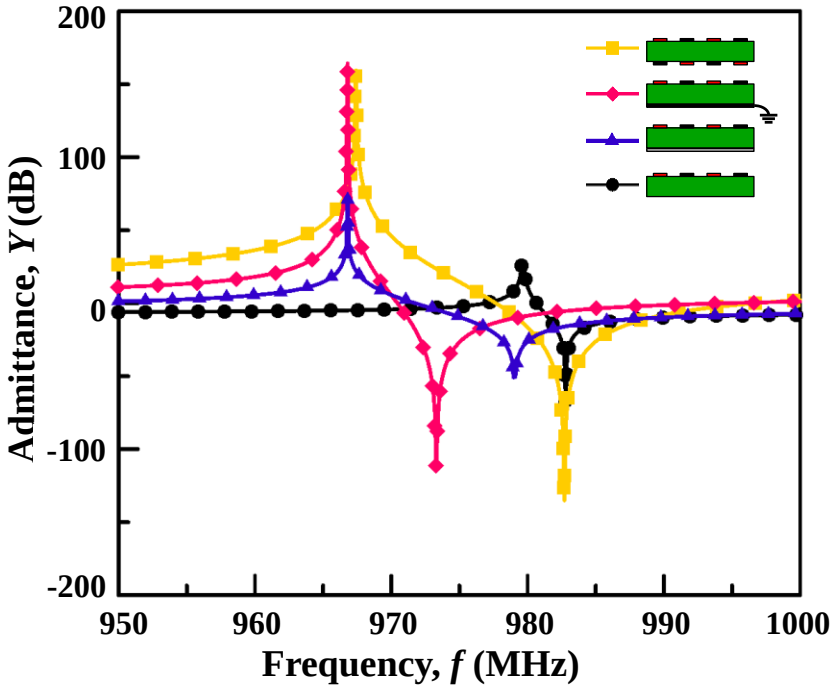

Figure 3-8. Simulated admittance spectra of the one-port AlN Lamb wave resonators with the single-IDT, grounded-BE, floating-BE, and double-IDT surface configurations using the 2D FEA model in COMSOL.

model predicts that the Lamb wave resonator with the double-IDT electrode configuration provides largest k^2_{eff}, the single-IDT case the smallest k^2_{eff} , and the floating-bottom-electrode topology offers a 1.8 times larger k^2_{eff} than that with the grounded bottom electrode. The existence of the bottom electrode (the grounded and floating bottom electrode topologies) also lowers the resonance frequency than the configurations only employing IDTs.

The simulation results also reveal that the static capacitance of the transducer with double-IDT is the largest, then the grounded-bottom-electrode type, the floating-bottom-electrode topology, and the single-IDT the smallest, which is in very good agreement with the approximation in Figure 3-7. The result confirms that even though the transduction efficiency of the IDTs over the floating and grounded bottom electrodes are the same, the smaller static capacitance of the floating-bottom-electrode configuration makes its k^2_{eff} larger than the grounded-bottom-electrode configuration.

3.2.4 General Electrode Configurations

As is mentioned in the previous chapter, although the double-IDTs configuration always offers the largest k^2 or k_{eff}^2, it requires much more complicated fabrication process which may consume more time and cost. As a result, the most widely used electrode configurations for the AlN Lamb wave resonators are the single-IDT type with relatively

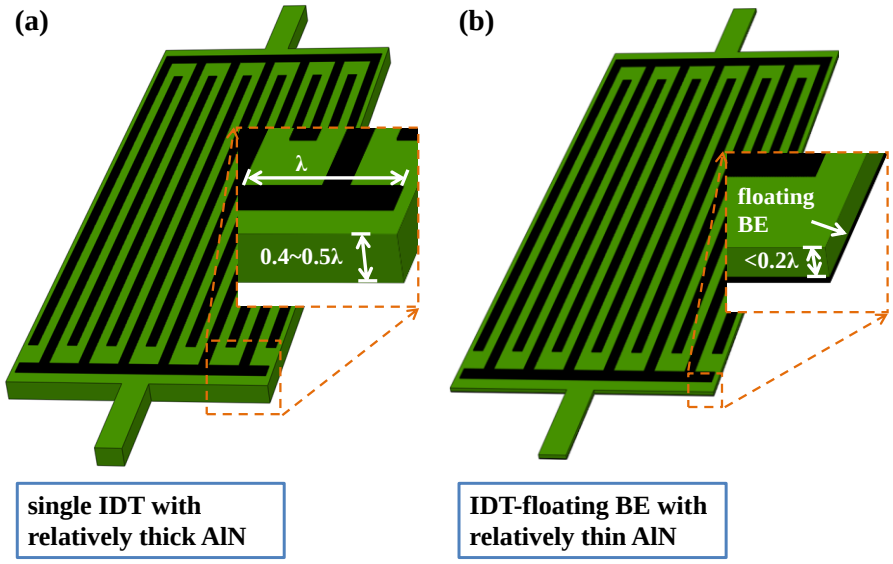

Figure 3-9. Simulated effective coupling of the Lamb wave S_0 mode using COMSOL for four electrode configurations: single-IDT, with a grounded bottom electrode, with a floating electrode, and double-IDT.

thick (h_{AlN}/λ ~ 0.4-0.5) AlN and IDT-floating BE type with relatively thin (h_{AlN}/λ < 0.2) AlN layer, shown in Figure 3-9, for they offer relatively large k^2 or k_{eff}^2 and simple fabrication process. More specifically, the former case (Figure 3-9 (a)) offers the large Q and the simplest fabrication process since the structure has only two layers, as well as medium k_{eff}^2 (~ 2% in Figure 3-6 (a)); the latter configuration offers very large k_{eff}^2 (~ 3.5% in Figure 3-4 (a)) as well as medium Q, and its frication process requires only 2 mask, much simpler than the IDT-grounded BE case which requires 4 mask involving the ground via.

3.3 Temperature Compensation Technique

Unlike quartz-based devices offering a variety of specific temperature compensation cuts for the bulk and surface acoustic waves, AlN exhibits the negative *TCE*, making it impossible to enable intrinsically temperature-compensated electroacoustic devices. The temperature compensation of the AlN-based devices is therefore achieved by employing thin film materials with opposite *TCF*. By adding a SiO_2 layer with a *TCF* of +85 ppm/°C onto the piezoelectric AlN layer, a robust temperature compensation approach for the LWRs on an AlN/SiO_2 bilayer plate has been successfully demonstrated at room temperature and high temperature, as shown in Figure 3-10 [68], [73].

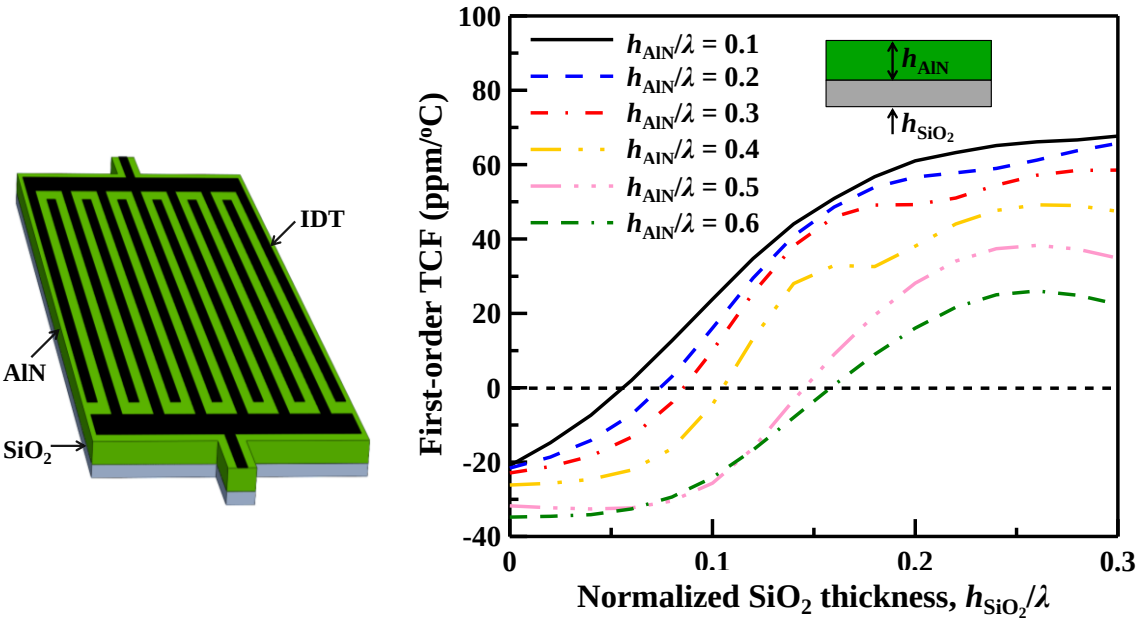

Figure 3-10. Illustration of the temperature compensated AlN/SiO_2 Lamb wave resonator and the calculated first-order *TCF*s for different AlN and SiO_2 thicknesses

Table 3-2. Material constants of AlN and SiO_2 used in the calculations. [69]

	Symbol	AlN	SiO_2	Units
Stiffness constants	C_{11}	345	78.5	(10^9 N/m^2)
	C_{12}	125	16.1	
	C_{13}	120	16.1	
	C_{33}	395	78.5	
	C_{44}	118	31.2	
	C_{66}	110	31.2	
Mass density	ρ	3260	2210	(kg/m^3)
Piezoelectric constants	e_{15}	–0.48	–	(C/m^2)
	e_{31}	–0.58	–	
	e_{33}	1.55	–	
Dielectric constants	ε_{11}	8.0	3.32	(10^{-11} F/m)
	ε_{33}	9.5	3.32	

Unfortunately, as is shown in Figure 3-11, the low elastic constants and non-piezoelectricity of the SiO_2 layer causes substantial reductions in the phase velocity and electromechanical coupling coefficient. Furthermore, the asymmetrical composite plate traps less acoustic waves in the AlN active layer so that the piezoelectric energy is

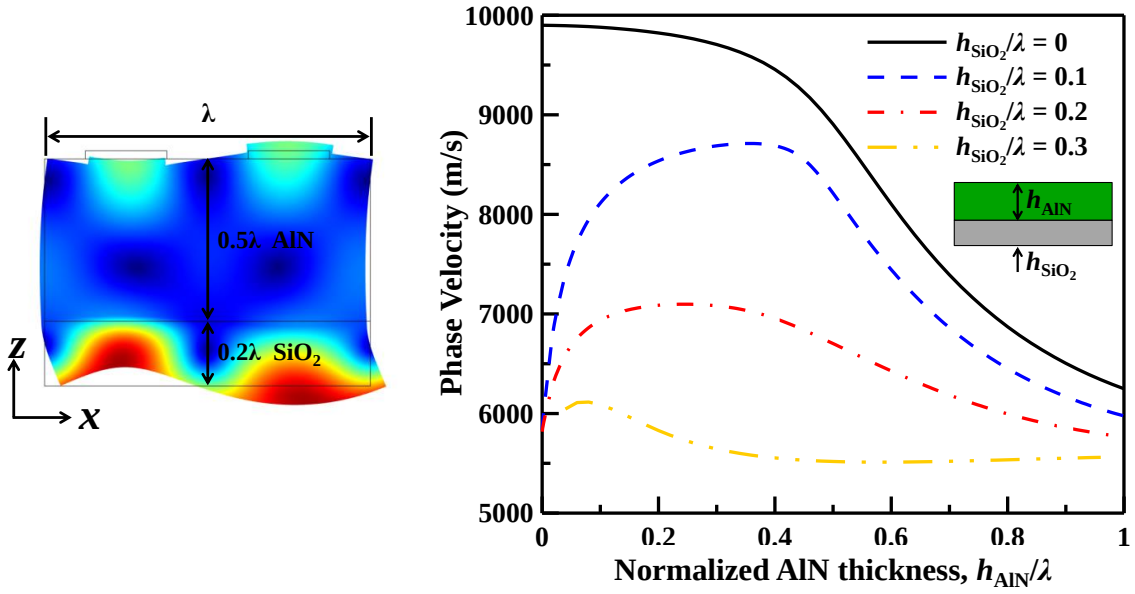

Figure 3-11. Calculated phase velocities of the Lamb wave S_0 modes for different AlN and SiO_2

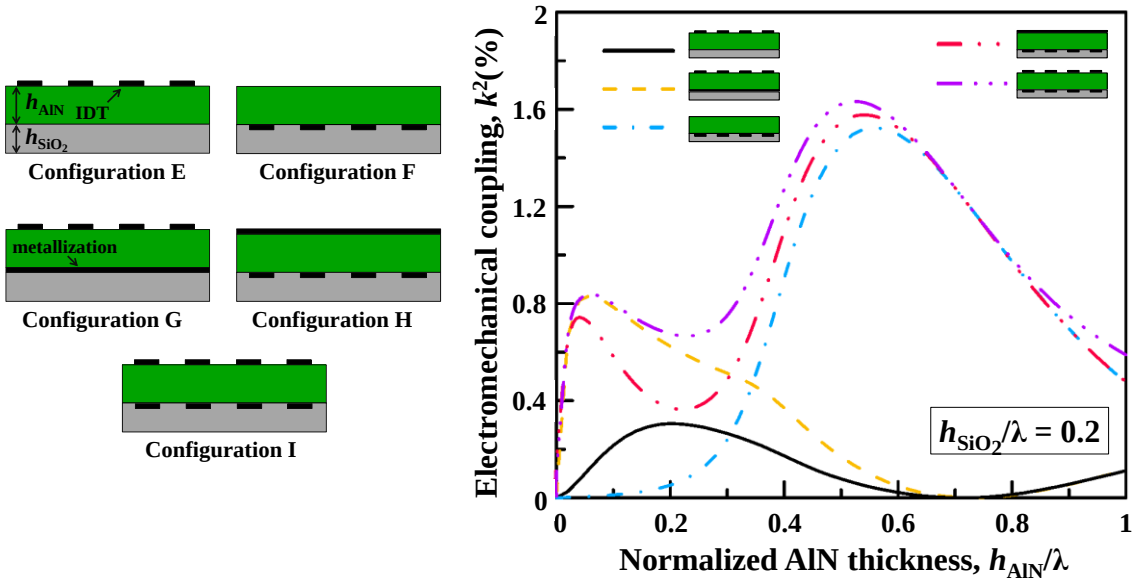

Figure 3-12. Calculated electromechanical coupling coefficients of the QS_0 mode for different electrode configurations listed when h_{SiO_2}/λ=0.2.

excited less efficiently to enable lower v_p and smaller k^2 for the S_0 Lamb wave mode in the AlN/SiO_2 membrane. Figure 3-11 also shows the phase velocities for different AlN and SiO_2 thicknesses calculated using the material parameters listed in Table 3-2. It is very clear that the adding layer of SiO_2 substantially lowers the phase velocity. When the normalized SiO_2 thickness reached 0.3, the phase velocity of the structure is almost halved compared to the pure AlN membrane.

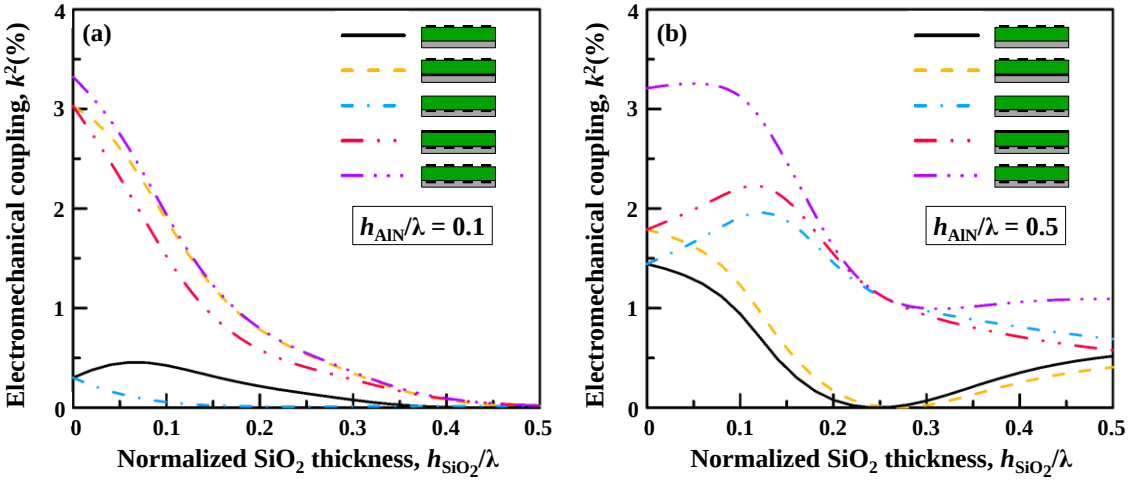

Figure 3-13. Calculated electromechanincal coupling coefficients for different electrode configurations at fixed normalized AlN thicknesses.

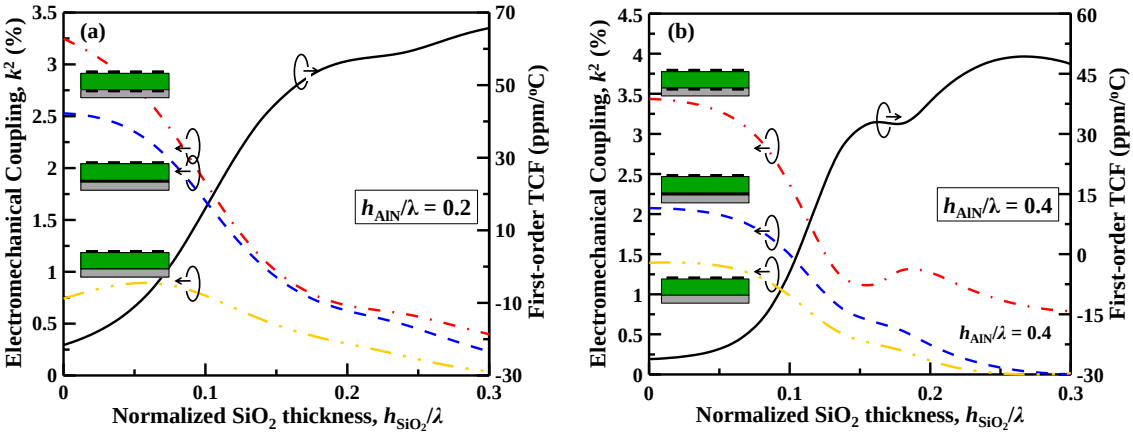

Figure 3-14. Trade-offs between the first-order *TCF* and intrinsic k^2 of the QS_0 mode in the AlN/SiO_2 bilayer when h_{AlN}/λ = 0.2 and h_{AlN}/λ = 0.4.

Because of the asymmetry in the z-axis direction, five different electrode configurations should be considered for the analysis of electromechanical coupling, as is listed in Figure 3-12, and the calculated electromechanical coupling from the material properties in Table 3-2 for a mostly used SiO_2 thickness 0.2λ is also given in the figure. It is obvious that the double-IDT configuration always exhibit the largest coupling, the configurations when the IDTs are placed in the outer surface of AlN shows a larger coupling when the normalized AlN thickness is around 0.55, and the configurations when the IDTs are placed in the interface of AlN and SiO_2 shows a larger coupling when the normalized AlN thickness is around 0.05.

Figure 3-13 also compares the electromechanical coupling for different electrode configurations but at fixed normalized AlN thicknesses, which indicate that for thin AlN

the bottom electrode is highly preferred and for thick AlN placing the IDT at the interface can largely increase the k^2.

Furthermore, the trade-offs between the *TCF* and k^2 can be observed in the same propagation medium. As shown in Figure 3-14, when the k^2 on the AlN/SiO_2 composite membrane achieve a locally minimum, it exhibits a locally maximal *TCF*, and vice versa, revealing the trade-off between the *TCF* and k^2 in the piezoelectric LWRs [74].

The above discussions indicate that a correct transducer configuration with proper selections of the AlN and SiO_2 thicknesses enables the AlN/SiO_2 LWRs to have high phase velocity, large intrinsic electromechanical coupling coefficient, and good temperature-frequency stability at high temperatures.

An improved temperature technique will be introduced in Chapter 6 based on the symmetric AlN/SiO_2 sandwiched structure to enable better overall performance at near-zero *TCF*s.

Except for SiO_2, tellurium dioxide (TeO_2) [75] and highly-doped Si [76], [77] layers were also used as the compensating material. Recently, fluorine-doped silicon oxide (SiOF) was found to have better temperature compensation efficiency than undoped SiO_2 films [78]. TeO_2 and SiOF both have larger positive *TCF*s than SiO_2, meaning thinner compensation film will be needed to get zero *TCF* for a certain thickness of AlN than SiO_2, but they are difficult of deposit and new etching process also need to be set up.

3.4 Microfabrication Process

3.4.1 The Process Flow

The fabrication process employed for manufacturing the AlN Lamb wave resonators is based on surface micromachining techniques, which are compatible with the CMOS processes. A baseline two-mask fabrication process is described to manufacture the AlN LWRs with single-IDT using Pt electrodes. The fabrication process could be easily modified for other bottom electrode metals, such as Mo, Al, or W. If the grounded bottom electrode is included, the fabrication process could be a four-mask process. Given that the bottom electrode is unnecessary to be grounded as discussed in section 3.2, the fabrication process steps would be further reduced to a three-mask process for the AlN LWRs with floating bottom electrodes. All the resonators in this thesis use the single-IDT configuration, so the two-mask process is introduced as followings.

First, as shown in step 1 in Figure 3–15, a 300-nm-thick LSN layer was deposited on Si (100) wafers in a LPCVD furnace under 835°C. The LSN stress depends on the film thickness and the film stress is around 300 MPa while the LSN thickness is 300–500 nm. The LSN layer is used for the electrical isolation with the Si substrates and eliminates unwanted current feedthrough and substrate losses.

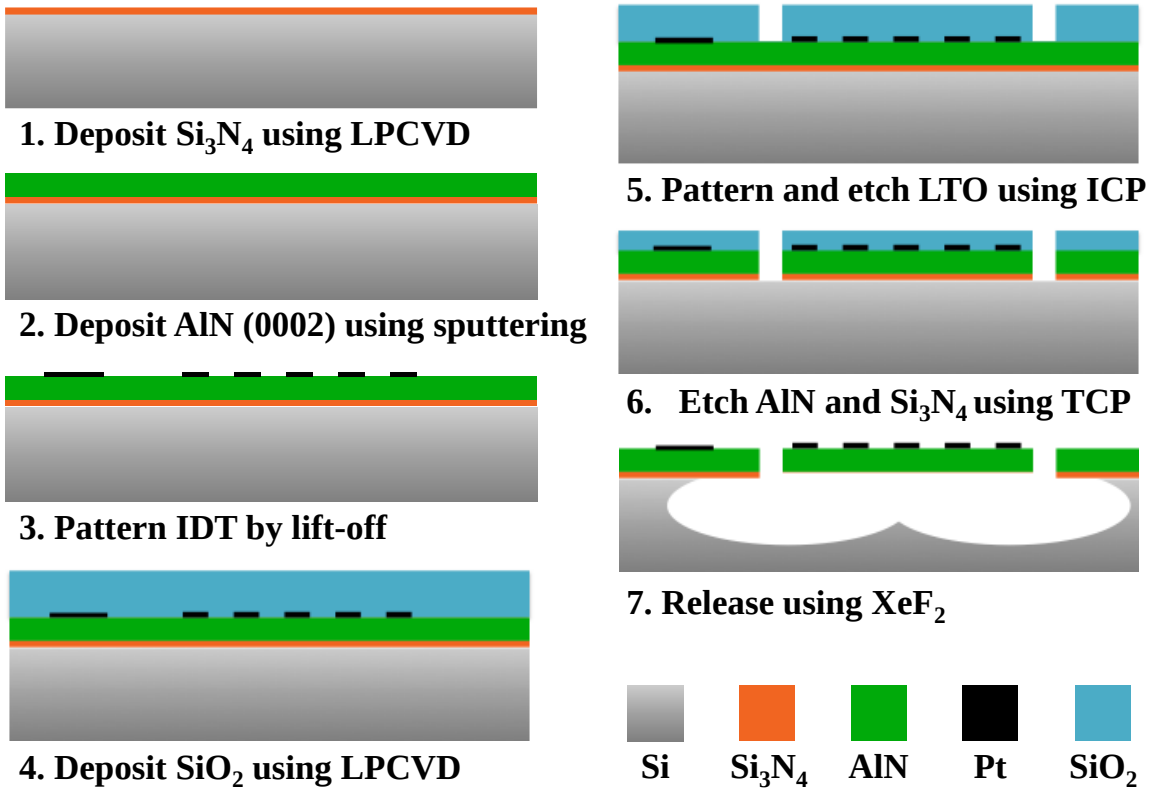

Figure 3-15. Cross-sectional process flow of the single-IDT AlN LWRs.

A highly c-axis oriented AlN thin film was deposited at 300°C in a Tegal multi-chamber dual ring sputtering system (Endeavor-AT sputtering tool) [79] locate in the Berkeley Marvell Nanofabrication Laboratory. After pumping to a base pressure below $2x10^{-6}$ Torr, an in-situ surface treatment of the substrate under low-power RF environment is conducted prior to AlN deposition to remove native oxide and reduce the roughness of the surface. The process atmosphere is a mixture of the controlled constant flow of argon and nitrogen gases. The argon plasma is used to bombard the surface materials off from a high purity Al target. The sputtered Al ions react with N_2 molecules to form AlN and then sputtered to the substrate by a potential difference between the target and the substrate where the target serves as the cathodes, while the substrate wafer acts as the anode [80]. The process enables the formation of columnar AlN thin film exhibiting strong (0002) texture on the silicon nitride or silicon substrate. However, if there are slopes or steps on the substrate, the growth tends to have random orientation and poor step coverage around that area. In the dual cathode S-Gun magnetron, regulation of the flux of the charged particles from AC (40 kHz) plasma discharge to the substrate enables effective control of both the AlN film crystallinity and the film intrinsic stress. An external stress control unit (adjustable high power resistor) provides coarse control of the film residual stress, while a 13.56 MHz RF-bias system and the gas flow rates of N2 and Ar provide a fine tune of the residual stress. The A thin film stress abruptly changes from high compressive tress in relatively thin film (below 500 nm) to tensile stress with thickness near 1,000 nm.

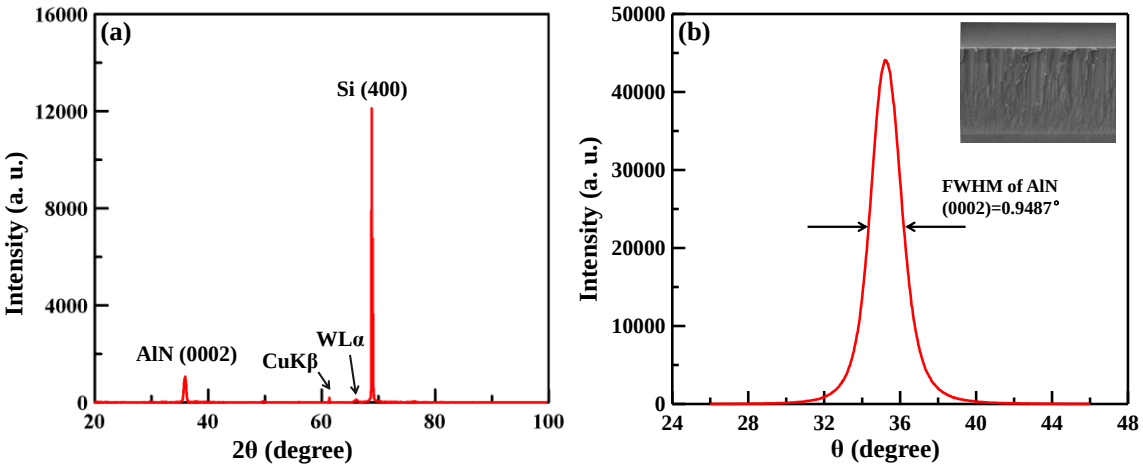

Figure 3-16. XRD (a) normal-couple scan and (b) rocking curve measurement of 4-μm thick AlN thin film deposited with nearly zero stress.

The electromechanical coupling strength and quality factor is strong correlated to the crystalline orientation of the AlN. The correlation between k^2_{eff} and AlN grain orientation has been found and suggests that maximum coupling can be achieved if the rocking curve FWHM value of the AlN film is below 2°. In Figure 3-16 a typical normal coupled scan and a rocking curve scan of an AlN thin film deposited on a silicon nitride substrate are shown. The diffraction pattern from a highly c-axis oriented AlN thin film shows a peak at 2θ = 36.4° in the normal coupled scan, and a minimum FWHM value of the 0002 rocking curve centered at ω = 18.2°. These crystalline characterizations are done using a Siemens D5000 X-ray Diffractometer. Moreover, the residual stress of the AlN thin film can be measured by a laser interferometer (tool "flexus" in Berkeley Marvell Nanofabrication Laboratory), determining the curvature of the whole 4 inch wafer before and after the deposition of the AlN thin film. By adjusting the AC power or the Ar and nitrogen (N_2) flow rates, the residual stress of the deposited AlN thin film can be controlled within tensile and compressive 100 MPa. It should be noted that the AC power and the gas flow rate also influence the deposition rate and the uniformity of the AlN thin film on the whole wafer.

Then, a 180-nm-thick platinum (Pt) layer on a 20-nm-thick chromium (Cr) adhesion layer was sputtered on the AlN thin film. Consequently dual photoresist layers were coated and patterned for the lift-off process of the top finger electrodes on the AlN thin film as shown in step 3 in Fig. 3–15.

Prior to the dry etching of the AlN thin film, as shown in step 4, a LTO layer was deposited using LPCVD at around 400°C, patterned using C_4F_8-based inductively coupled plasma (ICP) etching, and used as the hard mask for the following AlN etching process, as depicted as step 4 and 5.

The photoresist used to define the patterns of the LTO hard mask has to be removed after the LTO dry etching step as the photoresist would generate some organic byproducts on the sidewalls in the dry etching chamber. The AlN film was patterned by

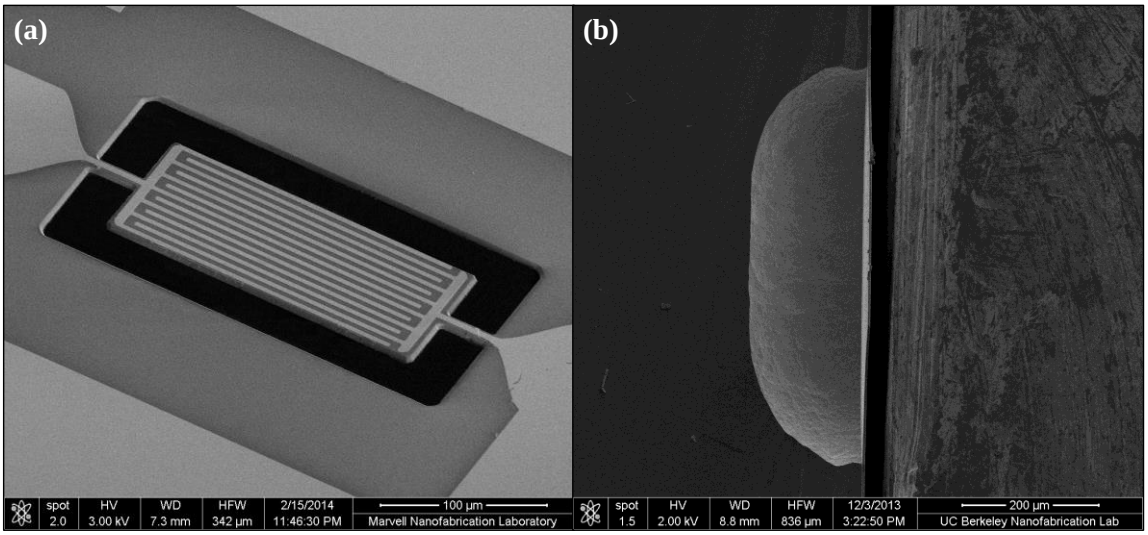

Figure 3-17. SEM image of the fabricated Lamb wave resonator and the air cavity structure.

Cl_2-based transformer coupled plasma (TCP) etching as depicted in step 6 in Figure 3–15. Based on the above etching recipes, the Cl_2-based TCP etching selectivity of AlN to LTO is around 2.5. In addition to the etching rate, the sidewall of the AlN layer is critical for the performance of the LWRs, especially for the spurious mode issue. In order to achieve vertical the sidewalls of the AlN layer, the LTO hard mask should have sidewalls as vertical as possible since the sidewall angle of the LTO layer would be transferred to the AIN sidewalls. The Cl_2-based TCP etching yields a sidewall angle of roughly 82° for the AlN thin film [81].

A CF_4-based reactive ion etching (RIE) process was used to remove the remaining oxide hard mask. Finally, as shown in step 7 in Figure 3–15, the AlN plate structure was released by using xenon difluoride (XeF_2)-based isotropic dry etching of the Si substrate, and the LSN layer beneath the AlN layer can be also removed by XeF_2 during the device release process.

Fig. 3-12 (a) shows the SEM images of the resonators on the 4-µm-thick AlN membranes and Figure 3-17 (b) presents the released air cavity.

3.4.2 Possible Failures

Broken anchor

The most commonly seen failure in the Lamb wave resonators is the broken anchors. As is shown in Figure 3-18, the anchor can broke in the middle (a), from the anchor-substrate interface (b), and from the anchor-device interface. This can be largely avoided in two approaches: 1. from the design side try not to design too thin and short anchors, and not too large devices since large and heavy resonators are tend to break the

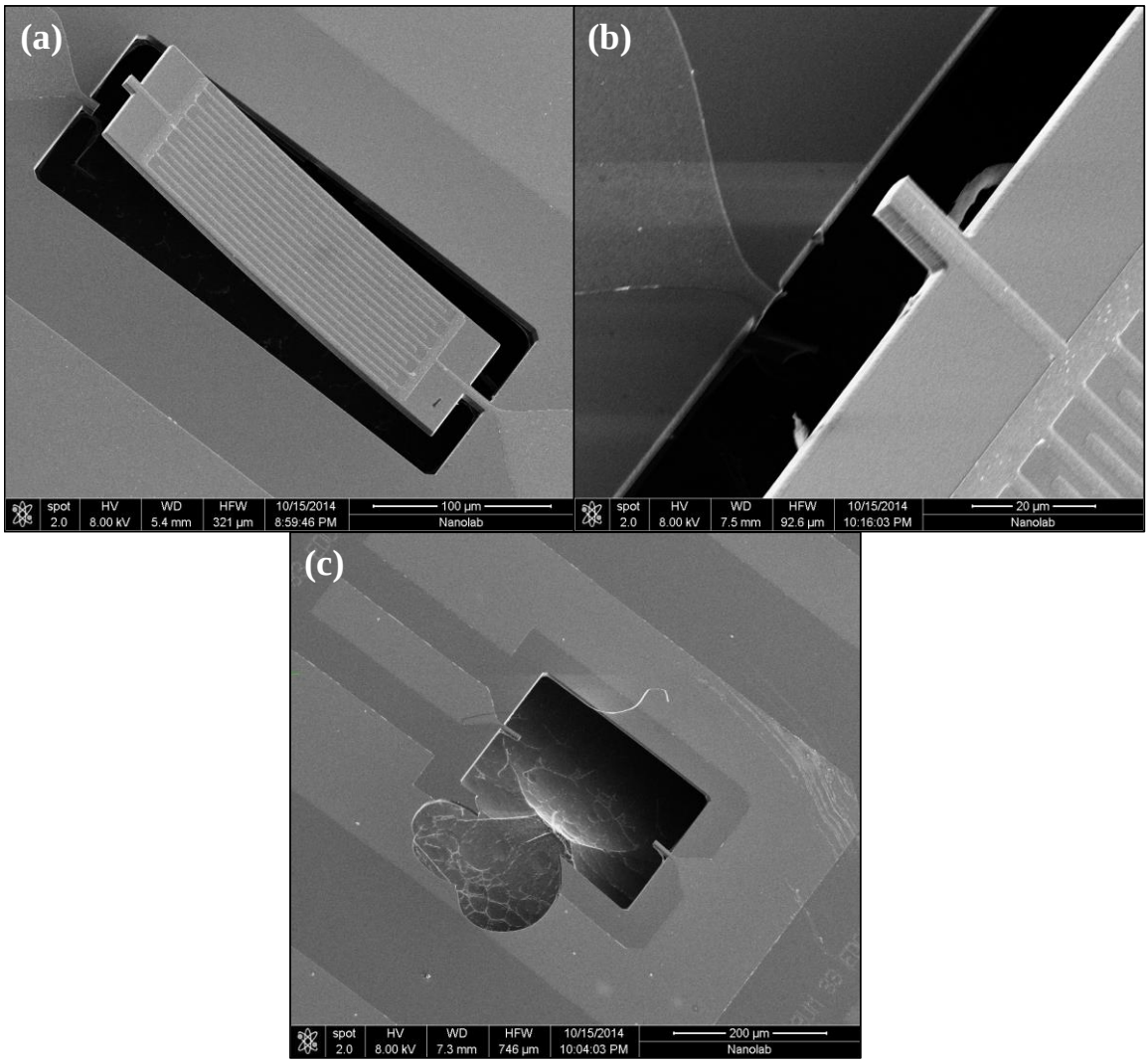

Figure 3-18. SEM image of the fabricated Lamb wave resonator with broken anchors: (a) anchor broken in the middle, (b) anchors broken from the anchor-substrate interface, and (c) anchor broken from the anchor-device interface.

supporting tethers; 2. from the fabrication side try to minimize the stress in the AlN and metal layer. By carefully designing the geometry and optimize the fabrication process, these type of failures can be largely minimized. Otherwise all the devices can be broken on a wafer in the worst case.

Bad lift-off

As shown in Figure 3-19 (a), sometimes the metal electrodes stick to the AlN layer and not fully shaped by lift-off. The device performance will be largely deteriorated if the IDT fingers are not separated. The Figure 3-15 (b) shows the well-shaped IDT electrodes using lift-off. The width of the IDT finger should be equal to the width of the separation, since we use the IDT of 50% metal cover ratio.

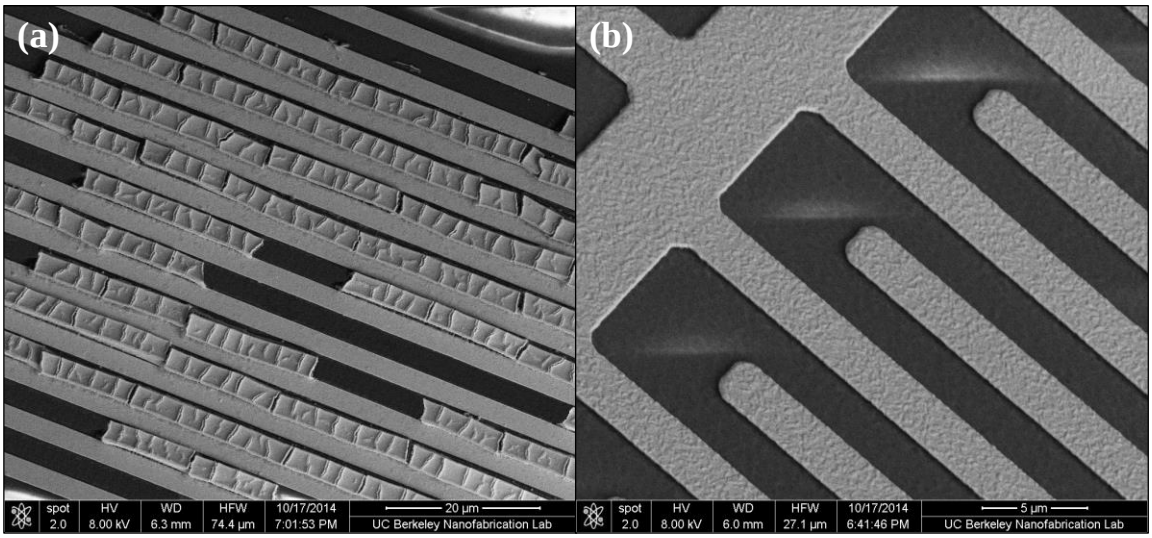

Figure 3-19. SEM image of the fabricated Lamb wave resonator with broken anchors: (a) bad lift-off IDTs, (b) .good lift-off IDTs

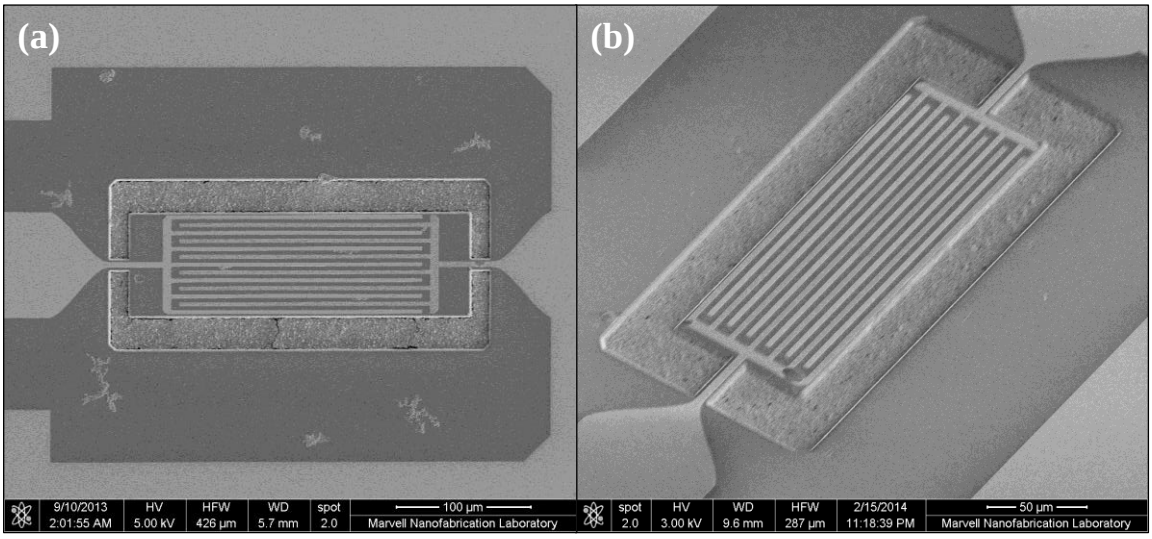

Figure 3-20. SEM image of the fabricated Lamb wave resonator with AlN layer not etched through.

Generally the metals that are evaporated are much easier to lift-off than sputtered and light metals like Al are not as sticky as heavy metals like Pt. Nevertheless, with careful lithography process step before the deposition of the metal and a long time of soak and ultrasonic in the solution, it is achievable to totally avoid this type of failure.

Etching Depth

Another problem that engineers widely encounter is getting the precise thicknesses of etching depth. One set of device that I have made are with residual AlN, as shown in Figure 3-20. The residual AlN layer connected the device to the substrate and thus largely

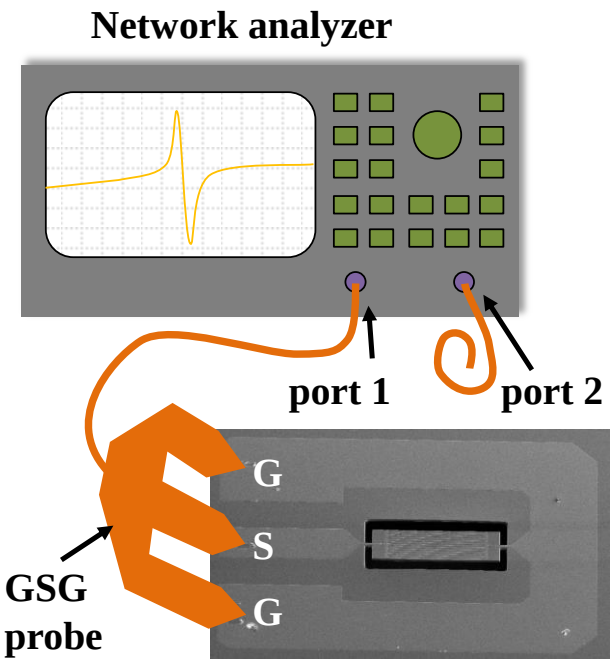

Figure 3-21. Testing setup used in this dissertation. Devices are probed by GSG probes connecting to a vector network analyzer directly.

decrease the *Q* and other performance parameters. Since the XeF_2 gas went through this very thin residual layer and successfully released the structure, these residual layers were found only after the bad measurement data was got and went back to do the SEM. Although this simple fabrication process does not include the precise etching depth, careful calculation is still needed before the etching to avoid the residual and at the same time not leave the wafer in the etching chamber for too long and harm the devices.

On the other hand, deposition with precise thicknesses and maximum flatness is also required to ensure good device performance and the yield. The other problems that need to pay attention are like the stress, wall straightness, contamination and so on.

3.5 Testing Setup

All AlN Lamb wave resonators studied in this dissertation are measured in a Janis RF probe station, with 200 μm micro-manipulated ground-signal-ground (GSG) probes from Cascade (Model ACP40-AW-GSG-200). A short-open-load-through (SOLT) calibration is performed on a precision reference substrate prior to the testing for a 50 Ω termination. All tests in this dissertation are performed in air at atmospheric pressure and ambient temperature.

The micro-acoustic frequency response characteristics of AIN Lamb wave resonators are measured directly using an Agilent E5071B vector network analyzer (VNA) with 0 dBm (1 mW) of signal power, as shown in Figure 3-21. All of the measured results are reported exactly as measured, without subtracting the parasitics are subtracted or de-embedding at the ports. All the resonators in this dissertation are one-port devices, so only S_{11} reflection parameters are recorded by the network analyzer. The admittances are calculated using equation (3.9):

$$Y_1 = \frac{1}{Z_0}\frac{1-S_{11}}{1+S_{11}}, \tag{3.9}$$

where the characteristic impedance $Z_0 = 50\ \Omega$ as the standard reference.

Then, the performance parameters can be calculated and equivalent circuit parameters can be extracted by fitting into the MBVD model discussed previously.

For two-port Lamb wave resonators, one can just connect one side of IDT to one port and one port to the other. S_{11} and S_{22} can be considered as return loss, or the input and output impedance mismatch respectively, while S_{12} and S_{21} are interpreted as power gain/loss in forward and reverse directions, respectively.

Chapter 4

Influence of Electrode Materials and Thicknesses on AlN Lamb Wave Resonator Characteristics

The Lamb wave resonators usually show a moderate k^2_{eff} of around 3% due to the lack of careful selection of the electrode configurations, materials, and thicknesses. So an optimization on the electrodes of the piezoelectric AlN Lamb wave resonators is highly desirable to further enable the high-f_s and large bandwidth filters. Although the technology about electrodes is mature for SAW resonators and FBARs, there hasn't been systematic study of the electrode materials for Lamb wave resonators. As the Lamb wave has dispersive characteristics, it will be different from SAWs and FBARs and more complicated. This study adopts the finite element analysis (FEA) to investigate the influence of electrodes on the dispersive characteristics of the S_0 mode propagating in the multi-membranes. The effects of electrodes configurations, AlN film thicknesses, electrode materials and electrodes thicknesses on the performance of Lamb wave resonators are also explored.

Four types of electrode configurations for the AlN Lamb wave resonators are considered here: the single-IDT type, the IDT with a floating bottom electrode type, the IDT with a grounded bottom electrode type, and the double-IDT type, as shown in Figure 1. Each electrode configuration has been widely explored and reported recently. For each electrode configuration, the impact of the metal electrodes on the phase velocities and effective coupling coefficients are calculated and analyzed in this study. The density (ρ), equivalent acoustic impedance (Z'), and equivalent phase velocity (v_p') of the metal are the main factors that directly impact the characteristics.

4.1 Electrode Materials

4.1.1 The phase velocity

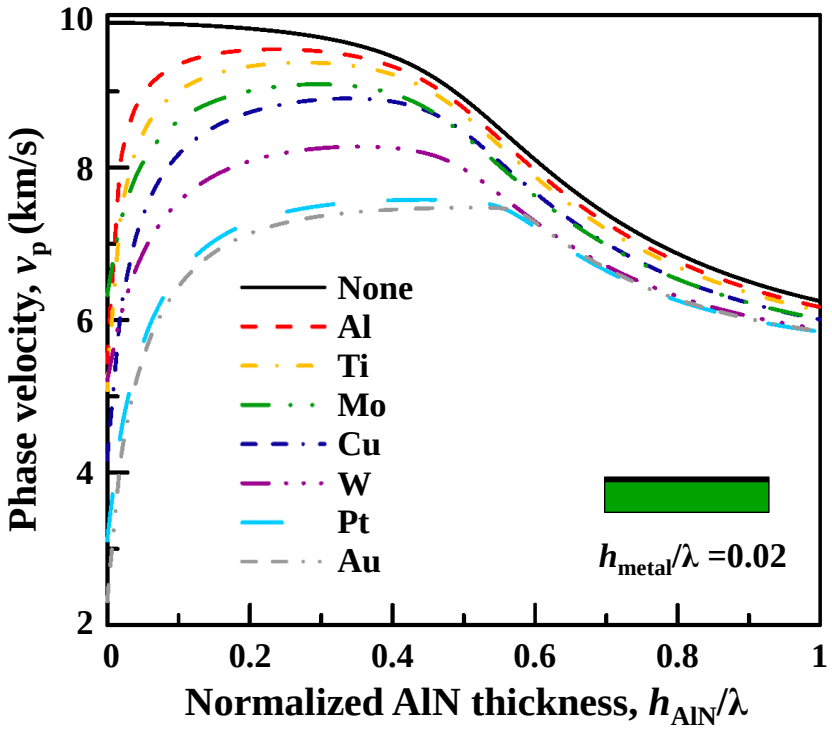

Figure 4-1. FEA simulations of phase velocities of the AlN Lamb wave resonators with different IDT electrodes when the electrode thickness is equal to 0.02λ.

The impact of different electrode materials on the phase velocity when $h_{metal}/\lambda = 0.02$ is shown in Figure 3 (a).The material constants used for calculation are listed in table 2. It is intuitive that heavier metal has stronger loading effect on the phase velocity, which is the case when the AlN is relatively thick ($h_{AlN}/\lambda > 0.5$), in which case the decrease of the phase velocity is proportional to the metal density.

Table 4-1. Material constants of AlN and metal materials used in the simulations [82].

	Symbol	AlN	Al	Ti	Mo	Cu	W	Pt	Au	Units
Stiffness constants	C_{11}	345	111	166	462	211	590	374	220	(GPa)
	C_{12}	125	59	92	158	107.8	200	251	160	
	C_{44}	110	261	44	109	51	135	77	30	
Mass density	ρ	3260	2700	4500	10200	8960	19250	21400	19300	(kg/m^3)
Young's modulus	E	345	70	116	312	120	489	168	70	(GPa)
Equivalent phase velocity	v'_p	10290	5090	5070	5530	3650	5040	2800	1900	(m/s)
Acoustic impedance	Z	1061	436	722	1784	1037	3067	1896	1162	(C/m^2)

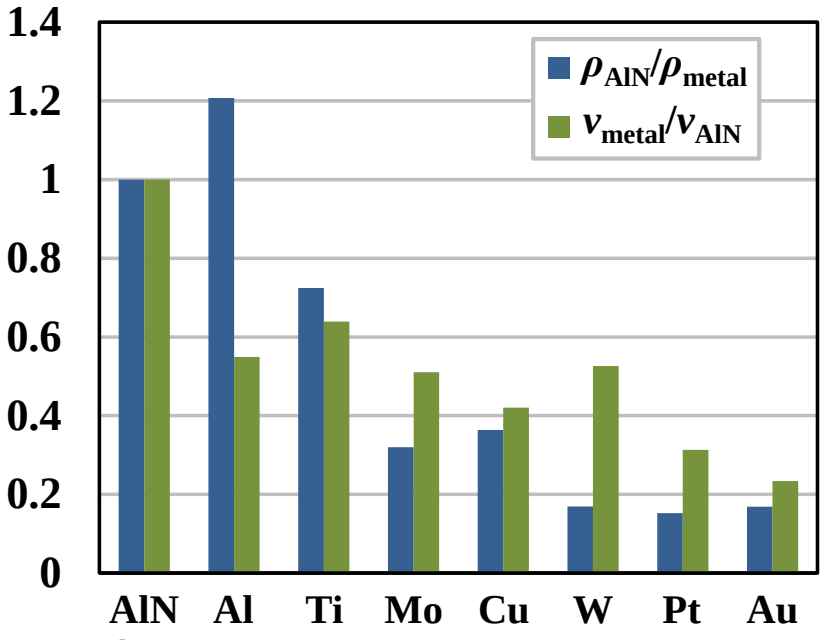

Figure 4-2. FEA simulations of phase velocities of the AlN Lamb wave resonators with different IDT electrodes when the electrode thickness is equal to 0.02λ.

When the AlN is thin ($h_{AlN}/\lambda < 0.1$), the stiffness of the metal also impact the loading effect, and the Lamb wave phase velocity in the bilayer is proportional to the equivalent phase velocity in the metal. Here we define the equivalent phase velocity as:

$$v_p' = \sqrt{\frac{E}{\rho}} \tag{4.1}$$

It should be noted that the v_p here is not the actual phase velocity of the Lamb wave or other wave modes. Since the Lamb wave phase velocity dependent on several stiffness constants, it is difficult to compare it with different metal materials. However, the Young's modulus is usually in the same level of the stiffness constants, so we simply the problem here and use the Young's modulus to calculate the equivalent phase velocity for comparison here.

The density of the metal materials inversely normalized to AlN and the equivalent acoustic velocity for the metals normalized to the equivalent acoustic velocity of AlN are shown in Figure 4-2. Comparing the v_p of different metal materials in Figure 4-1 to the densities and acoustic velocities in Figure 4-2, it can be observed that when the AlN is relatively thin ($h_{AlN}/\lambda < 0.2$), the v_p is in positive correlation with the normalized acoustic velocity v_{metal}/v_{AlN}, implying that the phase velocities in the multilayers are limited by the acoustic velocity in the metals. On the other hand, when the AlN is relatively thick ($h_{AlN}/\lambda > 0.5$), the phase velocities shown in Figure 4-1 are proportional to the inversely normalized density of the metals ρ_{AlN}/ρ_{metal}, indicating the heavier metal has stronger loading effect on the phase velocity.

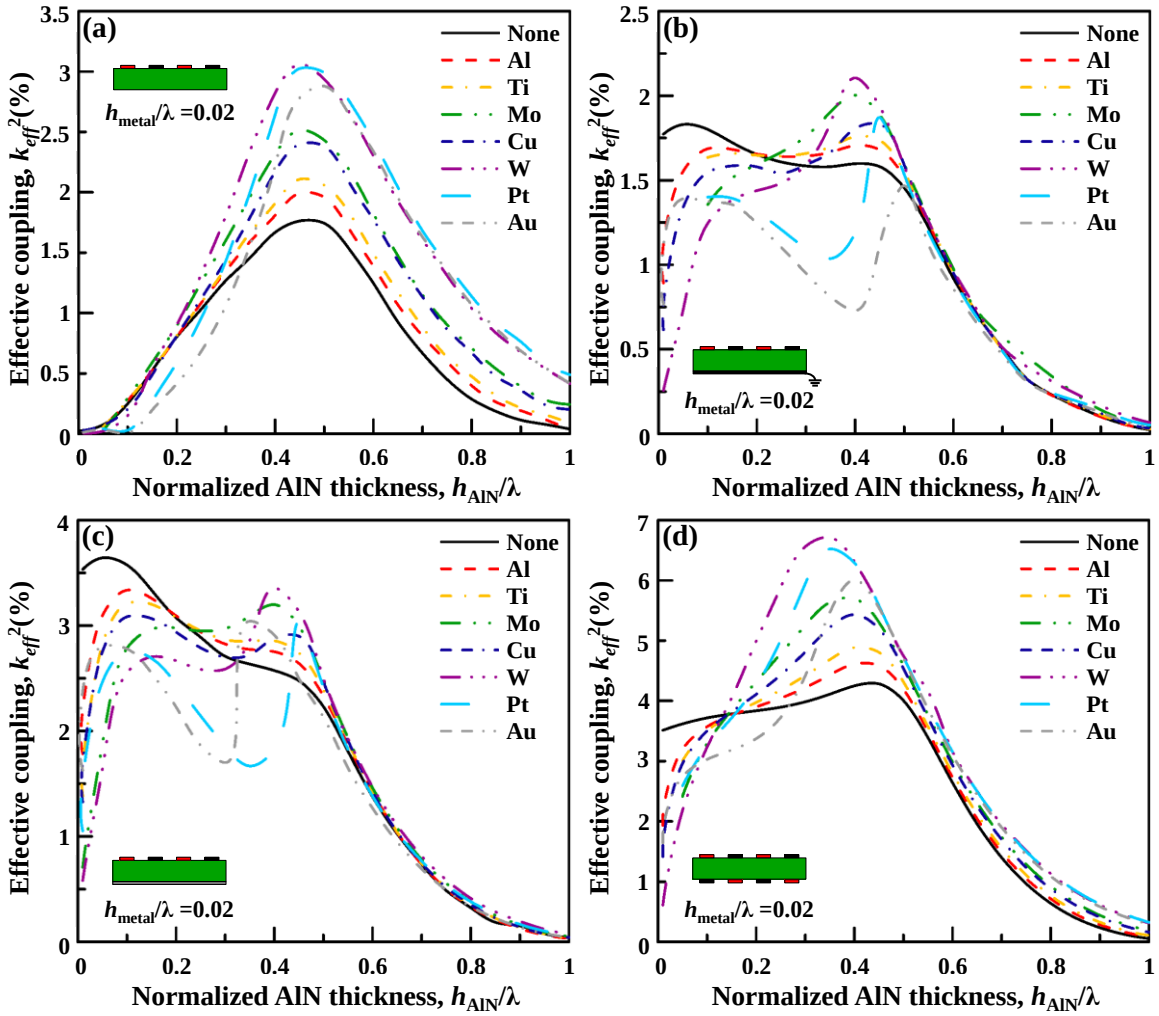

Figure 4-3. FEA simulations of effective coupling coefficients of AlN Lamb wave resonators for the (a) single IDT electrode configuration, (b)the IDT-grounded BE electrode configuration, (c) the IDT-floating BE electrode configuration, and (d) the double-IDT electrode configuration when the electrode thickness is equal to 0.02λ.

When the thickness of AlN is medium (h_{AlN}/λ = 0.1~0.5), the loading effect of the metal layer is not proportional to the density or the equivalent phase velocity, but the effect of both factors. As the equivalent phase velocity in the metal is proportional to stiffness and inversely proportional to the density, heavy and soft metals load the phase velocity more in general.

4.1.2 Electromechanical Coupling Coefficient

Figure 4-3(a)-(d) show the effect of different electrode materials on the effective coupling coefficients of the Lamb wave resonator with different electrode configurations. It is apparent that the electrode layers decrease the k^2_{eff} when AlN is very thin and enhance the k^2_{eff} when AlN becomes thick. When the AlN is thin, the piezoelectric-dead metal deviate the acoustic wave field away from the piezoelectric AlN layer and thus

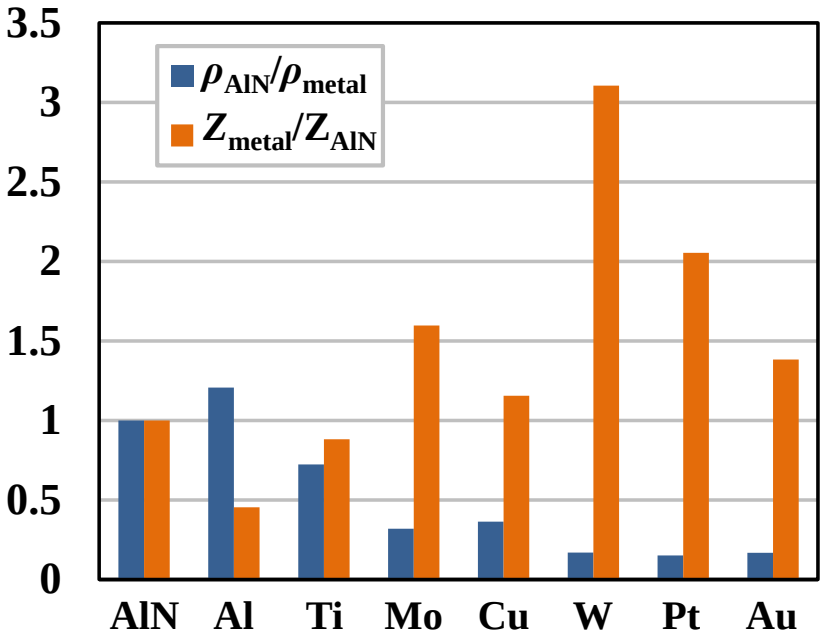

Figure 4-4. FEA simulations of phase velocities of the AlN Lamb wave resonators with different IDT electrodes when the electrode thickness is equal to 0.02λ.

reduce the k^2_{eff}, and the heavier metal have stronger loading effect. When the AlN becomes thick, the existence of the metal layer can boost the k^2_{eff} due to the large acoustic impedance, and the strength of k^2_{eff} is proportional to the acoustic impedance of the metal. The equivalent acoustic impedance can be calculated from [83], [84], [86]:

$$Z = \sqrt{E\rho} \tag{4.2}$$

Again, we use the Young's modulus instead of the stiffness constant here calculate the effective acoustic impedance for directly comparing different metal materials.

The density and acoustic impedance for different metals normalized to the density and acoustic impedance are shown in Figure 4-4. Comparing the k^2_{eff} of different metal materials in Figure 4-3 to the densities and acoustic impedances in Figure 4-4, it can be found that when the AlN is relatively thin ($h_{AlN}/\lambda < 0.2$), the k^2_{eff} is in positive correlation with the reverse normalized density ρ_{AlN}/ρ_{metal}, indicating the loading effect of the metal electrodes on the k^2_{eff} is proportional to the density of the metal. On the other hand, when the AlN is relatively thick ($h_{AlN}/\lambda > 0.4$), the strength of the k^2_{eff} in Figure 4-3 is in positive correlation with the normalized acoustic impedance Z_{metal}/Z_{AlN} of the metal material, implying that the large difference between the acoustic impedance of the metal and AlN enhance the k^2_{eff} proportionally.

It is interesting to notice that for the single-IDT and double-IDT type (Figure 4-3(a), (d)), the k^2_{eff} is largely improved if large-acoustic-impedance material is used. Especially

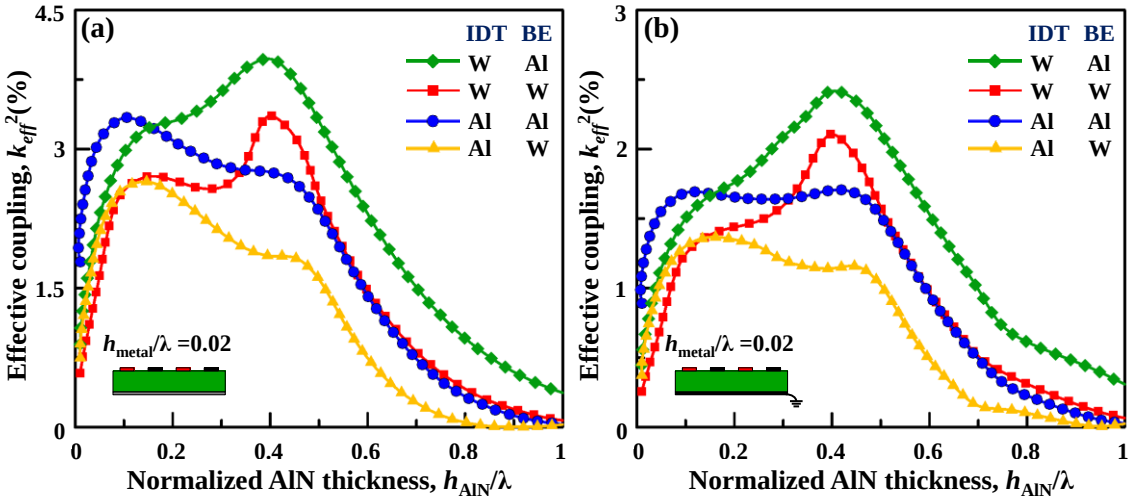

Figure 4-5. Calculated effective coupling coefficients of AlN Lamb wave resonators with the IDT-floating BE configuration using different combinations of electrode materials (Al, W) for the IDT and bottom electrodes.

for the double-IDT configuration, the k^2_{eff} can be boosted to near 7%, showing potential to enable very large coupling resonators.

4.1.3 Different Materials Combination

It can be noticed that for the electrode configurations that with a bottom electrode: the grounded and floating BE type, the coupling coefficients are not increased as much as the single-IDT and double-IDT configurations, this is due to the strong loading effect of the bottom electrode layer. Although the floating bottom electrode increase the k^2_{eff} a large amount from the single-IDT type for the pure AlN, the additional heavy metal layer draw the k^2_{eff} back intensively. Therefore, light metal can be used for the bottom electrode while the large-acoustic-impedance metal employed in the IDT to get the largest k^2_{eff}.

To demonstrate this approach, the k^2_{eff} is compared for different combinations of W and Al as the IDT or bottom electrode material, since Al has small density and small acoustic impedance while W has large density and large acoustic impedance. Figure 4-5 presents the comparison of different metal material combinations for the grounded and floating bottom electrode types, showing good agreement with the previous analysis. When AlN is very thin, the k^2_{eff} simply depends on the density of the metal material. As AlN becomes thick, when large-acoustic-impedance material as the IDT while light metal (Al) as the bottom electrode, this combination gives the largest k^2_{eff}.

As a result, light (low ρ) metals are preferable to be chosen as the bottom electrode and large acoustic impedance metals are suitable for IDTs in general to ensure a large k^2_{eff}.

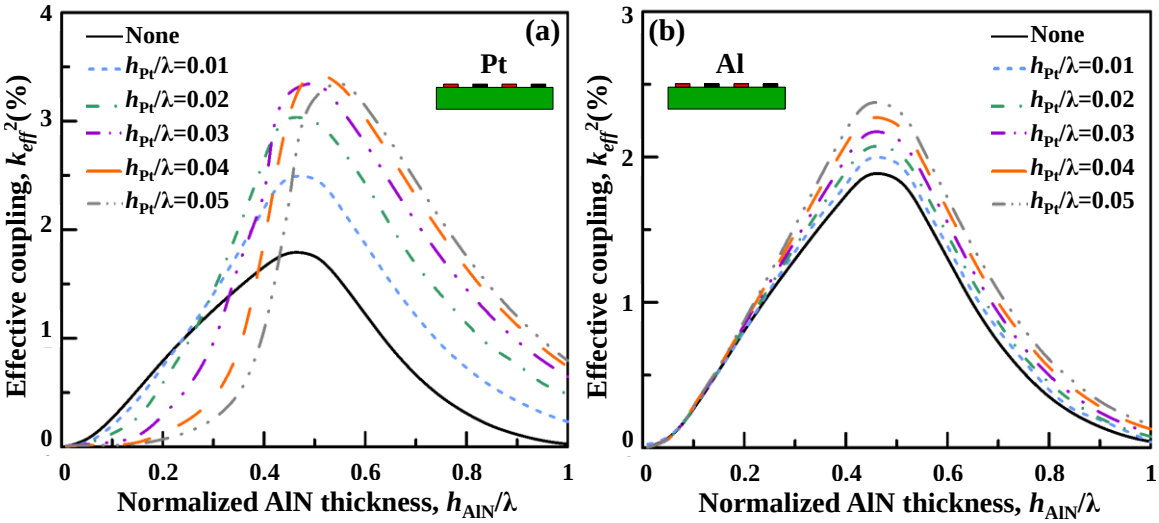

Figure 4-6. FEA simulations of (a) phase velocities and effective coupling coefficients of AlN Lamb wave resonators for the (b) single IDT electrode configuration, (c) the IDT-floating BE electrode configuration, and (d) the double-IDT electrode configuration when the electrode thickness is equal to 0.02λ.

4.2 Electrode Thicknesses

Generally the electrode thickness of the Lamb wave resonators is around 0.01-0.03. The effect of thicker electrodes is similar to using heavier metals.

Figure 4-6 presents the k^2_{eff} of the LWRs with single-IDT type using the Pt (representing the heavy metal case) and Al (representing the light metal case) as the IDT for a metal thickness range of 0.01-0.05. Thicker electrodes decrease the k^2_{eff} more when AlN is relatively thin(h_{AlN}/λ < 0.2), as shown in Figure 4-6(a), but for light metals the reduction is trivial, as shown in Figure 4-6(b). On the other hand, thicker electrodes using either heavy or light metal enhance the k^2_{eff} more when AlN is thick (h_{AlN}/λ > 0.5). The reason is that for the heavy metal case, when AlN is thin, thicker metal deviates the acoustic wave field more from the piezoelectric layer and reduce the electro-mechanical transduction efficiency, but light metal don't effect the acoustic wave field much. However, for the both case, when the AlN is relatively thick, the thicker metal gives stronger stiffening effect that enhance the k^2_{eff}. However, there is also a limit of the largest k^2_{eff}. For example, when $h_{Pt}/\lambda \approx 0.04$ and $h_{AlN}/\lambda \approx 0.5$, the k^2_{eff} reaches a top value of around 3.4%, as shown in Figure 4-6(a), and when h_{Pt}/λ increased to 0.05 the top value of k^2_{eff} decreased because of the stronger loading effect.

Another consideration for determining the electrode thickness is the static capacitance. Thinner metals generally give slightly large C_0 under the same area, which can potentially enable small devices. Whats more, although electrode resistance is a secondary consideration, too thin metal electrodes would not be preferable to avoid additional circuit elements [28].

Table 4-2. Physical properties of selected metals [2].

	Al	Pt	Mo	W	Units
Bulk resistivity	2.8	10.7	5.7	5.39	(10^{-6} Ω·cm)
Mass density	2700	21400	10200	19250	(kg/m^3)
Longitudinal acoustic wave velocity	~6400	~4200	~6700	~5500	(m/s)
Thermal expansion	18	8.9	5.1	4.3	(10^{-6}/°C)
Crystal structure	Cubic (FCC)	Cubic (FCC)	Cubic (BCC)	Cubic (BCC)	–
Crystalline orientation	(111)	(111)	(110)	(110)	–
Lattice constant	4.0494	3.9231	3.1472	3.16	(Å)
Lattice mismatch to AlN	8.68	12.18	1.12	1.52	(%)

4.3 Other Considerations and Comparison

4.3.1 Other Considerations

For the bottom electrode, the lattice mismatch between the metal and AlN should also be considered to ensure a good quality of AlN. Except for the texture and surface roughness of the underlying electrode metals, the degree of c-axis orientation of AlN thin films is strongly dependent on their crystal structures and lattice mismatch with AlN [85]. Table 4–2 summarizes and compares the physical properties of several common metal materials used for the bottom surface metallization of AlN-based devices. Although Mo and W show less lattice mismatch than Al, W usually tends to have a high level of residual film stress and large surface roughness and Mo would be attacked by XeF_2 during the structure release process of the AlN LWRs. The lattice mismatch issue can be addressed by using an AlN seed layer.

If a metal has large density and high resistivity, it would be difficult to get a balance between suppressing the strong loading effect and getting low impedance.

In addition, low acoustic impedance, especially the “soft” material also has low acoustic *Q* that may deteriorate the *Q* of the resonator.

4.3.2 Comparisons

Aluminum (Al) is the most readily available material and is easily deposited with a standard DC-sputter deposition. But Al cannot stand high temperature. If the device needs low resistance and does not need to stand high temperature, aluminum is a good

choice for the bottom electrode. If there is no requirement on the coupling coefficient, Al can also be used as IDT material.

Titanium (Ti) has hexagonal (0001) structure and is most suitable for AlN to grow on it. However, Ti has only small acoustic impedance and talked before and it shows a high bulk resistivity up to 55 $\mu\Omega \cdot$ cm which is not preferred for low-impedance acoustic wave devices.

Copper (Cu) has even better conductivity than Al, but the deposition process for it is complex and the cost is high. It has small acoustic impedance as discussed before, and it also has low acoustic *Q*, which makes is a unfavorable electrode material for micro-acoustic devices. Cu can also potentially contaminate the CMOS process.

Molybdenum (Mo) has been widely used in commercial manufacturing of BAW resonators since it is a very acoustically stiff material and has moderately low resistance. Mo can easily be deposited by either DC or AC sputtering. It has thermal expansion coefficient similar to AlN which minimizes impact from thermal mismatch and residual stress from Mo/AlN interface. Mo can also enable highly oriented AlN grown on it because of the small mismatch between the surfaces of the two crystalline structures. As a result, Mo is very good material used for IDT electrodes, and can also be used as bottom electrode. The only concern is that Mo would be attacked by XeF_2 during the structure release process of the AlN LWRs, so additional protection process is needed which will complicate the fabrication process.

Tungsten (W) has very high acoustic impedance that can enable high k^2_{eff} and similar thermal expansion coefficient to AlN that minimize the thermal mismatch. The high acoustic impedance and similar thermal expansion coefficient to AlN makes W an excellent candidate as part of the acoustic mirror in SMRs. Unfortunately, W is both dense and has high resistance, which makes it difficult to get a balance between the strong loading effect and low impedance. It also has poor surface roughness, making an additional CMP process is required to ensure good crystallized AlN grown on it. So W is not good for the bottom electrode but can be used as IDTs if low-impedance is not emphasized and the AlN cannot be too thin as discussed before to get large k^2_{eff}.

Platinum (Pt) is a face-centered cubic (FCC) structure and can be easily deposited. It has very high acoustic impedance that can enable high k^2_{eff} when AlN is relatively thick as discussed before. It can also stand high temperature. However, similar with tungsten that has both high density and high resistance, Pt electrodes are required to be thin to avoid the strong loading effect but becomes high resistive, which makes is less successful in commercial BAW industry. For Lamb wave resonators, Pt are very suitable for IDT electrodes to enhance the high k^2_{eff} and stand high temperature for harsh environment applications. It should be noticed that Pt electrodes can be shaped by lift-off but very difficult by chemical etching.

Gold (Au) is a typical “soft” material and has large acoustic loss. It is also expensive and a contaminant of the CMOS process, even though it is very conductive. So similar to copper, it is usually not considered for electrodes in micro-acoustic devices [28].

Potential alternatives for electrode materials are like the iridium (Ir) [87] and ruthenium (Ru) [84], [86]. Especially Ru has been widely studied nowadays. It has hexagonal structure and can enable high Q and large k^2_{eff} at the same time, which are very attractive properties. In practice, Ru tends to oxidize fairly quickly especially when it has poor crystal orientation. Once heavily oxidized, it is critical to remove the oxide before depositing AlN. Ru is very expensive and is seldom used in high-volume application now.

4.4 Conclusions

The selection of electrode materials and thicknesses has large impact on the performance of micro-acoustic resonators. Although the effect of electrode materials and thicknesses has been intensively studied for the SAW resonators and FBARs, the dispersive characteristic of the Lamb wave makes it complicated and different from SAW resonators or FBARs, and there is yet no systematic study for the Lamb wave resonators. For the first time, this study adopts the finite element analysis to investigate the influence of electrodes on the Lamb wave resonators using the S_0 mode. Four types of electrode configurations for the AlN Lamb wave resonators are considered here and compared for the pure AlN structure. For each electrode configuration, the effect of metal electrodes on the phase velocities and effective coupling coefficients are calculated and analyzed. The phase velocity is directly related to the density and equivalent phase velocity in the metal, while the coupling coefficients depend on the density and acoustic impedance of the metal. Large-Z material is preferred for the IDT and light material is favored for the bottom electrode to optimize the effective coupling coefficient. The impact of the electrode thickness is also analyzed: thicker metal for the IDT loads the k^2_{eff} more when AlN is thin and enhance k^2_{eff} more when AlN is relatively thick. These results reveal the potential of high-f_s and large–k^2_{eff} AlN Lamb wave resonators by careful selection of electrodes for frequency selection applications.

Chapter 5

Q Enhancement of AlN Lamb Wave Resonators Using Butterfly-shaped Plates

The small-in-size and CMOS-compatible MEMS resonators are likely to be the driving core of a new generation of electronic devices such as RF filters, sensors, and timing references [4], [45]. Thanks to the high frequencies, low R_m, and capability of multiple frequencies operation on a single chip, the AlN Lamb wave resonators utilizing the S_0 mode have attracted attention among various micromechanical resonator technologies. However, the AlN Lamb wave resonator usually shows a Q below 2,000 due to complicated energy dissipation mechanisms, so an improvement in its Q is highly desirable to further enable low-loss filters, high-sensitivity sensors, and low-phase-noise oscillators.

5.1 Loss Mechanisms

Unlike the capacitive resonators that tend to show a very high Q but a huge R_m, piezoelectric resonators usually exhibit a large coupling which leads a small R_m, but unfortunately they show a medium Q [45], [88]. Different loss mechanisms [89] in piezoelectric MEMS resonators have been investigated recently, and the interfacial loss, causing from the stress jump at the material interface [90]–[92] as well as the anchor loss, representing the acoustic energy leakage via the support tethers into the substrates [92]–[100], are now suspected of the primary energy dissipation mechanisms. Fortunately, the electrode-to-piezoelectric stress can be minimized with the optimized metal deposition conditions [72] or separating the piezoelectric layer from its metal electrode [91] to reduce the interfacial loss. By suppressing the acoustic wave leakage through the tethers, the Q of the piezoelectric resonators can be improved [94]–[100].

Generally, the anchor loss of the MEMS resonators can be minimized by many strategies, such as positioning the tethers at nodal locations of the resonance mode,

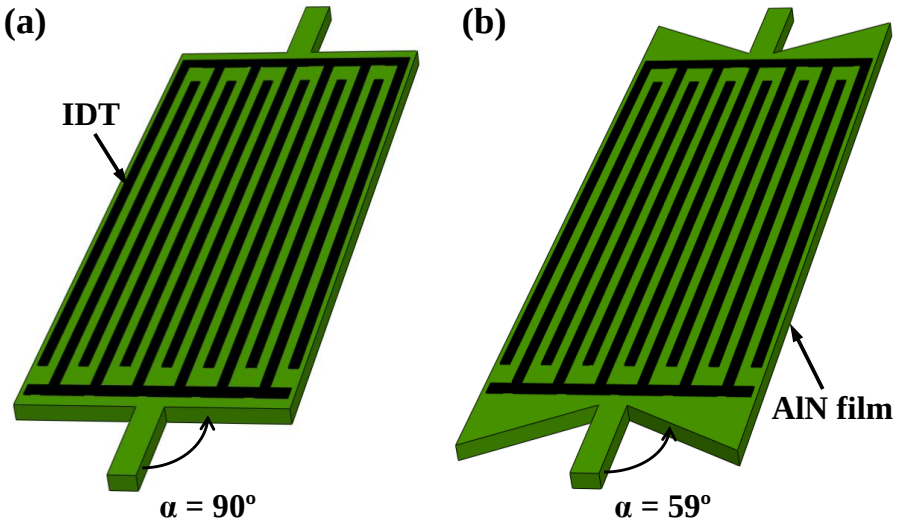

Figure 5-1. Illustration of (a) a conventional AlN Lamb wave resonator employing a rectangular plate with tether-to-plate angle α = 90º, and (b) an AlN Lamb wave resonator with a butterfly-shaped plate with α = 59º

narrowing the width of the support tethers, using different materials for the support and vibrating body to form an acoustic impedance mismatch, and designing the tether length with an odd multiple of a quarter-wavelength ($\lambda/4$) [93]. Another effective way of reducing the anchor loss is to reflect the acoustic waves leaky via the tethers back to the resonant structure [95], [99], [100] or to concentrate the acoustic wave displacement far from the supporting area [96]. Recently, the suspended biconvex edges were demonstrated to efficiently concentrate the Lamb wave distributions in the resonance plate and then boost the *Q*. However, some unwanted spurious vibration modes were also introduced due to the curved reflecting edges [96].

To effectively reduce the anchor loss without introducing unwanted spurious modes, for the first time, a novel AlN Lamb wave resonator utilizing a butterfly-shaped plate is investigated to enhance the anchor *Q* in this work. Fig. 1(a) illustrates a conventional AlN Lamb wave resonator based on a rectangular thin plate consisting of one interdigital transducer (IDT) and two suspended free edges. As shown in Fig. 1(b), another AlN α = 90º α = 59º.a rectangular plate with tether-to-plate angle α = 90º, and (b) an AlN Lamb wave resonator with a butterfly-shaped plate with α = 59º. Lamb wave resonator composed of the same IDT electrode configuration and free-edge reflector, but the butterfly-shaped plates with a tether-to-plate angle α = 59º is employed as the vibrating structure.

5.2 *Q* Enhancement by Using the Butterfly-Shaped Plate

5.2.1 Resonator Design and Finite Element Analysis

As is well known, the mechanical *Q* describes how under-damped a resonator is and can be generally expressed as:

$$Q = 2\pi \times \frac{E_{\text{stored}}}{E_{\text{dissipated}}}, \tag{5.1}$$

where E_{stored} is the vibration energy stored in the resonator and $E_{\text{dissipated}}$ denotes the energy dissipated per cycle of vibration, respectively. It is clear that to obtain a higher *Q*, it requires more energy stored in the resonator and less energy dissipation, indicating that the magnitude of *Q* ultimately depends on the energy loss in resonators. The most relevant loss mechanisms in piezoelectric resonators are the anchor loss, interface loss, thermoelastic damping (TED), material damping, and other unknown losses [89]. Then, the total *Q* can be estimated by adding the impact of each specific energy loss mechanism:

$$\frac{1}{Q_{\text{total}}} = \frac{1}{Q_{\text{anchor}}} + \frac{1}{Q_{\text{interface}}} + \frac{1}{Q_{\text{TED}}} + \frac{1}{Q_{\text{material}}} + \frac{1}{Q_{\text{unknown}}}. \tag{5.2}$$

The interface loss, $Q_{\text{interface}}$, is caused by the plane stress jump at the material interface and can be minimized by controlling the interfacial stresses during the deposition process. The thermoelastic damping, Q_{TED}, means the energy dissipation during vibration which produces a strain gradient, which leads to a temperature gradient, yielding the heat flow as well as the energy loss. The material damping, Q_{material}, is related to the crystal defects in the material, surface roughness, or grain size so it is difficult to estimate the Q_{material}. In this work, we simply assume that the anchor loss, Q_{anchor}, is the main energy dissipation source in the resonator so we simplify the Q_{total} is contributed by the Q_{anchor}

Table 5-1. Geometric dimensions of the AlN Lamb wave resonators.

	Conventional	**Butterfly-shaped**
IDT finger electrode	13	13
IDT aperture	180 μm	180 μm
IDT electrode width	3 μm	3 μm
IDT electrode thickness	200 nm	200 nm
Tether-to-plate angle	90°	59°
Tether length	33 μm	33 μm
Tether width	8 μm	8 μm
AlN plate length	210 μm	252 μm
AlN plate width	78 μm	78 μm
AlN plate thickness	4.0 μm	4.0 μm

and other losses, Q_{other}, as following:

$$\frac{1}{Q_{total}} = \frac{1}{Q_{anchor}} + \frac{1}{Q_{other}}. \tag{5.3}$$

In this work, we propose a novel AlN plate geometry to reduce the tether vibration caused by the resonant structure to increase the Q_{anchor}. In order to study the effect of the plate shape on Q, the Lamb wave resonators on AlN plates utilizing a rectangular plate and a butterfly-shaped plate are designed and compared as summarized and listed in Table 5-1.

Recently, a new finite element analysis (FEA) simulation approach which is based on the perfectly matched layer (PML) technique is introduced to evaluate Q_{anchor} in MEMS resonators [99]–[101]. The PML can rapidly attenuate the acoustic waves leaky via the support tethers and also perfectly match the rest of the domain so there is no spurious reflection caused by the substrate/PML interface as shown in Fig. 5-2. Herein, we employ the PML-based FEA approach and the commercially available FEA software, COMSOL Multiphysics®, to analyze the Q_{anchor} of two resonators using different plate geometries. The Q_{anchor} can be obtained by using the equation [88],[98]–[101]:

$$Q_{anchor} = \frac{\mathrm{Re}(\omega)}{2\,\mathrm{Im}(\omega)}, \tag{5.4}$$

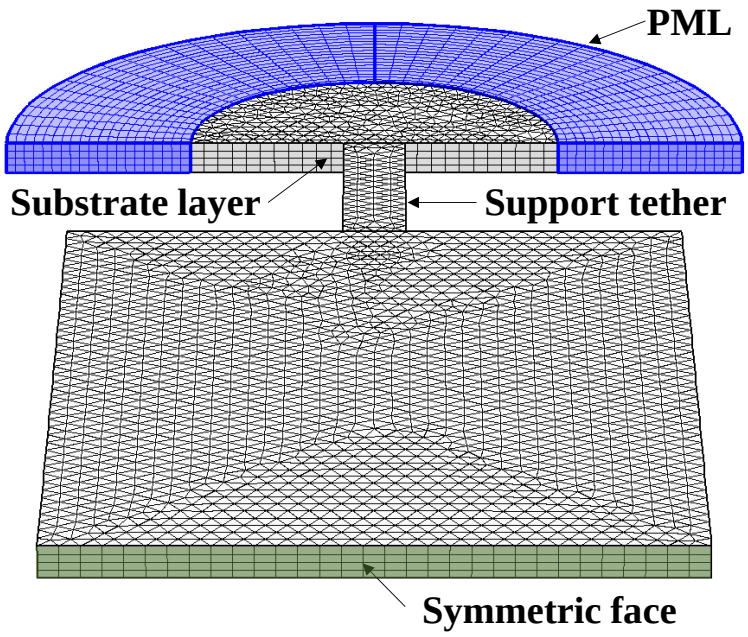

Figure 5-2. Illustrations of half an AlN plate with a simple beam tether attaching to a substrate layer covered by PMLs and the mesh adopted in FEA.

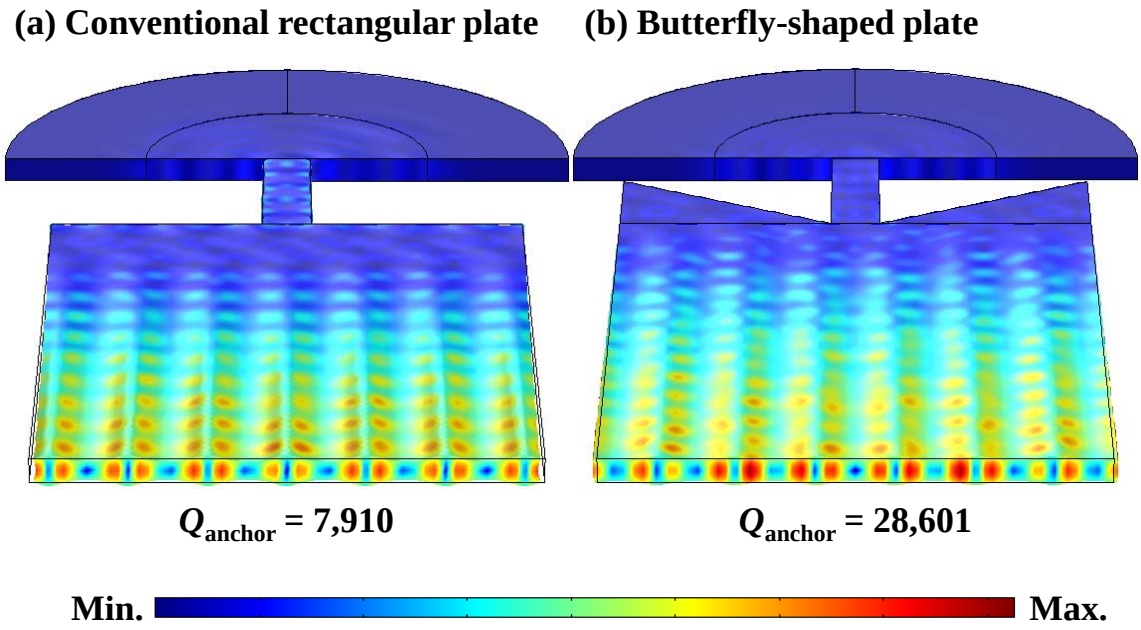

Figure.5-3. Resonance mode shapes (displacement profile) of (a) a conventional rectangular AlN plate with tether-to-plate angle α = 90º and (b) a butterfly-shaped AlN plate with α = 59º.

where ω is the eigen-frequency of the desired mode solved in the FEA model.

Fig. 2 illustrates the FEA model of half an AlN plate with one simple beam tether attaching to the semi-cylinder substrate plate which is covered by the PML to assume the substrate is a semi-infinite plate. The radius of the substrate plate is set as 2λ while the radius of the PML equals 4λ (i.e., the PML thickness is equal to 2λ). The mesh adopted in the FEA model is also shown in Figure 4-2. A symmetric boundary condition is applied to the center face of the AlN plate to ensure the eigen modes are solved for a whole plate.

Figure 4-3 (a) presents the mode shape (displacement profiles) of the S_0 Lamb wave at resonance in the conventional rectangular AlN plate. There is obvious displacement in the support tether, indicating a part of mechanical energy would lose via the tether vibration. The predicated Q_{anchor} is equal to 7,910 based on the PML-based FEA model. In addition, Figure 4-3 (b) depicts the mode shape of the same S_0 mode at resonance in the butterfly-shaped AlN plate and the displacement in the tether is apparently less than that in the conventional rectangular plate. The simulated Q_{anchor} of the S_0 mode in the butterfly-shaped AlN plate is increased to 28,601. Interestingly, the butterfly-shape plate can effectively reduce the displacement occurring in the tethers and further offer a 3.62× improvement in the Q_{anchor}.

5.2.2 Experimental Results and Discussions

All the resonators reported in this work were fabricated on the same wafer and placed in the vicinity. The Lamb wave resonators were tested in air and S_{11} parameters were

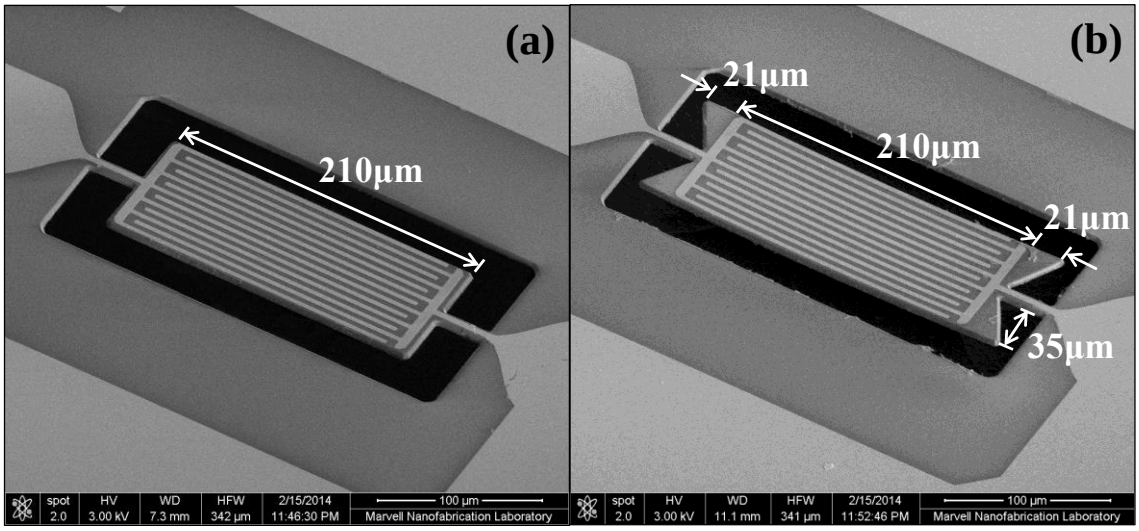

Figure 5-4. SEM images of the fabricated AlN Lamb wave resonators utilizing the (a) rectangular plate and (b) butterfly-shaped plate with α = 59º.

extracted using an Agilent E5071B network analyzer. The measured *Q* was extracted from the admittance plot by dividing the resonance frequency (f_s) by the 3 dB bandwidth.

The *Q*'s measured from Lamb wave resonators using the butterfly-shaped plates are consistently higher than those using the rectangular plates. Figure 5-5 compares one set of the measured frequency responses of the resonators with 13 finger electrodes on the 4-

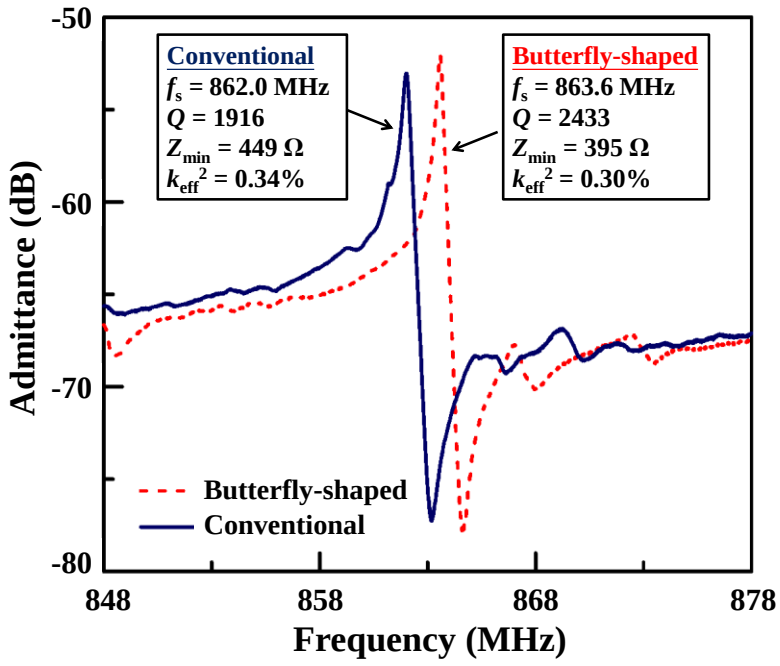

Figure 5-5. Measured admittance spectra of the conventional and butterfly-shaped AlN Lamb wave resonators. The inset depicts the MBVD model.

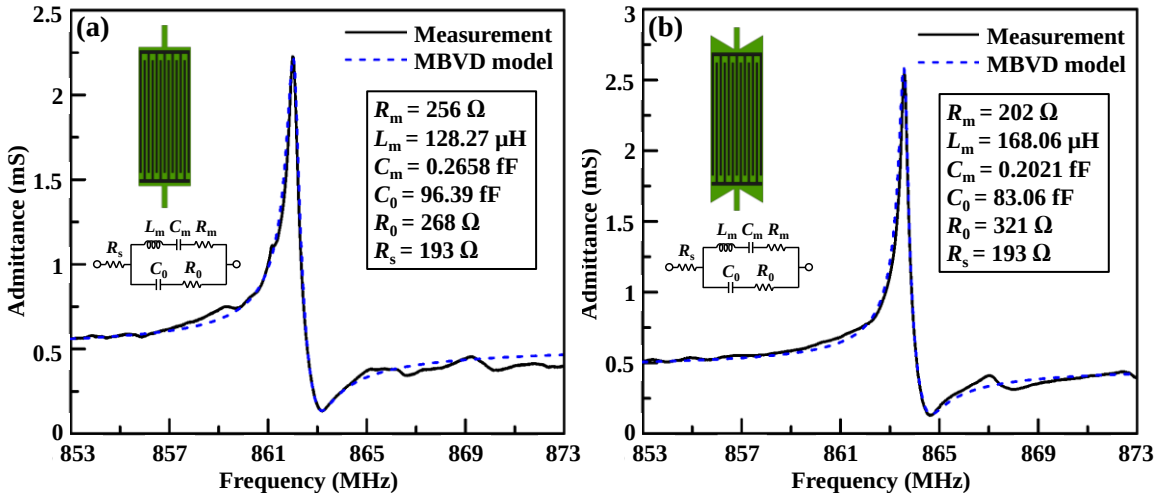

Figure 5-6. Close-up view of the frequency spectra of the resonators with the (a) conventional, (b) butterfly-shaped plates and their six equivalent circuit parameters of the MBVD model.

μm-thick rectangular and butterfly-shaped AlN plates. The 863.6 MHz resonator on the butterfly-shaped plate with α = 59º yields a Q of 2,433, representing a 1.27× enhancement over the 862.0 MHz resonator on the rectangular plate. An effective coupling (k_{eff}^2) of the butterfly-shaped resonator is 0.3%, slightly lower than 0.34% observed in the rectangular one, but the k_{eff}^2 is still sufficient for oscillators, sensors and narrowband filters. Moreover, the butterfly-shaped AlN plate neither introduces any other spurious mode nor shifts the resonance frequency significantly in comparison to the Lamb wave resonator with biconvex free edges [88].

Figure 5-6 shows the fitted curves comparing to the measured spectra of the AlN Lamb wave resonators on the rectangular and butterfly-shaped plates. The corresponding MBVD parameters are also listed in Figure 5-6. The extracted R_m of the conventional and butterfly-shaped AlN Lamb wave resonators are 256 Ω and 202 Ω, respectively. The resonator based on the butterfly-shaped plate exhibits a smaller R_m than the conventional

Table 5-2. Performance of the AlN Lamb wave resonators.

	Conventional	**Butterfly-shaped**
Motional resistance, R_m	256 Ω	202 Ω
Motional inductance, L_m	128.27 μH	168.06 μH
Motional capacitance, C_m	0.2658 fF	0.2021 fF
Static capacitance, C_0	96.39 fF	83.06 fF
Static resistance, R_0	268 Ω	321 Ω
Series resistance, R_s	193 Ω	193 Ω
Loaded Q	1,916	2,433
Unloaded Q	3,360	4,758
Simulated Q_{anchor}	7,910	28,601
Extracted Q_{other}	5,841	5,707

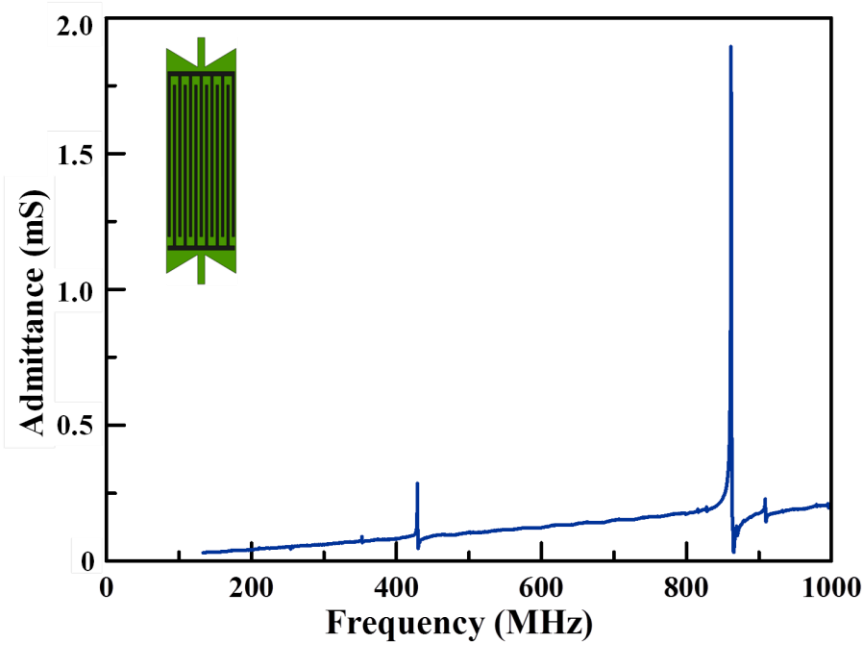

Figure 5-7. Measured admittance spectrum for the butterfly-shaped Lamb wave resonator in a wide spectrum.

resonator thanks to the higher Q. It should be noted that the series resistance (R_s) in the resonators is huge, implying imperfect metal contact condition and poor metal deposition in the resonators, resulting in a considerable loading effect on Q's. The unloaded Q can be extracted by the following expression

$$Q_{s,unload} = (\frac{R_m + R_s}{R_m})Q_s \,. \tag{5.5}$$

The unloaded Q of the butterfly-shaped resonator is 4,758, showing a 1.42× increase in the unloaded Q compared to the conventional Lamb wave resonator.

Table 5-2 summarizes the performance of the AlN Lamb wave resonators on the rectangular and butterfly-shaped plates, including the six extracted MBVD [72] parameters as well as the loaded and unloaded Q. As listed in Table 5-2, based on the loaded Q and simulated Q_{anchor}, the extracted Q_{other} are around 5,800 for both resonators, implying that either the conventional resonator or the butterfly-shaped resonator are suffered from the same level of the other loss mechanisms. As a result, although the Q_{anchor} of the Lamb wave resonator has been boosted to 28,601 using the butterfly-shaped plate, the measured Q is still limited by the other loss mechanisms. Among all the loss mechanisms, the interfacial damping is suspected of another main loss mechanism in the AlN Lamb wave resonator since the Pt/Cr metal contact in the resonators is not perfect as discussed above[72],[90]–[92].

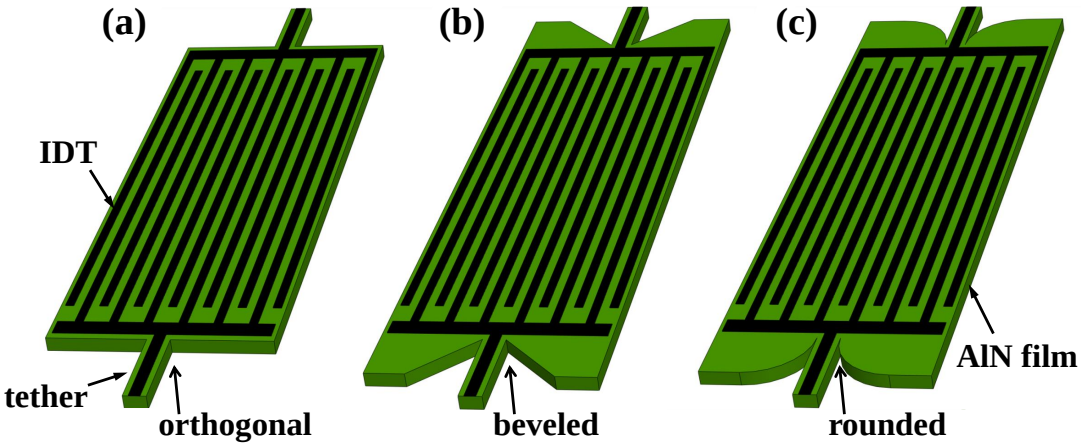

Figure 5-8. Illustrations of (a) a conventional AlN Lamb wave resonator (LWR), (b) a butterfly-shaped AlN LWR with a beveled tether-to-plate transition angle of 45º, and (c) a butterfly-shaped AlN LWR with a rounded tether-to-plate transition.

Most importantly, as shown in the measured frequency response in the wide spectrum in Figure 5-7, the butterfly-shaped plate didn't introduce spurious modes on a wide spectrum, compared to other *Q* increase techniques.

By using the butterfly-shape AlN plate, the displacement in the tethers is efficiently suppressed and the energy loss via the tethers is then reduced. The butterfly-shaped resonator enables an unloaded *Q* up to 4,758, showing a 1.42× enhancement over the conventional resonator. In addition, the experimental results are in good agreement with the simulated predictions by the 3D PML-based FEA model, confirming that the butterfly-shaped AlN thin plate can efficiently eliminate the anchor dissipation. The *Q* of the Lamb wave resonators is expected to be significantly boosted using the butterfly-shaped plate if the interfacial loss can be minimized by well-controlled interface stresses under optimized metal deposition conditions.

5.3 Butterfly-Shaped Resonator Using Rounded Tether-to-Plate Transition

5.3.1 Resonator Design and Modeling

Figure 5-8(a) illustrates a conventional AlN LWR employing the orthogonal tether-to-plate transition and with one IDT and two straight suspended free edges. As shown in Figure 5-8(b) and (c), butterfly-shaped AlN LWRs are composed of the same IDT electrode configuration and straight free-edge reflectors, but with a 45º beveled tether-to-plate transition and a rounded tether-to-plate transition, respectively [97].

Figure 5-9(a) indicates the position of the tether-to-plate plane that we investigate in the FEA model, and Figure 5-9(b) illustrates the half AlN plate with one simple beam

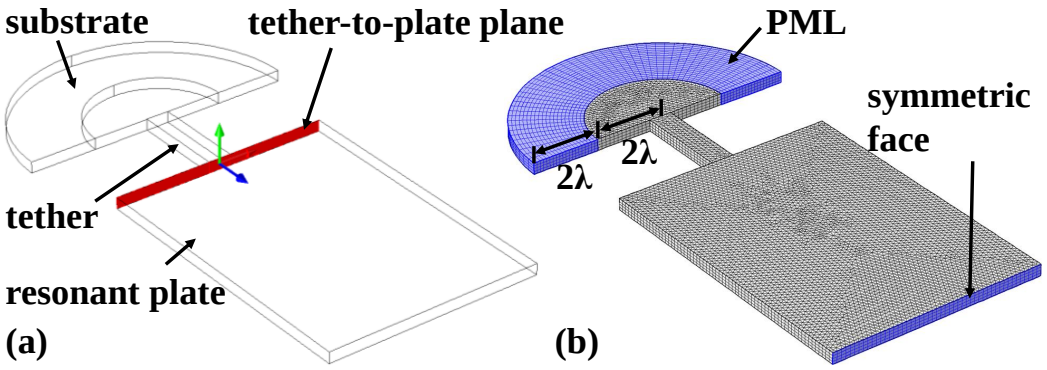

Figure 5-9. Illustrations of (a) the position of the tether-to-plate plane and (b) the half AlN plate with a simple beam tether attaching to a substrate layer covered by PMLs and the mesh adopted in FEA.

Table 5-3. Geometric dimensions of the AlN Lamb wave resonators with different tether-to-plate transitions.

	Orthogonal	Beveled	Rounded
IDT finger electrodes	13	13	13
IDT aperture	180 μm	180 μm	180 μm
IDT electrode width	3 μm	3 μm	3 μm
IDT electrode thickness	200 nm	200 nm	200 nm
Tether-to-plate angle	90°	45°	–
Tether length	33 μm	33 μm	33 μm
Tether width	8 μm	8 μm	8 μm
AlN plate length	210 μm	252 μm	252 μm
AlN plate width	78 μm	78 μm	78 μm
AlN plate thickness	4.0 μm	4.0 μm	4.0 μm

tether attaching to the semi-cylinder substrate which is covered by the PML to model the substrate as the semi-infinite plates. The radius of the substrate plate is set as 2λ while the PML thickness is equal to 2λ. The mesh adopted in the FEA model is also shown in Figure 5-9(b). A symmetric boundary condition is applied to the center face in the FEA model.

The anchor loss can be directly evaluated by the vibration strength in the tether. For the conventional LWR with the orthogonal tether-to-plate transition, there are relatively strong vibrations delivered to the tether from the resonant plate, so that the mechanical energy is dissipated through the tethers. In this work, we propose a novel AlN plate geometry to reduce the tether vibration caused by the resonance body. In order to study the effect of the plate shape on the tether vibration, the LWRs on AlN plates utilizing a rectangular plate, a beveled butterfly-shaped plate and a rounded butterfly-shaped plate are designed and compared as summarized and listed in Table 5-3.

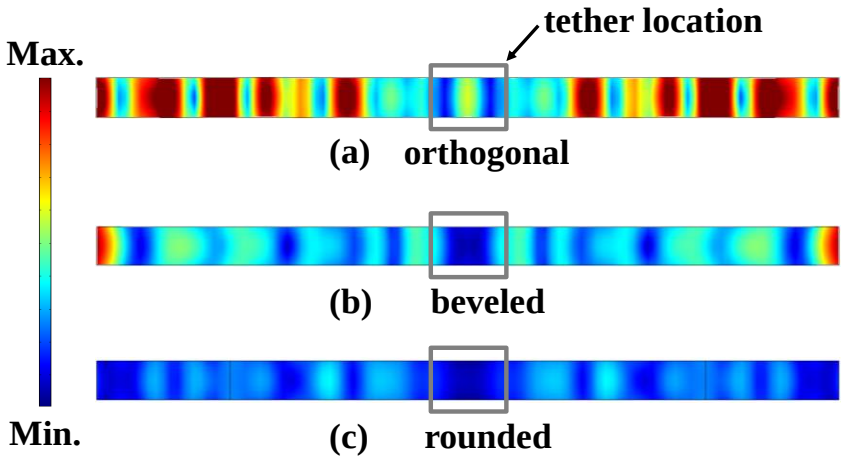

Figure 5-10. Displacement profiles at the S_0 mode resonance of the tether-to-plate plane for the AlN LWRs with the (a) orthogonal (b) beveled, and (c) rounded tether-to-plate transitions.

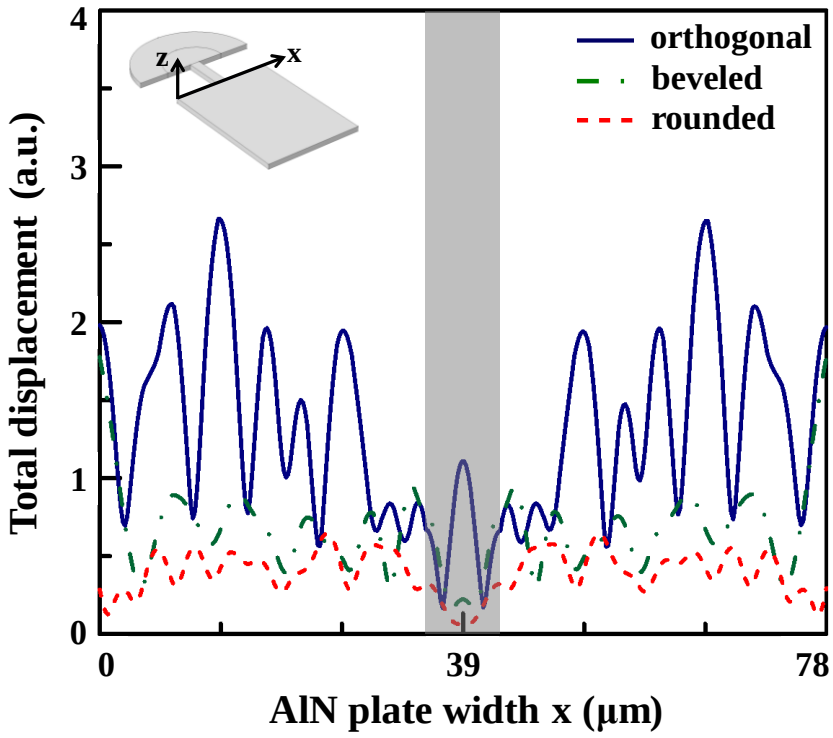

Figure 5-11. Simulated displacement profiles on the top edge of the tether-to-plate plane at the S_0 mode resonance for the three designs of AlN LWRs.

As is shown in Figure 5-10, the FEA model simulates the displacement profile on the tether-to-plate plane for the different resonator designs. The vibration in the center of the plane directly goes to the substrate through the tether. The displacement profiles indicate that the butterfly-shaped design can efficiently reduce the vibration in the center by pushing the displacement to the sides, so that the wave dissipated through the tether can be reduced. Also, the rounded tether-to-plate transition shows a more efficient

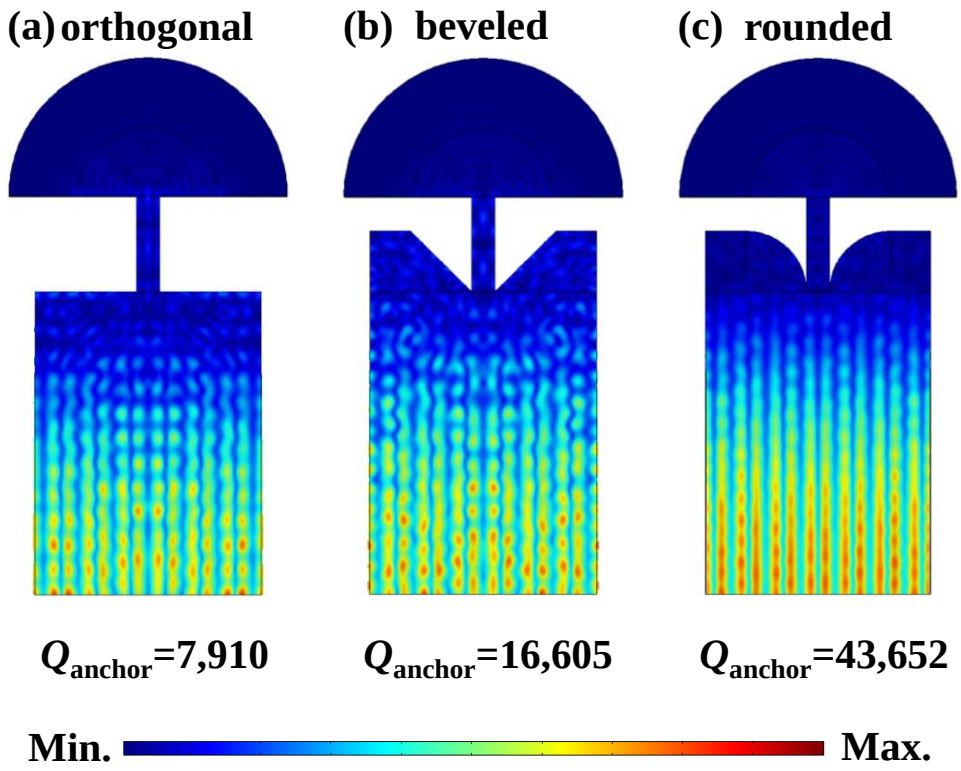

Figure 5-12. Resonance mode shapes of (a) conventional rectangular AlN LWRs utilizing an orthogonal tether-to-plate transition, and butterfly-shaped AlN LWRs with (b) a 45º beveled tether-to-plate transition, and (c) a rounded tether-to-plate transition.

suppression on the center vibration, due to a smaller tether-to-plate angle (0˚) than the beveled transition (45˚). To be more specifically, Figure 5-11 gives the displacement level on top of the tether-to-plate plane. Again, it can be observed that the butterfly-shaped design push the displacement level to the sides, and the rounded transition has a stronger pushing effect especially at the plane center, where the tether locates.

Figure 5-12 presents the mode shape of the S_0 Lamb wave at resonance in the AlN plates employing different tether-to-plate transition types. In Figure 5-12(a), there is obvious wave leaky through the support tether of the orthogonal transition type, indicating a part of mechanical energy loss via the tether. The predicated Q_{anchor} is equal to 7,910 using the PML-based FEA approach. In Figure 5-12(b) and (c), the displacement field in the supporting area is weaker than that in the conventional rectangular plate. In addition, the rejection of the leaky wave is most effective for the rounded transition type and the vibration in the tether is the minimum. The simulated Q_{anchor} of the S_0 mode in the butterfly-shaped AlN plate using the beveled transition is increased to 16,605, and the rounded transition upwards to 43,652. Interestingly, the butterfly shape employing the rounded tether-to-plate transition can effectively reduce the displacement occurring in the tether and further shows a 5.52× improvement in anchor *Q*.

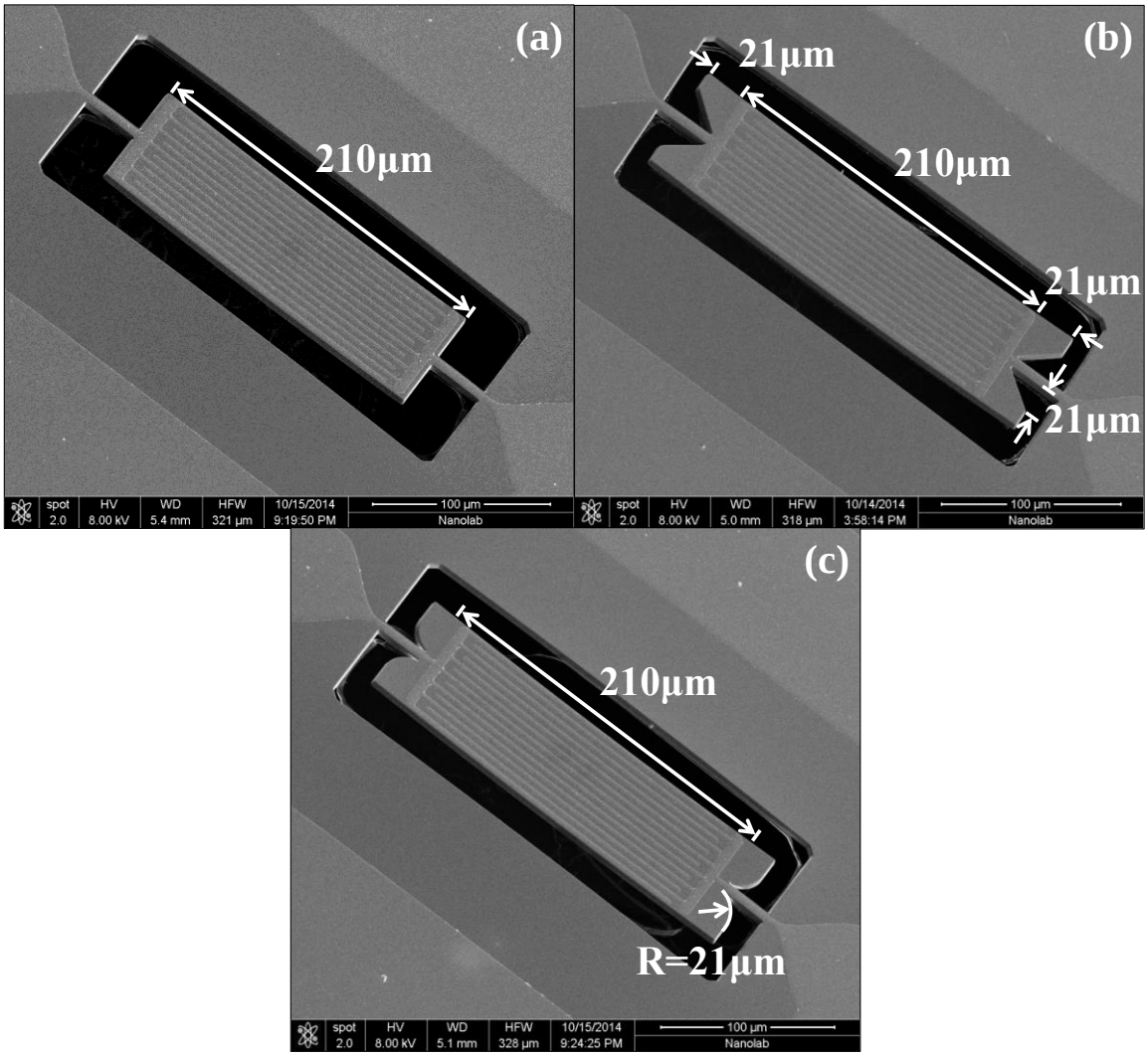

Figure 5-13. SEM images of the fabricated (a) conventional rectangular AlN LWRs utilizing an orthogonal tether-to-plate transition, and butterfly-shaped AlN LWRs with (b) a 45º beveled tether-to-plate transition, and (c) a rounded tether-to-plate transition.

5.3.2 Experimental Results and Discussions

Figure 5-13 shows the SEM images of the rectangular and butterfly-shaped resonators on 4.0-µm-thick AlN membranes. To diminish the fabrication error, all the resonators were fabricated on the same wafer and placed in the vicinity. LWRs were all tested in air and S_{11} parameters were extracted using an Agilent E5071B network analyzer. The measured Q was extracted from the admittance plot by dividing the resonance frequency (f_s) by employing the 3 dB bandwidth.

The Q's measured from the butterfly-shaped Lamb wave resonators with small tether-to-plate angle are consistently higher than conventional rectangular resonators using

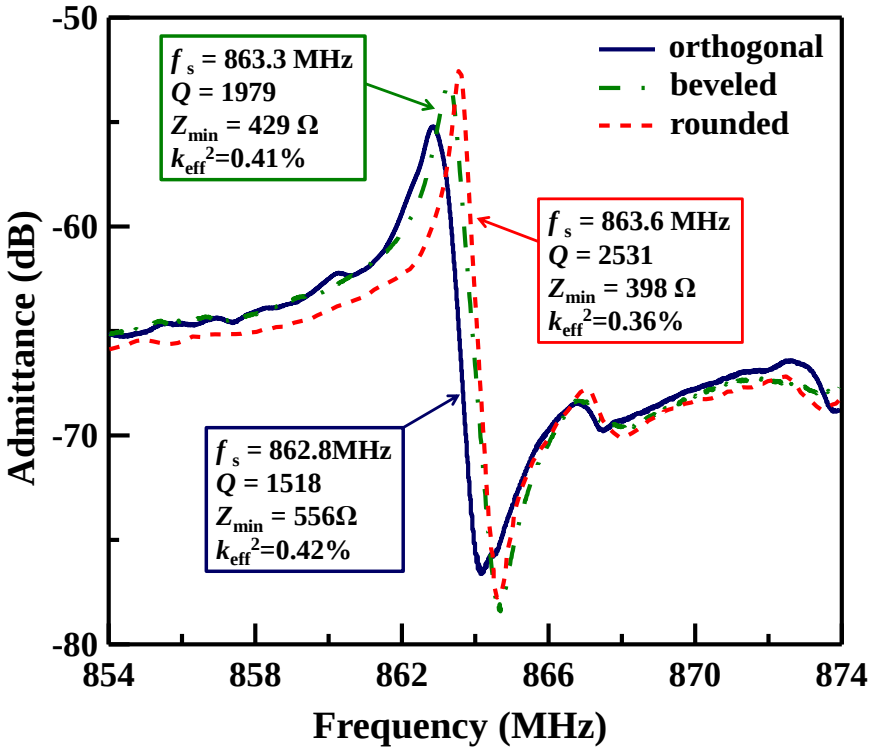

Figure 5-14. Measured admittance spectra of the AlN LWRs using the orthogonal, beveled, and rounded tether-to-plate transitions.

orthogonal tether-to-plate transition. Figure 5-14 presents one set of the one-port admittance response spectra for the LWRs using orthogonal, 45˚ beveled and rounded tether-to-plate transitions. The reduction of the tether-to-plate angle successfully suppresses the vibration in the supporting area, offering reduction of the anchor loss and boost of the *Q*.

The 863.3-MHz resonator on the butterfly-shaped plate with 45˚ beveled tether-to-plate transition yields a *Q* of 1,979, upwards 30% over a conventional rectangular resonator using the orthogonal transition, and the rounded tether-to-plate transition enables a *Q* over 2,500, representing a 67% improvement. The effective coupling (k_{eff}^2) of the resonators on the butterfly-shaped plates are slightly lower than observed in the conventional AlN LWR, but still sufficient for oscillators and narrowband filters. Moreover, the butterfly-shaped AlN plate neither introduces any other spurious mode nor shifts the resonance frequency fs significantly.

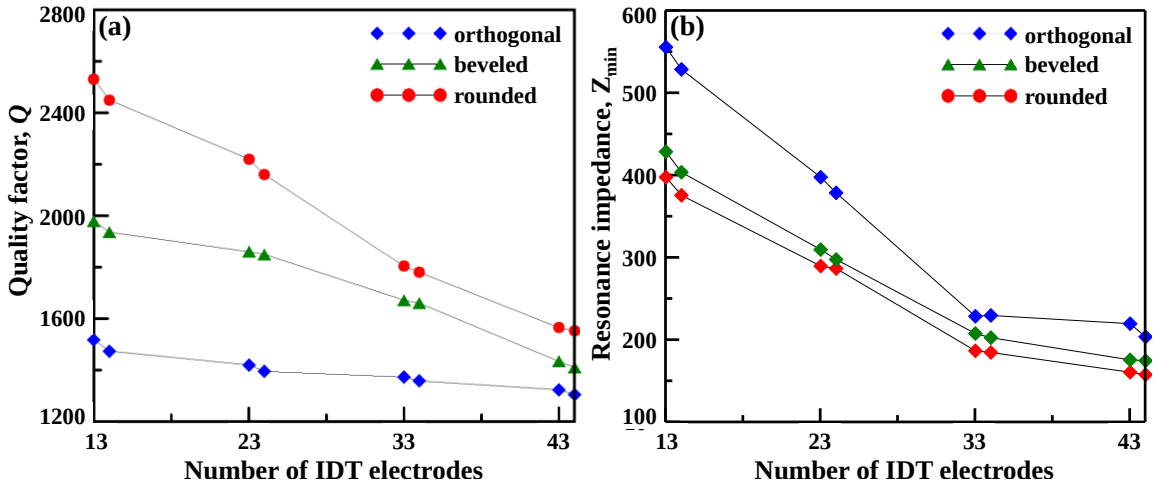

Figure 5-15. Measured (a) quality factors and (b) resonance impedances of the AlN LWRs using the orthogonal, beveled, and rounded tether-to-plate transitions for different number of electrodes (NE).

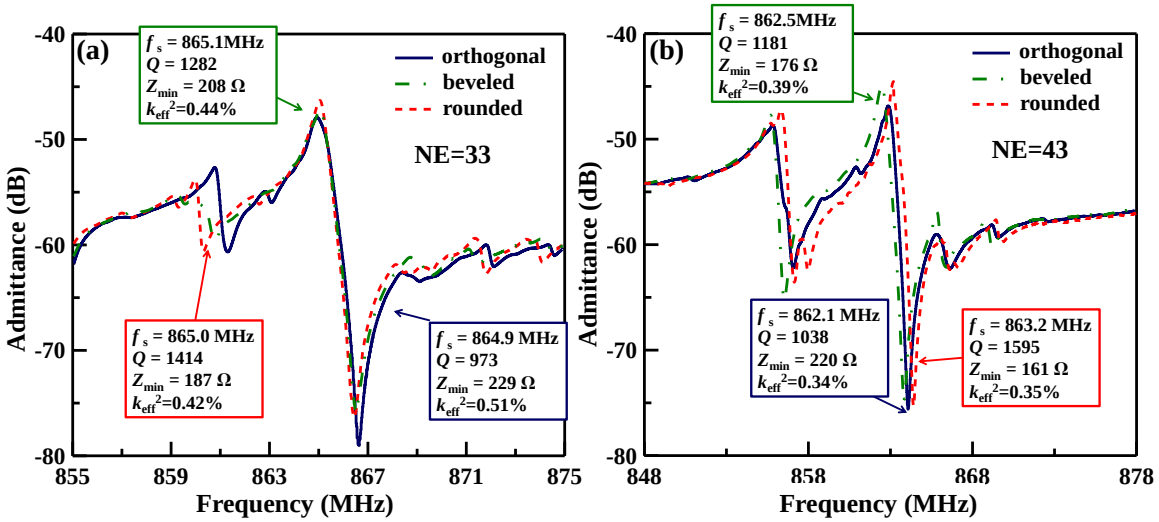

Figure 5-16. Measured admittance spectra of the AlN LWRs using the orthogonal, beveled, and rounded tether-to-plate transitions when (a) NE = 33 and (b) NE = 43.

5.5 Effect of the Number of Electrodes (*NE*)

Figure 5-15 summarizes the measured quality factors and resonance impedances of the AlN Lamb wave resonators using the orthogonal, beveled, and rounded tether-to-plate transitions for different number of electrodes (*NE*). By comparing the *Q*'s and Zmin's with different number of electrodes, it can be observed that the butterfly shape shows constant enhancement on the *Q*, and a constant reduction on Z_{min}, especially the rounded tether-to-plate transition case. When number of electrodes increases, the resonance

impedance is smaller thanks to the smaller resistance of the IDT electrodes (larger area) and better transduction (larger k^2_{eff}). The measured loaded Q becomes smaller as the NE increases. This because the motional impedance of the device R_m decreases much faster than the resistance of the electrodes R_s as the the *NE* increases, resulting in stronger electrical loading effect that suppresses the Q_{loaded}.

Figure 5-16 presents two sets of measured admittance spectra of the AlN LWRs using the orthogonal, beveled, and rounded tether-to-plate transitions when NE = 33 and NE = 43. It can be noted that when number of electrodes becomes too large, the internal reflection will bring spurious modes. When NE = 43, the spurious mode is almost as strong as the main S_0 mode. As a result, we generally use number of electrodes that below 30 for the AlN Lamb wave resonators.

5.6. Conclusions

A new design approach for improving the anchor loss of the Lamb wave resonators is presented. By using the butterfly-shape AlN plate, the displacement in the tethers is efficiently suppressed and the energy loss via the tethers is then reduced. The 59˚ butterfly-shaped resonator enables an unloaded Q up to 4,758, showing a 1.42× enhancement over the conventional resonator. In addition, the experimental results are in good agreement with the simulated predictions by the 3D PML-based FEA model, confirming that the butterfly-shaped AlN thin plate can efficiently eliminate the anchor dissipation. The Q of the Lamb wave resonators is expected to be significantly increased using the butterfly-shaped plate if the interfacial loss can be minimized by well-controlled interface stresses under optimized metal deposition conditions. In addition, the butterfly-shaped plate didn't introduce spurious modes on a wide spectrum, compared to other Q increase techniques

By employing the butterfly-shape AlN plates with rounded tether-to-plate transition which has smaller tether-to-plate angle, the suppression in the anchor loss and enhancement in the Q is even more effective. The simulated displacement profiles show that the butterfly-shaped plate significantly reduces the displacement at the plane center, and the rounded one offers a better efficiency on the displacement suppression at the plane center. The simulated Q_{anchor} using the 3D PML-based FEA model also confirm that the rounded butterfly-shape plates can successfully minimize the anchor loss and boost the Q_{anchor}. The butterfly-shaped resonator with 45˚ beveled tether-to-plate transition yields a Q of 1,979 which upwards 30% over a conventional rectangular resonator; another AlN LWR on the butterfly-shaped plate with rounded tether-to-plate transition yields a Q of 2,531, representing a 67% improvement.

By comparing the performances with different number of electrodes it is found that the butterfly shape shows constant enhancement on Q and a reduction on Z_{min}. When the *NE* becomes larger, the Z_{min} becomes smaller and the loaded Q decreases because the lower R_m causes an obvious electrical loading effect on the Q. When *NE* becomes too

large (> 40), there are strong spurious modes due to internal reflection of the IDTs, which is not preferable.

Chapter 6

Thermally Stable $SiO_2/AlN/SiO_2$ Lamb Wave Resonators

AlN and SiO_2 bilayer structure has been widely utilized in temperature-compensated micromechanical resonators as SiO_2 has unique positive temperature coefficients of elasticity. However, the thermal expansion mismatch would cause large bending deformation and stress distribution in the resonant plate. In this study, a symmetrical $SiO_2/AlN/SiO_2$ sandwiched structure is proposed to reduce the temperature-induced deformation in the asymmetrical AlN/SiO_2 bilayer plate. The thermal compensation at high temperatures for the Lamb wave resonators utilizing the S_0 mode in the $SiO_2/AlN/SiO_2$ sandwiched structure is theoretically investigated herein. While operation temperature rises from room temperature to 600 ˚C, the temperature-induced bending deformation in the symmetrical $SiO_2/AlN/SiO_2$ composite plate is much less than that in the AlN/SiO_2 composite plate conventionally used for temperature compensation. Furthermore, the different material properties of the AlN and SiO2 layers make the displacements of the S_0 mode not purely symmetric with respect to the neutral axis, whereas the symmetrical $SiO_2/AlN/SiO_2$ sandwiched membrane still can enable a pure S_0 mode which shows higher phase velocity and larger electromechanical coupling coefficient than the lowest-order quasi-symmetric (QS_0) mode traveling in the AlN/SiO_2 bilayer membrane. With proper thickness selection of AlN and SiO_2, the S_0 mode in the symmetrical $SiO_2/AlN/SiO_2$ sandwiched membrane can simultaneously offer excellent thermal compensation, high phase velocity, large electromechanical coupling coefficient, and small thermally induced deformation at high temperatures.

6.1 Introduction

In recent years, piezoelectric micro-acoustic devices capable of operating in high temperature environments have attracted great interest in various industries, such as automotive, aerospace, gas and petroleum exploration, and power electronics [102]-[106]. The choice of the constitutive materials is critical for these high-temperature devices. Only few piezoelectric media can withstand high temperature operations above 600°C. For example, quartz is the most widely used piezoelectric material for resonators and sensors, but its applications at high temperatures are limited by the phase transition at

nearly 573°C [102]. Langasite (LGS) can work at high temperatures but suffer from a few drawbacks, such as its rapid increased propagation loss at high temperatures [105]. From this perspective, AlN is one of the most interesting piezoelectric materials for harsh environment applications since AlN retains its piezoelectric properties up to 1150°C and maintains good wave propagation properties at the melting point exceeding 2000°C in a nitrogen atmosphere [103]. Furthermore, the low deposition temperature of the AlN thin film shows the potential for the integration of micro-acoustic devices and CMOS circuits on a single silicon chip.

While the AlN Lamb wave resonator technology constitutes a promising way to enable bandpass filters [106], timing references [46], and passive wireless sensors for harsh environment applications, the capacity for keeping stable resonance frequency (f_s) in high temperature environments is essential [107]-[109]. Unlike quartz-based devices offering a variety of specific temperature compensation cuts for the bulk and surface acoustic waves, AlN exhibits the negative temperature coefficient of elasticity (*TCE*), making it impossible to enable intrinsically temperature-compensated electro-acoustic devices [49]. The temperature compensation of the AlN-based devices is therefore achieved by employing thin film materials with opposite *TCF*. By adding a SiO_2 layer with a *TCF* of 85 ppm/°C [49] onto the piezoelectric AlN layer, a robust temperature compensation approach for the LWRs on an AlN/SiO_2 bilayer plate has been successfully demonstrated at room temperature [73] [110] and high temperatures [107]-[109].

However, these piezoelectric resonators suffer from the frequency instability due to the deformation induced by thermal expansion mismatch between the AlN thin film and SiO_2 layer when operating at high temperatures [109]. Since the thermal expansion coefficients α_{11} of AlN and SiO_2 are 5.27×10–6 $°C^{-1}$ and 0.55×10–6 $°C^{-1}$ [69], respectively, the distinct thermal expansion mismatch of the two materials in the in-plane directions results in large bending deformation which can contribute to spurious modes and frequency instability in the AlN/SiO_2 bilayer structure when the operation temperature arises from room temperature to 600°C. Unfortunately, the low elastic constants and non-piezoelectricity of the SiO_2 layer also causes substantial reductions in the phase velocity (v_p) and electromechanical coupling coefficient (k^2) [68], [73], [108]-[110].

In this work, we propose to integrate the passive SiO_2 layers with the same thickness on both sides of the AlN active layer instead of one single side, forming a symmetrical SiO_2/AlN/SiO_2 sandwiched structure, to lessen the substantial reduction in the v_p and k^2 caused by the SiO_2 layer. As illustrated in Figure 6-1(a), the conventional temperature-compensated LWR consists of one IDT on the AlN surface and two suspended flat edges at the both sides of the AlN/SiO_2 composite plate. Figure 6-1(b) shows the proposed temperature compensated LWR which also consists of the same IDT configuration on the AlN surface but two edge-type reflectors at the both sides of the symmetrical SiO_2/AlN/SiO_2 sandwiched plate. The SiO_2/AlN/SiO_2 structure experiences much less bending deformation induced by the thermal expansion mismatch than the AlN/SiO_2 bilayer plate because of the symmetry in vertical direction as shown in Figure 6-2. Furthermore, the symmetrical composite plate traps more acoustic waves in the AlN active layer [111], [112], so that the piezoelectric energy can be excited more efficiently

to enable higher v_p and larger k^2 for the S_0 Lamb wave mode in the SiO_2/AlN/SiO_2 membrane. By designing a proper thickness ratio of SiO_2 to AlN, the temperature-compensated and high-k^2 LWRs can be achieved at high temperatures.

6.2 Characteristics of the S_0 Lamb wave mode in the SiO_2/AlN/SiO_2 membrane

The physical characteristics that make the lowest-order symmetric (S_0) Lamb wave mode propagation in the AlN plate attractive for practical implementation in piezoelectric resonators are possible simultaneous employment of high phase velocity, weak dispersion, and moderate electromechanical coupling strength [45], [72]. In this study, the S_0 Lamb wave modes propagating in the symmetrical SiO_2/AlN/SiO_2 sandwiched membrane are theoretically investigated.

6.2.1 Displacement symmetry

In general, Lamb waves only have the displacements in the x- and z-directions and the S_0 mode shows the symmetric x-displacement and antisymmetric z-displacement [113], [114]. However, in the conventional AlN/SiO_2 bilayer structure, the different material properties of the AlN and SiO_2 layers make the displacements of the S0 mode not purely symmetric with respect to the neutral axis, which is usually classified as the lowest-order quasi-symmetric (QS_0) mode [115], as shown in Figure 6-3(a). As depicted

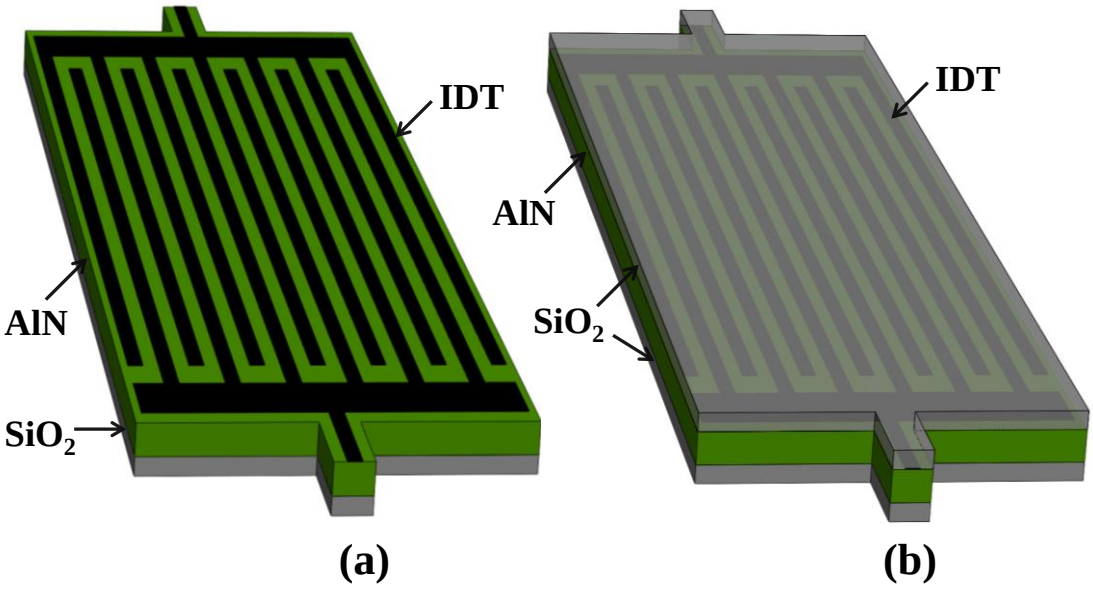

Figure 6-1. Illustrations of (a) a conventional temperature-compensated LWR on an AlN/SiO2 bilayer plate and (b) a temperature-compensated LWR on a symmetrical SiO_2/AlN/SiO_2 composite plate.

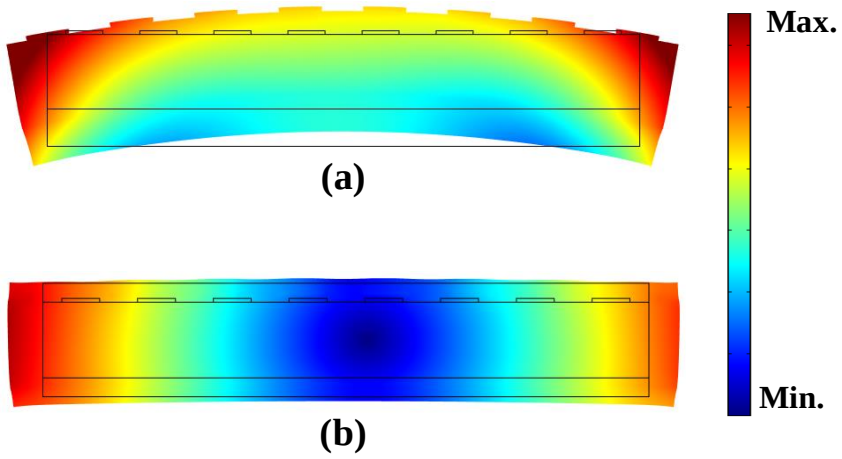

Figure 6-2. Finite element analysis simulation of the deformation of (a) AlN/SiO_2 and (b) $SiO_2/AlN/SiO_2$ layered structures induced by thermal stress when temperature changes from 25°C to 600°C.

in Figure 6-3(b), in the $SiO_2/AlN/SiO_2$ sandwiched structure, the S_0 mode still shows symmetric x-displacement and antisymmetric z-displacement with respect to the neutral axis. The S_0 mode in the symmetrical $SiO_2/AlN/SiO_2$ sandwiched plate traps more acoustic wave fields in the AlN active layer [111] than the QS_0 mode in the AlN/SiO_2 bilayer plate so that the acoustic energy is maximal in the piezoelectric layer to ensure a larger k^2.

6.2.2 Phase velocities

The phase velocity dispersion of the Lamb wave mode propagating in the composite plates can be theoretically computed using Adler's matrix approach [113] or finite element analysis (FEA) method [116]. In the simulation, the Lamb waves propagate in

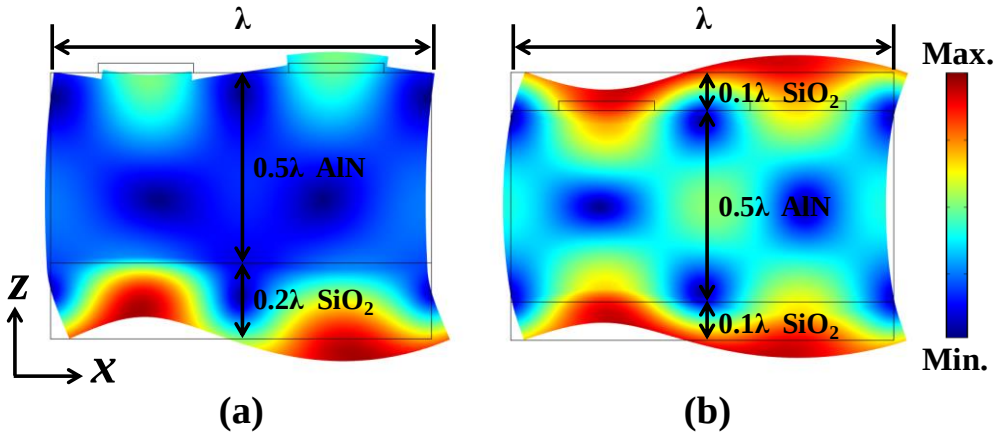

Figure 6-3. The resonance mode shapes of (a) the QS_0 Lamb wave mode in the AlN/SiO_2 bilayer plate and (b) the S_0 Lamb wave mode in the symmetrical $SiO_2/AlN/SiO_2$ sandwiched plate.

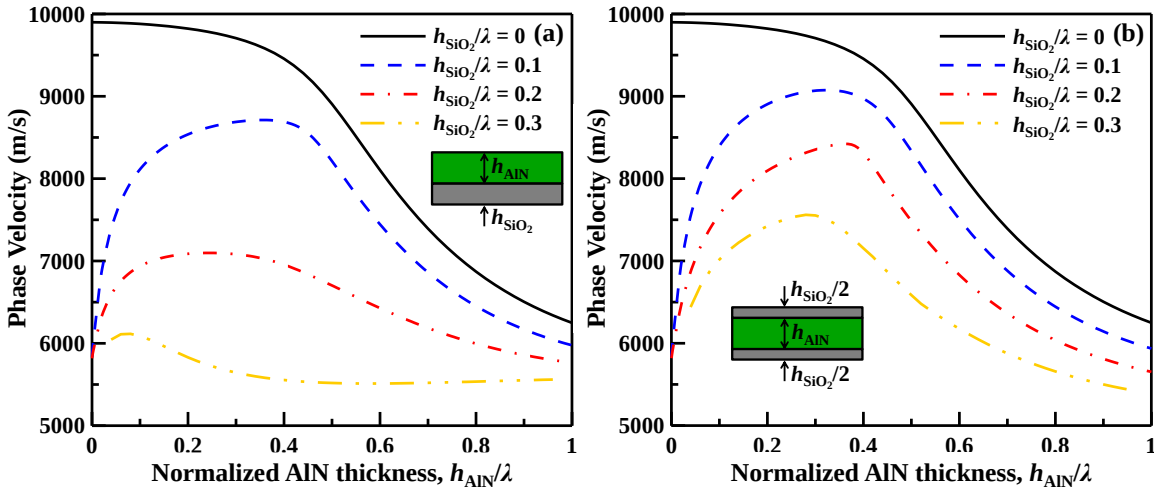

Figure 6-4. Simulated v_p dispersion of (a) the QS_0 mode in the AlN/SiO_2 bilayer membrane and (b) the S_0 mode in the symmetrical SiO_2/AlN/SiO_2 composite membrane.

the plane normal to the c-axis of AlN and the material constants of the AlN and SiO_2 thin film employed in the calculation are obtained from the literature [69] and listed in Table 3-2. The electrical effect of the IDTs and bottom electrodes are ignored because the phase velocity is insensitive to the electrical condition [73].

The SiO_2 layer loads the AlN thin film and significantly reduces the v_p of the QS_0 mode in the AlN/SiO_2 membrane [68], as shown in Figure 6-4(a). For instance, at the normalized SiO_2 thickness (h_{SiO2}/λ) of 0.3, the v_p of the QS_0 mode in the AlN/SiO_2 membrane nearly decreases to the half v_p of the S_0 mode in the AlN membrane for the normalized AlN thickness (h_{AlN}/λ) equal to 0.4. The v_p of the QS_0 mode in the AlN/SiO_2 membrane is no longer higher than that of the Rayleigh mode (5760 m/s) in the c-plane oriented AlN substrate [117] while the h_{SiO2}/λ increases up to 0.3. As are shown in Fig. 6-4(b), the v_p of the S_0 mode in the symmetrical SiO_2/AlN/SiO_2 membrane are much higher than that in the AlN/SiO_2 bilayer structure, especially when the thicker SiO_2 layer is utilized for temperature compensation at high temperatures. The S_0 mode in the SiO_2/AlN/SiO_2 membrane shows the phase velocity of roughly 2000 m/s higher than the QS_0 mode in the AlN/SiO_2 bilayer structure at h_{SiO2}/λ = 0.3 and h_{AlN}/λ = 0.3. Apparently the symmetrical SiO_2/AlN/SiO_2 sandwiched membrane shows the capability to enable high-frequency LWRs utilizing the S_0 mode.

6.2.3 Electromechanical coupling coefficients

The intrinsic electromechanical coupling coefficient k^2 is strongly correlated to the piezoelectric constants of the materials and the acoustic wave modes employed for the electro-acoustic resonators [118]. The intrinsic k^2 can be computed using an approximation method which is based on the v_p difference between the Lamb waves propagating under the electrically open and short boundary conditions [68]. Again, as described in Chapter 2, the intrinsic k^2 of the Lamb wave is defined as

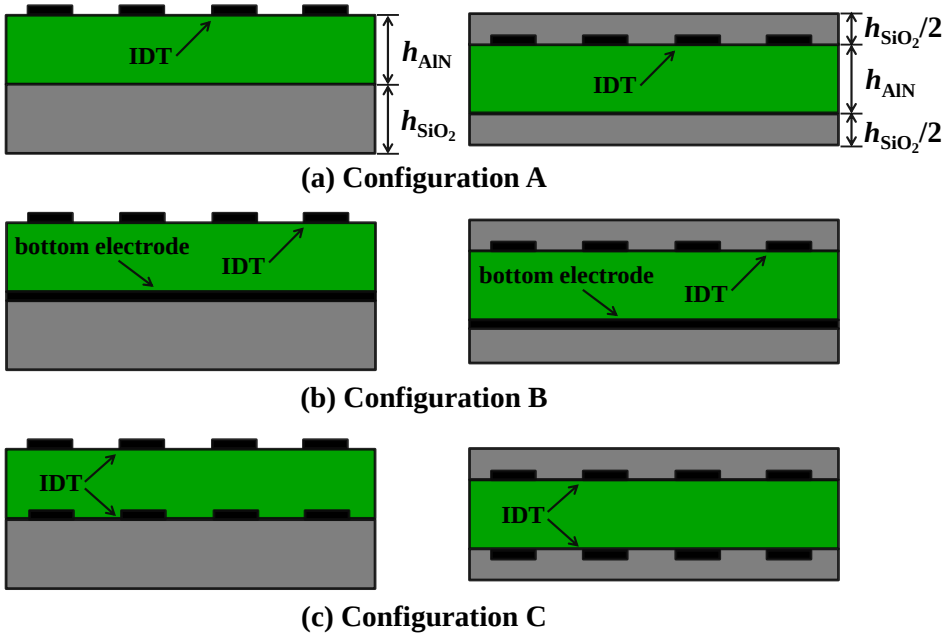

Figure 6-5. Three transducer configurations for the Lamb wave excitation using (a) an IDT on one surface of the AlN layer with the other open-circuited interface, (b) an IDT on one surface of the AlN layer with the other short-circuited interface, and (c) double IDTs on both sides of the AlN layer.

$$k^2 = \frac{2\left(v_o - v_m\right)}{v_o} \tag{2.23}$$

where v_o and v_m are the phase velocities for the electrically open and metallized surface conditions, respectively. The electrode thickness is assumed to be infinitely thin so the mass loading effect is neglected herein. Three transducer configurations for the LWRs based on the AlN/SiO_2 and $SiO_2/AlN/SiO_2$ composite plates are illustrated in Figure 6-5. To ensure a large intrinsic k^2, all the IDTs are placed on the surface of the piezoelectric AlN layer. Configuration A represents an IDT on one surface of the AlN layer with the other open-circuited interface; configuration B represents an IDT placed on one surface the AlN layer with the other short-circuited interface; configuration C represents two IDTs arranged on the both sides of the AlN layer.

As depicted in Figures. 6-6, 6-7 and 6-8, the intrinsic k^2 dispersion curves of the three transducer configurations on the AlN/SiO_2 and $SiO_2/AlN/SiO_2$ composite membrane are compared. Generally speaking, the intrinsic k^2 is deteriorated by the additional SiO_2 layer because of the acoustic energy absorption by the non-piezoelectric SiO_2 layer. Since the acoustic wave field tends to be more involved in the AlN layer of the symmetrical $SiO_2/AlN/SiO_2$ plate, the acoustic energy can be confined in the AlN plate to enable a higher k^2 for the S_0 mode [111], [64]. As a result, especially when the thick SiO_2 layers are employed on the both sides of the AlN layer, the intrinsic k^2 of the S_0 mode in the $SiO_2/AlN/SiO_2$ sandwiched plate is much larger than the QS_0 mode in the AlN/SiO_2 bilayer structure.

Intriguingly, unlike the k^2 deterioration in the AlN/SiO_2 composite membrane, the k^2 of the S_0 mode in the SiO_2/AlN/SiO_2 sandwiched plate is even larger than that in the AlN thin plate when h_{AlN}/λ = 0.4–0.5 is employed in the propagation medium. Therefore, all the three transducer configurations on the symmetrical SiO_2/AlN/SiO_2 sandwiched plate exhibit the maximal intrinsic k^2 at h_{SiO2}/λ < 0.2 and h_{AlN}/λ = 0.4–0.5 where the growing contribution of the e_{15} piezoelectric constant is more than the loading effect of non-piezoelectric material [49].

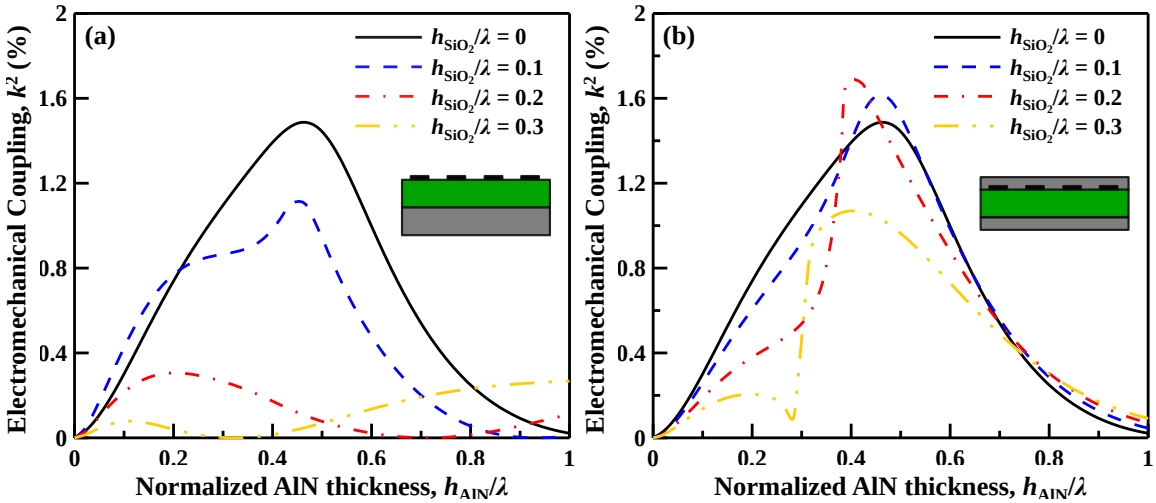

Figure 6-6. Calculated k^2 dispersion of the configuration A utilizing (a) the QS_0 mode in the AlN/SiO_2 bilayer membrane and (b) the S_0 mode in the symmetrical SiO_2/AlN/SiO_2 composite membrane.

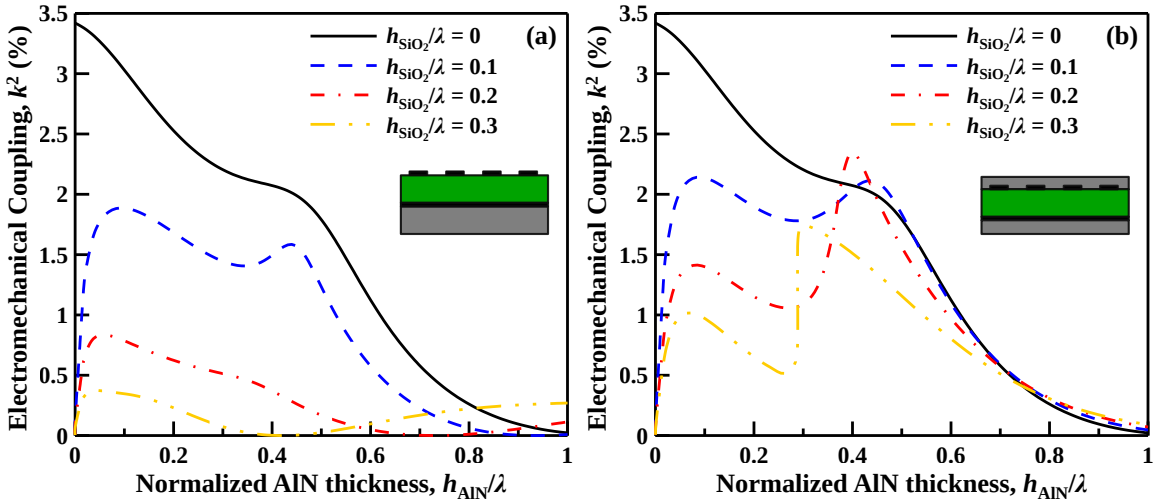

Figure 6-7. Calculated k^2 dispersion of the configuration A utilizing (a) the QS_0 mode in the AlN/SiO_2 bilayer membrane and (b) the S_0 mode in the symmetrical SiO_2/AlN/SiO_2 composite membrane.

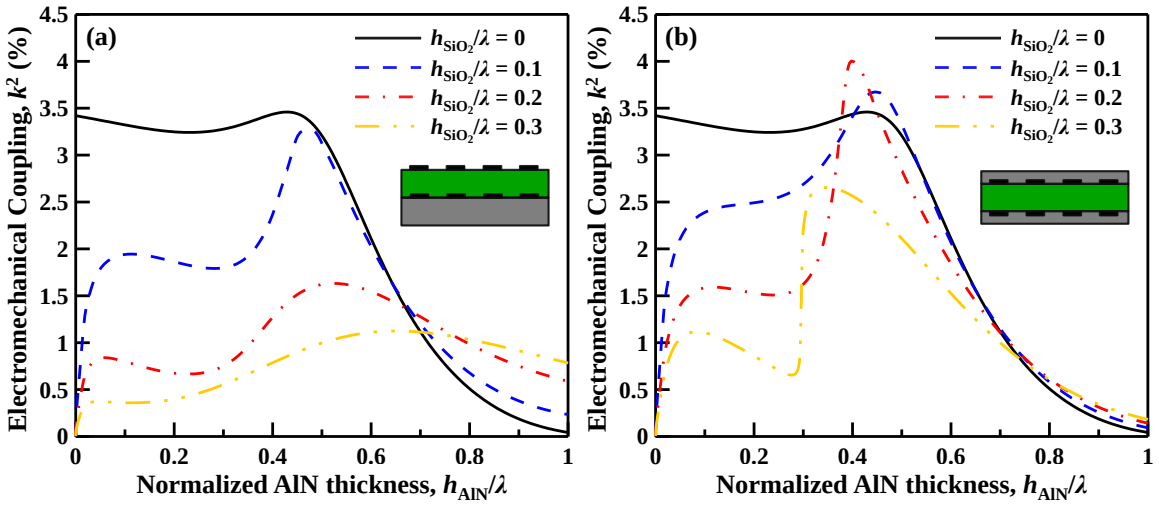

Figure 6-8. Calculated k^2 dispersion of the configuration A utilizing (a) the QS_0 mode in the AlN/SiO_2 bilayer membrane and (b) the S_0 mode in the symmetrical SiO_2/AlN/SiO_2 composite membrane.

Figure 6-9 compares the intrinsic k^2 dispersion curves of the S_0 Lamb wave mode in the SiO_2/AlN/SiO_2 composite membrane for the three transducer configurations at h_{SiO2}/λ = 0.1, 0.2, and 0.3. For any thickness ratio of AlN to SiO_2, configuration A always exhibits a smaller k^2 than configurations B and C because the electric field strength through the AlN plate of configurations B and C is higher, promoting the intrinsic k^2 strength of the S_0 mode [47], [72]. The acoustic wave excitation of configurations B and C is usually dominated by the e_{31} piezoelectric constant so the k^2 decreases steadily with the SiO_2 thickness in contrast to the excitation in configuration A, but fortunately they still exhibit relatively large k^2 strength when a thick SiO_2 layer is utilized for thermal compensation.

In particular, at the relatively thin AlN thickness region (i.e., h_{AlN}/λ < 0.1), configurations B and C offer a similar k^2 characteristic which is much larger than configuration A. Moreover, configurations A and B only require simple fabrication processes, whereas configuration C needs more complicated fabrication processes due to the required well alignment of the IDTs on the both sides of the AlN layer or an additional CMP process [40]. As a result, configuration B is preferred at the thin AlN thickness region (i.e., h_{AlN}/λ < 0.1) considering the microfabrication complexity. However, at the thick AlN thickness region (i.e., h_{AlN}/λ = 0.4–0.5), configuration C exhibits a very large k^2 up to 4% even when a thick SiO_2 layer is employed for thermal compensation at high temperatures; therefore, the double-sided IDTs configuration is favored while a large k^2 is desirable for the high temperature-compensated LWRs.

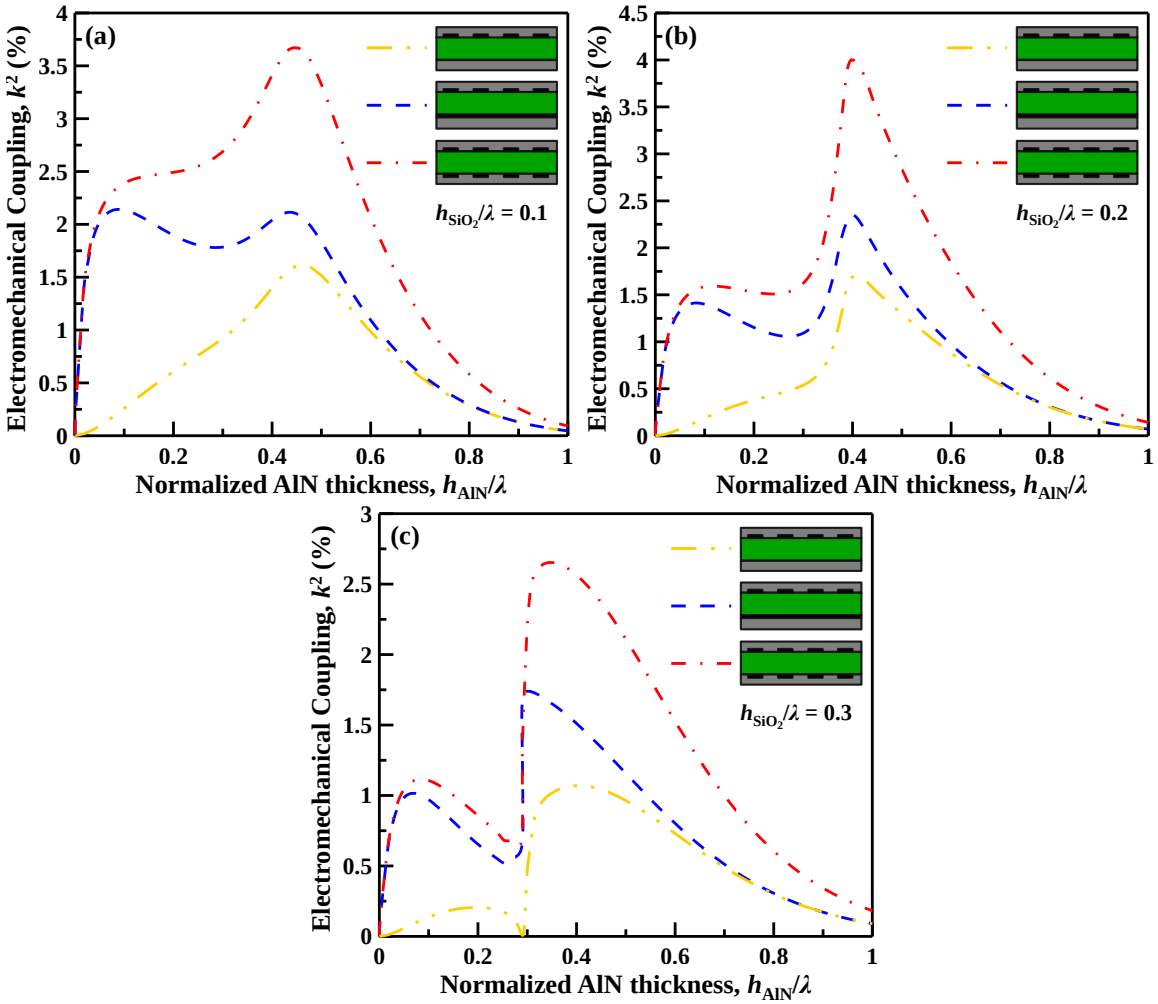

Figure 6-9. k^2 comparison of the S_0 mode in the symmetrical SiO_2/AlN/SiO_2 composite membrane with different transducer configurations at h_{SiO_2}/λ = (a) 0.1, (b) 0.2, and (c) 0.3.

6.3 Thermally stable SiO_2/AlN/SiO_2 Lamb wave resonators at high temperatures

The temperature-induced frequency drift of the resonator is related to the decrease in the material stiffness constants and thermal expansion coefficients. Neglecting the electrode thickness effect, the first-order *TCF* of the LWRs can be theoretically predicted using the method described in literatures [107]-[109]. The temperature coefficients of the material constants of AlN and SiO_2 used in the simulation are obtained from literature [69] and listed in Table 3-2.

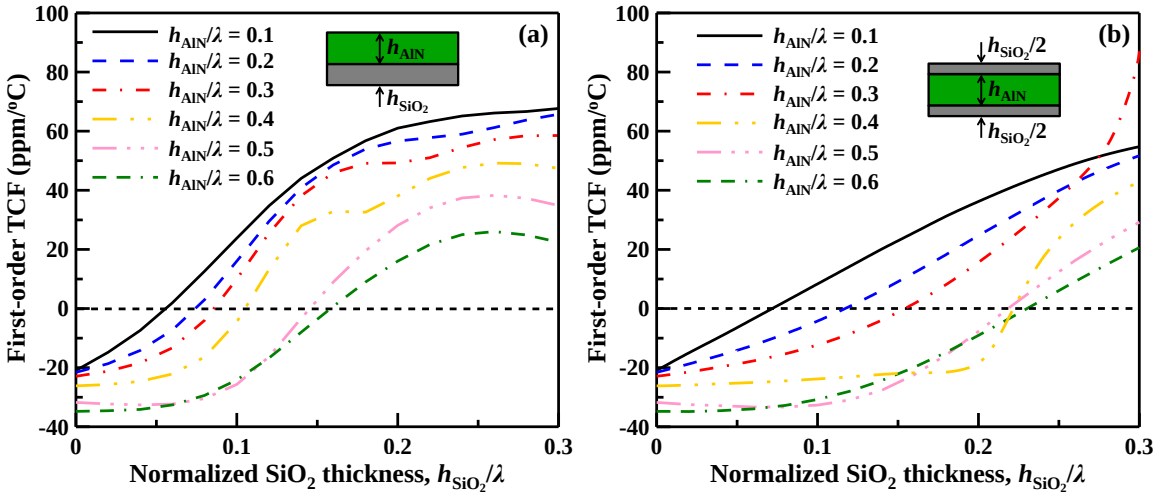

Figure 6-10. Simulated room temperature first-order *TCF*s of (a) the QS_0 mode in the AlN/SiO_2 bilayer membrane and (b) the QS_0 mode in the $SiO_2/AlN/SiO_2$ sandwiched membrane under different AlN and SiO_2 thicknesses.

The room temperature first-order *TCF*s of the QS_0 mode in the AlN/SiO_2 bilayer membrane and the S_0 mode in the $SiO_2/AlN/SiO_2$ sandwiched membrane for h_{AlN}/λ equal to 0.1, 0.2, 0.3, 0.4, 0.5 and 0.6 are depicted in Figure 6-10. By adding the SiO_2 layers onto the AlN thin film, the first-order *TCF* is generally increased with the thicker SiO_2 layer as shown in Figure 6-10. The turnover temperature can be determined by the first-order, second-order, and higher-order *TCF* terms. It should be noted that only when the second-order *TCF* is close to zero, the higher-order *TCF* terms would affect the turnover temperature.

To achieve temperature compensation at high temperatures, the first-order *TCF*s of the composite membrane could be intentionally positive at room temperature by designing h_{AlN}/λ and h_{SiO2}/λ [110]. Since the second-order *TCF*s of AlN and SiO_2 are both

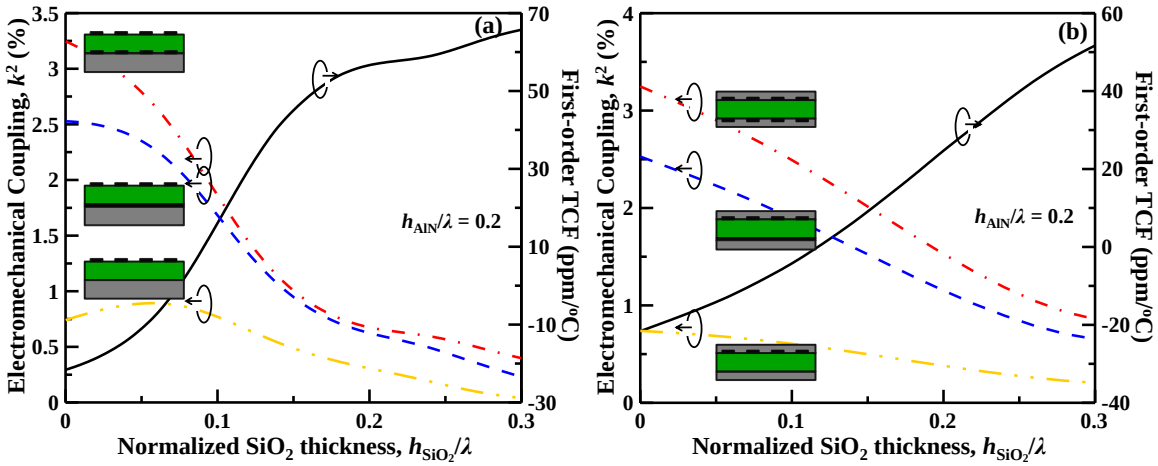

Figure 6-11. Trade-off between the first-order *TCF* and intrinsic k^2 of (a) the QS_0 mode in the AlN/SiO_2 bilayer membrane and (b) the S_0 mode in the $SiO_2/AlN/SiO_2$ sandwiched membrane at h_{AlN}/λ = 0.2.

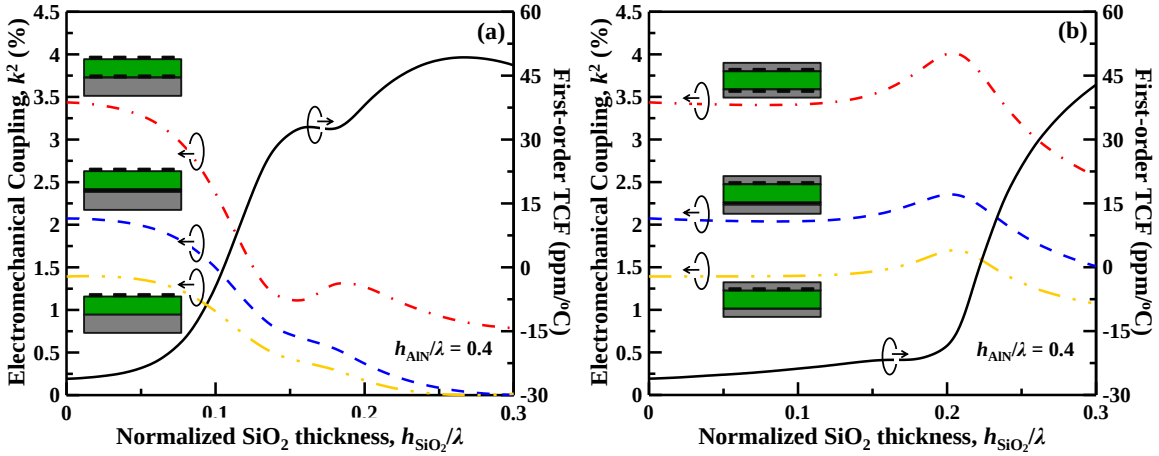

Figure 6-12. Trade-off between the first-order *TCF* and intrinsic k^2 of (a) the QS_0 mode in the AlN/SiO_2 bilayer membrane and (b) the S_0 mode in the SiO_2/AlN/SiO_2 sandwiched membrane at h_{AlN}/λ = 0.4.

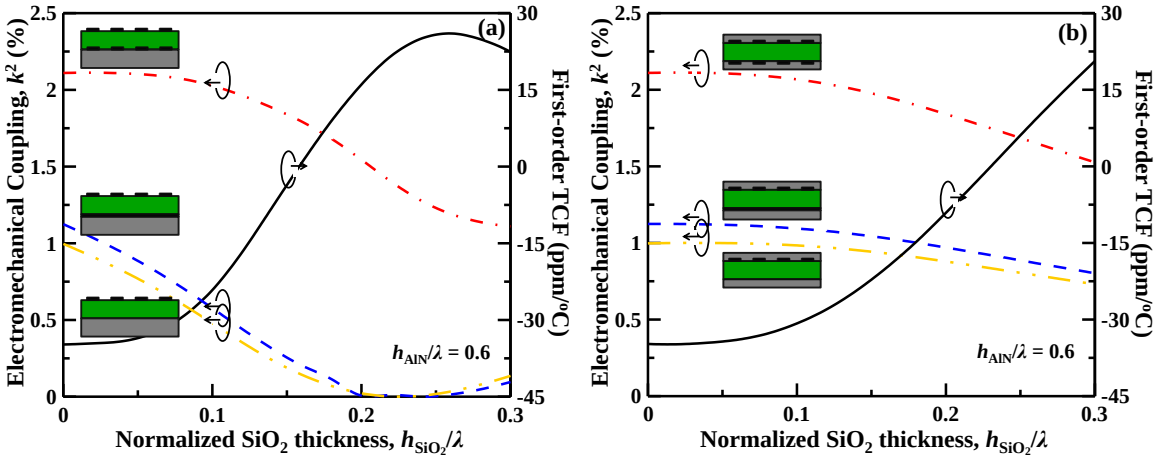

Figure 6-13. Trade-off between the first-order *TCF* and intrinsic k^2 of (a) the QS_0 mode in the AlN/SiO_2 bilayer membrane and (b) the S_0 mode in the SiO_2/AlN/SiO_2 sandwiched membrane at h_{AlN}/λ = 0.6.

negative [109], the turnover temperature is expected to be above room temperature, implying the SiO_2/AlN/SiO_2 LWRs become thermally stable at high temperatures. However, the first-order TCFs of the S_0 mode in the SiO_2/AlN/SiO_2 plate are slightly smaller than that of the QS_0 mode in the AlN/SiO_2 plate at the same h_{AlN}/λ and h_{SiO2}/λ, which means that the SiO_2/AlN/SiO_2 structure requires thicker SiO_2 layers for achieving temperature compensation at the same temperatures. Moreover, since reliable second-order *TCE*s of AlN and SiO_2 are not available in current literatures, the second-order *TCF*s and turnover temperatures are not predicable so far. Once reliable *TCE* data of AlN and SiO_2 are available in the future, the turnover temperature of the SiO_2/AlN/SiO_2 LWR can be accurately predicted.

In addition, there is a general trade-off relation between the first-order *TCF* and k^2 in the piezoelectric resonators [119]. For example, the k^2 of the QS_0 mode in the AlN/SiO2 bilayer plate is smaller than the S_0 mode in the SiO_2/AlN/SiO_2 sandwiched plate, whereas

the first-order *TCF* of the QS_0 mode in the AlN/SiO_2 composite membrane is closer to zero larger than the S_0 mode in the symmetrical $SiO_2/AlN/SiO_2$ membrane, as can be compared between (a) and (b) in Fig. 6-11, Fig. 6-12 and Fig.6-13. Furthermore, the trade-off between the *TCF* and k^2 can be observed in the same propagation medium. As shown in Fig. 6-12(a), the transducer configuration C on the AlN/SiO_2 composite membrane exhibits a locally minimal *TCF* at h_{SiO2}/λ = 0.18 and h_{AlN}/λ = 0.4 where the transducer has a locally maximal k^2. As illustrated in Fig. 6-11(b), all of the three transducer configurations on the symmetrical $SiO_2/AlN/SiO_2$ sandwiched plate show their maximal k^2 but a locally minimal first-order *TCF* at $h_{AlN} = 0.4\lambda$ and $h_{SiO2} = 0.2\lambda$, revealing the trade-off between the *TCF* and k^2 in the piezoelectric LWRs. The similar phenomena can also be found in Figure 6-11 and Figure 6-13 for different normalized AlN thicknesses. Despite the general trade-off, the sandwiched structure still provides the larger k^2 under the same *TCF* than the bilayer structure. For example, as for the case of h_{AlN}/λ = 0.4 and transducer configuration B, the $SiO_2/AlN/SiO_2$ sandwiched membrane achieves zero *TCF* at k^2 =2.24% and the AlN/SiO_2 bilayer membrane achieves zero *TCF* at k^2 =1.50%. From the discussions above, a correct transducer configuration with proper selections of the AlN and SiO_2 thicknesses enables the $SiO_2/AlN/SiO_2$ LWRs to have high phase velocity, large intrinsic electromechanical coupling coefficient, and good temperature-frequency stability at high temperatures.

6.4 Conclusions

In this chapter, we present the theoretical investigation on the acoustic characteristics of the thermally stable $SiO_2/AlN/SiO_2$ LWRs utilizing the S_0 mode for high temperature applications. The symmetrical $SiO_2/AlN/SiO_2$ sandwiched plate experiences the less temperature-induced bending deformation than the conventional AlN/SiO_2 bilayer plate when the operation temperature arises from room temperature to 600°C. The symmetrical $SiO_2/AlN/SiO_2$ sandwiched plate also enables the pure S_0 mode which shows the higher v_p and larger k^2 than the QS_0 mode in the AlN/SiO_2 bilayer plate. In the SiO2/AlN/SiO2 sandwiched membrane, the single IDT with the bottom electrode configuration offers a simple process flow and a large k^2 at the relatively thin h_{AlN} region ($h_{AlN} = 0.1\lambda$). The double-sided IDTs configuration provides a large k^2 up to 4% at the relatively thick hAlN region ($h_{AlN}/\lambda = 0.4\lambda$) even when the thick SiO_2 layers are employed for thermal compensation at high temperatures. Based on the correct choices of the AlN and SiO2 thicknesses in the symmetrical $SiO_2/AlN/SiO_2$ sandwiched membrane, the LWRs can be thermally stable and retain a large k^2 at high temperatures.

Chapter 7

High-Frequency and Low-Resonance-Impedance Lamb Wave Resonators Utilizing the S_1 Mode

In this work, a high-frequency (f_s) and low-resonance-impedance (Z_{min}) Lamb wave resonator utilizing the first order symmetric (S_1) mode propagating in highly textured AlN layers is presented. In order to achieve the larger electromechanical coupling coefficient and high phase velocity as well as avoid the negative group velocity in the S_1 Lamb wave mode, the 4-μm-thick AlN layer and 3-μm-wide finger electrodes are employed in the Lamb wave resonator design. The experimental results show that despite the S_1 mode shows a slightly lower Q than the S0 mode, the S_1 mode presents a Z_{min} of 94 Ω at 1.34 GHz, lower than the Z_{min} equal to 224 Ω of the S_0 mode at 878.3 MHz.

7.1 Introduction

MEMS resonators offer fascinating prospects for many important applications including frequency selection, timing reference, and physical sensing. In general, a low resonance impedance (Z_{min}) at high resonance frequency (f_s) are the invariably requests for MEMS resonators since the low Z_{min} can provide a low phase noise for timing applications or convenient impedance match for electronic systems. The high operation frequency can increase the data rate for electronics and enhance the sensitivity for sensing applications [88]. However, while scaling down the dimensions of MEMS resonators enables a high resonance frequency, the miniaturization of excitation area would significantly decrease the coupling coefficient and deteriorate the losses, which increase the motional impedance. Consequently, a long-standing interest in the MEMS resonators is the ability to achieve high fs and low Z_{min} at the same time.

Among various MEMS resonators, piezoelectric AlN Lamb wave resonators which are transduced by the IDTs recently capture attentions since they possess both advantages of SAW devices and FBARs [28]: the lithographically defined resonance frequency and

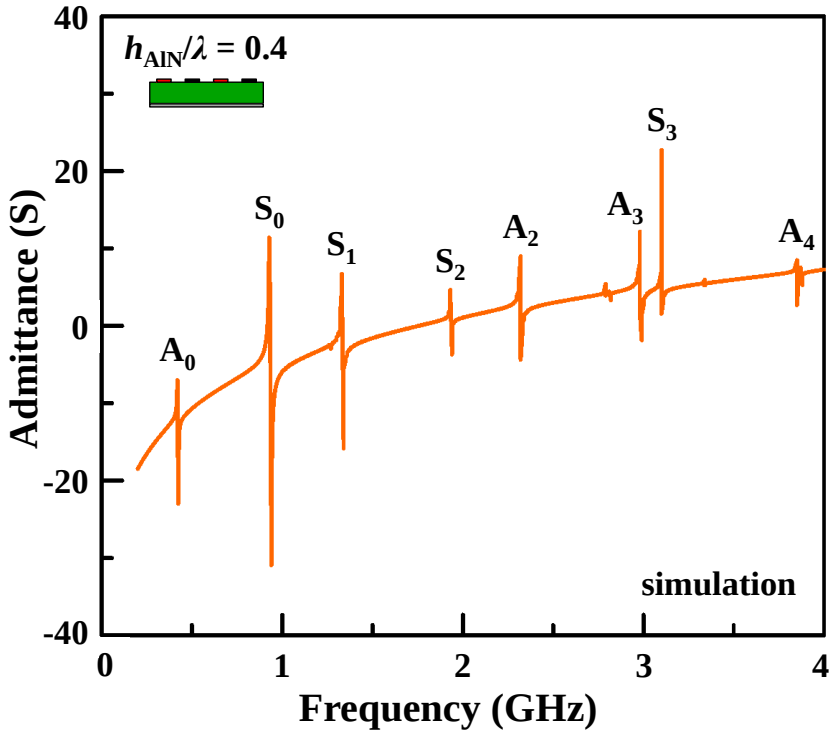

Figure 7-1. Simulated frequency response for a wide spectrum of a Lamb wave resonator on 0.4λ thick AlN and with floating bottom electrode.

the high phase velocity, respectively. For all Lamb wave modes propagating in an AlN thin plate, the S_0 mode is particularly preferred because it shows a phase velocity close to 10,000 m/s, a moderate electromechanical coupling coefficient, and a low dispersive phase velocity characteristic [40], [72], [120]. However, the quality factor of the Lamb wave resonator using the S_0 mode is degraded to 500 while the IDT finger width is decreased to the nanometer scale for a super-high f_s at 3.46 GHz [121], [122].

The use of high-order Lamb wave modes in the AlN plate is an alternative approach to achieve a high f_s for the piezoelectric resonators. Recently the first-order symmetric (S_1) Lamb wave mode in an AlN thin plate has been demonstrated have a high phase velocity exceeding 20,000 m/s; however, the S_1 mode showed three resonance peaks because they exhibit a negative group velocity when the AlN plate thickness (h_{AlN}) normalized to the wavelength (λ) is equal to 0.167 [38]. In addition, the Q of 1100 in the S_1 mode is not satisfied. In this work, in order to achieve a larger electromechanical coupling coefficient and a positive group velocity in the S_1 Lamb wave mode, the 4-μm-thick AlN layer and 3-μm-wide finger electrodes are employed in the Lamb wave resonators, resulting in a normalized AlN thickness (h_{AlN}/λ) equal to 0.333. The experimental results show that the Lamb wave resonator utilizing the S_1 mode presents a Z_{min} = 94 Ω at 1.34 GHz, lower than the Z_{min} = 224 Ω of that utilizing the S_0 mode at 878.3 MHz.

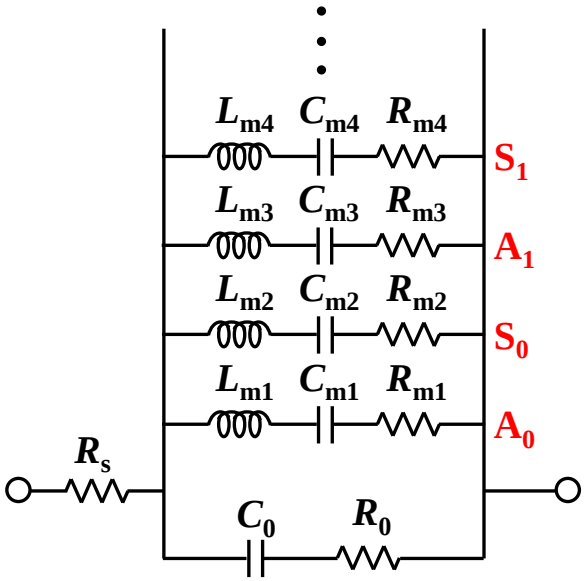

Figure 7-2. Multi-resonant MBVD circuit. Each leg corresponds to a resonance mode.

7.2 Lamb Wave Modes Propagating in an AlN Plate

7.2.1 The Multi-Modes Resonance

As introduced in chapter 2, there are a series of Lamb wave modes for the symmetric and antisymmetric mode shapes. For a Lamb wave resonator, all these modes coexist at specific frequencies. Figure 7-1 shows an example of the frequency response for some of the modes in a Lamb wave resonator with floating bottom electrode on a 0.4 thick AlN plate simulated using FEA. The A_1 mode is missing in this plot because the intrinsic electromechanical coupling coefficient is near-zero at this AlN thickness under the floating-bottom-electrode configuration, which can be found in Figure 7-4(b). Since the quality factors are not considered and the data in the plot is limited, the height of each mode in the simulated admittance plot doesn't indicate any parameter and does not match with the measured result.

The MBVD circuit model for a resonator that with multi- Lamb wave modes is depicted in Figure 7-2. Each motional branch corresponds to a resonance mode. The static arm is common to all Lamb wave modes. So the resonance frequency and effective coupling coefficient for a mode is:

$$f_{s,i} = \frac{\omega_{s,i}}{2\pi} = \frac{1}{2\pi}\sqrt{\frac{1}{L_{m,i}C_{m,i}}} (i = 1, 2, 3...), \tag{7.1}$$

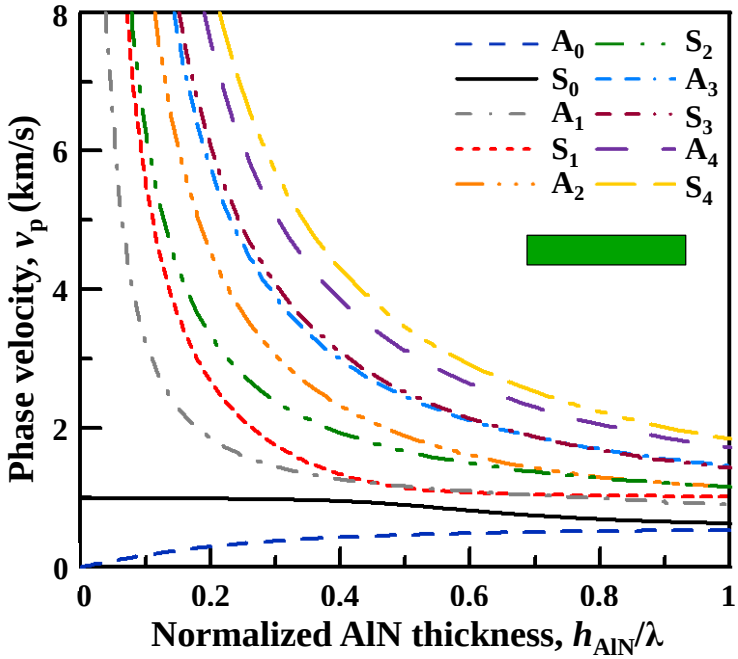

Figure 7-3. FEA simulations of the phase velocities of the first ten modes in the AlN Lamb wave resonators

$$k_{\mathrm{eff,i}}^2 = \frac{\pi^2}{8}\left(\frac{C_{\mathrm{m,i}}}{C_0}\right)(i = 1, 2, 3...), \tag{7.2}$$

where i is the i-th resonance corresponding the Lamb wave mode shown in Figure 7-2.

7.2.2 Phase Velocities

The simulated phase velocities for the first ten Lamb wave modes are shown in Figure 7-3. The higher modes (S_1, A_1, S_2, A_2, …) other than the fundamental modes have very large phase velocities and very steep dispersions when the AlN is relatively thin (h_{AlN}/λ < 0.3). Although the large phase velocities can enable ultra-high frequencies, the steep dispersion makes it almost impossible to fabricate the device working at a specific accurate frequency, which means the fabrication tolerance is terrible so that the higher modes are not applicable when the AlN is thinner than 0.3λ.

Fortunately, when AlN becomes relatively thick (h_{AlN}/λ > 0.3), the dispersion slope becomes flat that can give reasonable fabrication tolerance. What's more, the phase velocities of the higher modes are much larger than the S_0 mode, showing potential in enabling the ultra-high frequency devices (f_s>2 GHz).

7.2.3 Electromechanical Coupling Coefficients

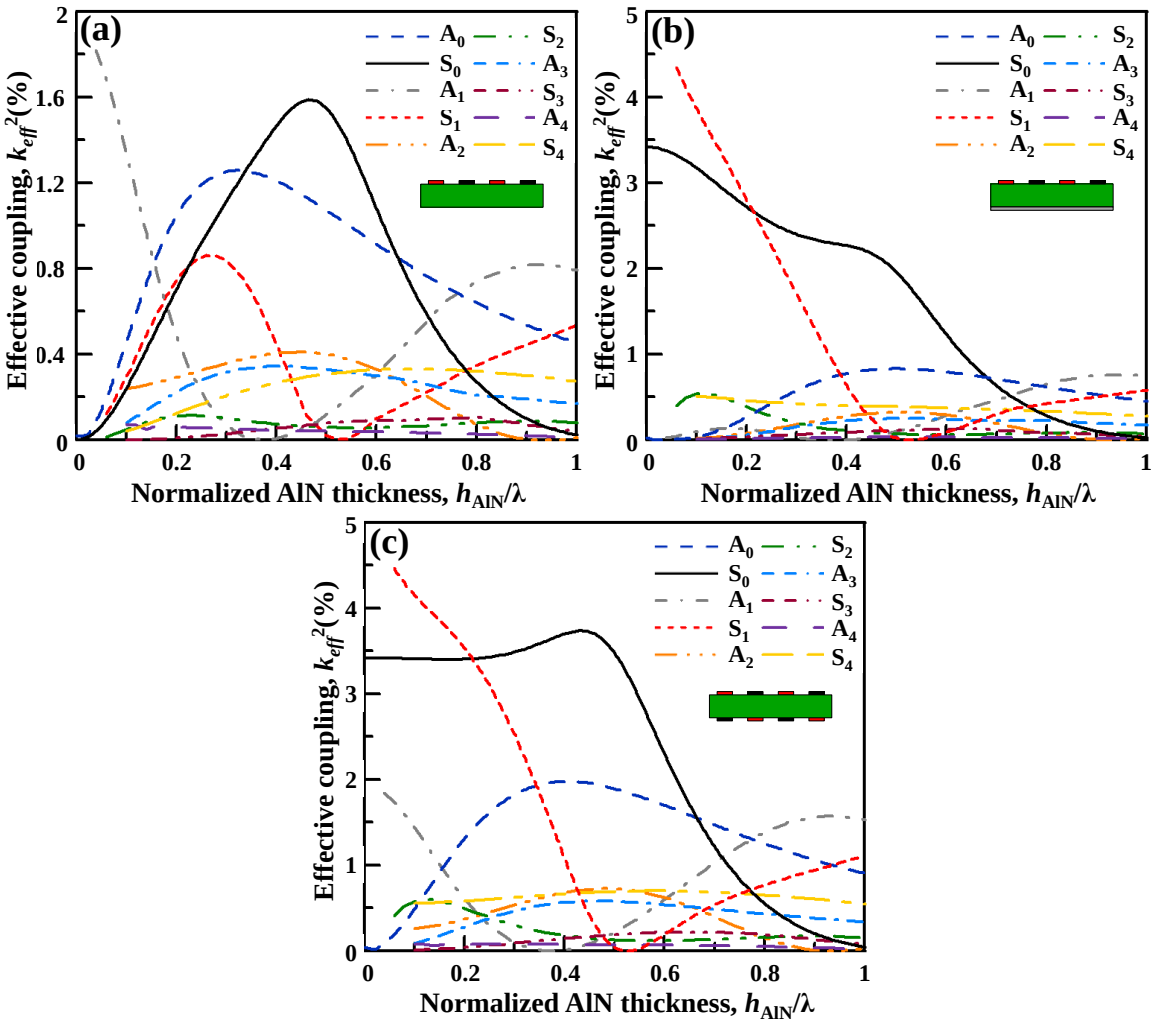

Figure 7-4. FEA simulations of effective coupling coefficients of AlN Lamb wave resonators for the (a) single IDT electrode configuration, (b) the IDT-floating BE electrode configuration, and (c) the double-IDT electrode configuration for the first ten Lamb wave modes.

The simulated effective coupling coefficients for the first ten Lamb wave modes and resonators for the single IDT electrode configuration, the IDT-floating BE electrode configuration, and the double-IDT electrode configuration are shown in Figure 7-4(a)-(c). It can be observed that except the S_0 mode, some other modes also show moderate or high electromechanical coupling coefficients under some electrode configurations. For example, the A_1 mode shows slightly larger k^2_{eff} under the single-IDT configuration when the AlN is relatively thin (h_{AlN}/λ > 0.3) and relatively thick (h_{AlN}/λ > 0.3). Intriguingly, the S_1 mode generally shows comparable k^2_{eff} with the S_0 mode. Under the floating-bottom-electrode and double-IDT configurations, the k2eff of the S_1 mode is larger than 1% as long as AlN is thinner than 0.4 , which is the common AlN thickness range for a Lamb wave resonator (Figure 7-4(b), (c)).

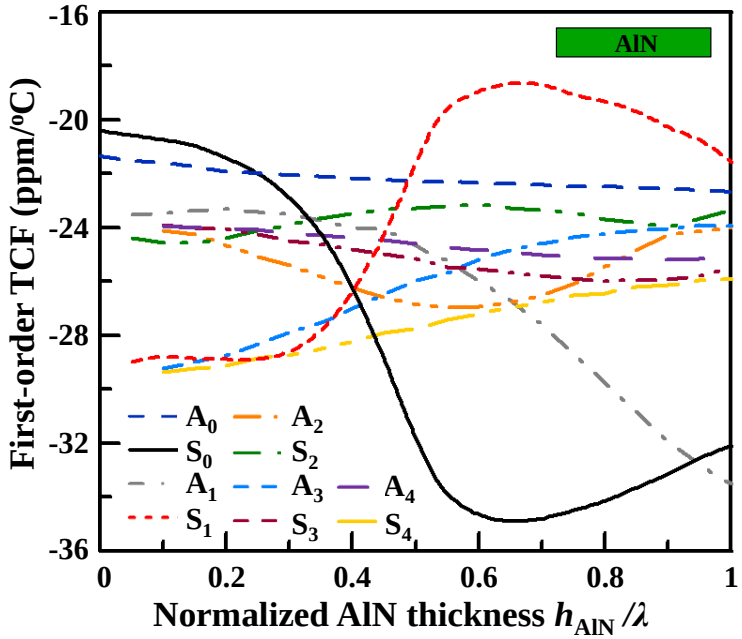

Figure 7-5. Simulated *TCF*s of the first ten Lamb wave modes in AlN plate.

7.2.4 Temperature Coefficients of Frequency

The *TCF*s for the first ten Lamb wave modes are also simulated for different thicknesses of AlN plates, as shown in Figure 7-5. All the *TCF*s of the first ten Lamb wave modes propagating in the AlN membrane that is thinner than λ are between -35 ppm/˚C and -18 ppm/˚C. In contrast to the S_0 mode that exhibits larger *TCF* when the AlN is thicker, the S_1 mode exhibits larger *TCF* when the AlN is thicker. The dispersion of the *TCF*s is due to the dispersion of the phase velocities of the Lamb wave modes. Nonetheless, there is little difference between all the *TCF* values, meaning the consideration of *TCF* is not needed when we design the Lamb wave resonator based on pure AlN utilizing different modes.

7.3 Lamb Wave Resonators Utilizing the S_1 Mode

Recently the S_1 Lamb wave mode in the AlN thin plate has been demonstrated have a high phase velocity exceeding 20,000 m/s; however, the S_1 mode showed three resonance peaks because they exhibit a negative group velocity when the AlN plate thickness (h_{AlN}) normalized to the wavelength (λ) is equal to 0.167 [38]. In addition, the *Q* of 1100 in the S_1 mode is not satisfied. In this work, in order to achieve a larger electromechanical coupling coefficient and a positive group velocity for the S_1 Lamb wave mode, the 4-μm-thick AlN layer and 3-μm-wide finger electrodes are employed in the Lamb wave

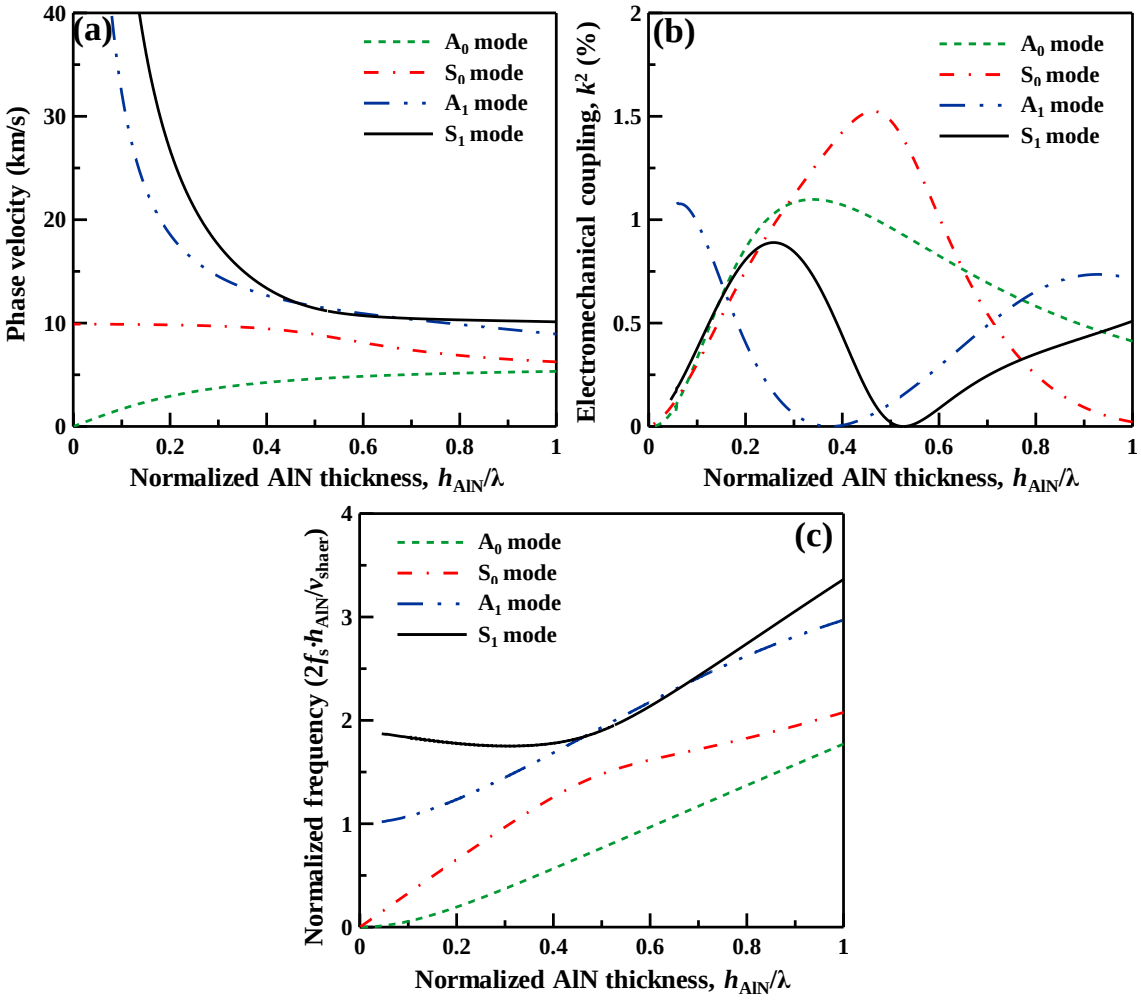

Figure 7-6. (a) Phase velocity dispersion, (b) electromechanical coupling dispersion, and (c) the phase velocity curve normalized to the shear BAW velocity of the first four Lamb wave modes propagating in an AlN plate.

resonators, creating a normalized AlN thickness (h_{AlN}/λ) equal to 0.333. The experimental results show that the Lamb wave resonator utilizing the S_1 mode presents a Z_{min} = 94 Ω at 1.34 GHz, smaller than the Z_{min} = 224 Ω of that utilizing the S_0 mode at 878.3 MHz.

Again, Figure 7-6(a) shows the phase velocity dispersion of the first four Lamb wave modes propagating in an AlN plate. As depicted in Figure 7-6(a), the first-order antisymmetric (A_1) and S_1 Lamb wave modes in an AlN thin plate have steep phase velocities when the AlN plate thickness is thin, making them not preferred for MEMS resonators although they have much higher phase velocities than the S_0 mode. It is noted that the phase velocity dispersion of the S_1 Lamb wave mode becomes much smooth while a thicker AlN plate (i.e., $h_{AlN}/\lambda > 0.3$) is employed. As a result, it is possible to enable the acoustic resonators utilizing the S_1 Lamb wave mode in the piezoelectric AlN plate.

Figure 7-6(b) illustrates the electromechanical coupling dispersion of the first four Lamb wave modes in an AlN plate with a non-metallized (open-circuited) bottom surface. As shown in Figure 7-6(b), when the normalized AlN thickness is close to 0.3, the S_1 Lamb wave mode exhibits a larger k^2, enabling the electroacoustic resonators utilizing the S_1 mode in the AlN plate.

In order to investigate the group velocity of the first four Lamb wave modes in the AlN plate, the phase velocity curve can be normalized to the wavelength and the phase velocity of shear bulk acoustic wave (v_{shear} = 6,106 m/s) as shown in Figure 7-6(c) [38]. When the normalized AlN thickness h_{AlN}/λ is about 0.3, the S_1 mode shows a zero group velocity [123] and while the h_{AlN}/λ is larger than 0.3, the S_1 mode can exhibit a positive group velocity, indicating the S_1 mode is able to propagate out the IDT region. It concludes that the S_1 mode exhibits a smooth phase velocity dispersion, a larger k^2, and a positive group velocity if the h_{AlN}/λ is larger than 0.3. Therefore, 4-μm-thick AlN plate and 3-μm-wide electrodes are employed in the Lamb wave resonator and result in a h_{AlN}/λ equal to 0.333 in this work.

7.4 Experimental Results

To obtain highly c-axis oriented AlN thin films and prevent the interface loss induced by the bottom electrodes [72], the Lamb wave resonators are intentionally designed with no backside metallization in this study. The 4-μm-thick c-axis oriented AlN films were deposited on the substrate using AC reactive magnetron sputtering at approximately 350

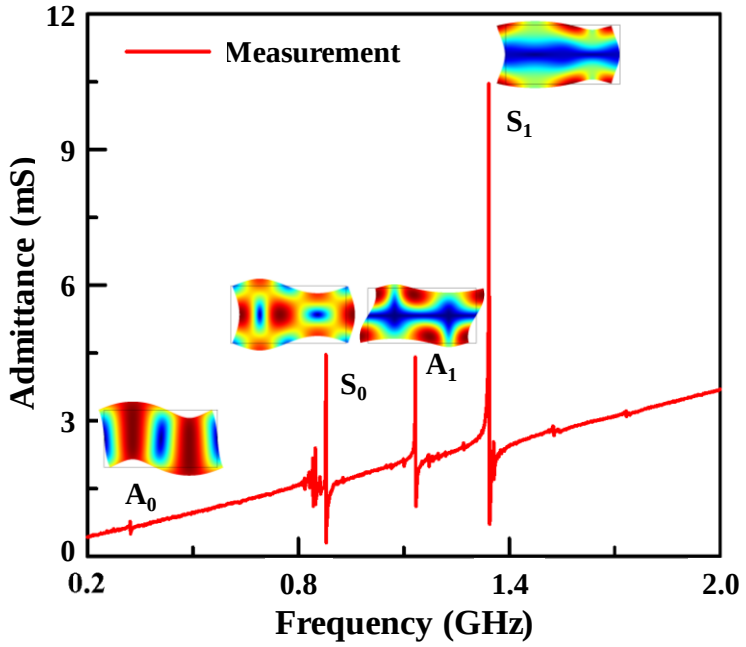

Figure 7-7. The measured frequency spectrum of the Lamb wave resonator on a 4-μm-thick AlN plate.

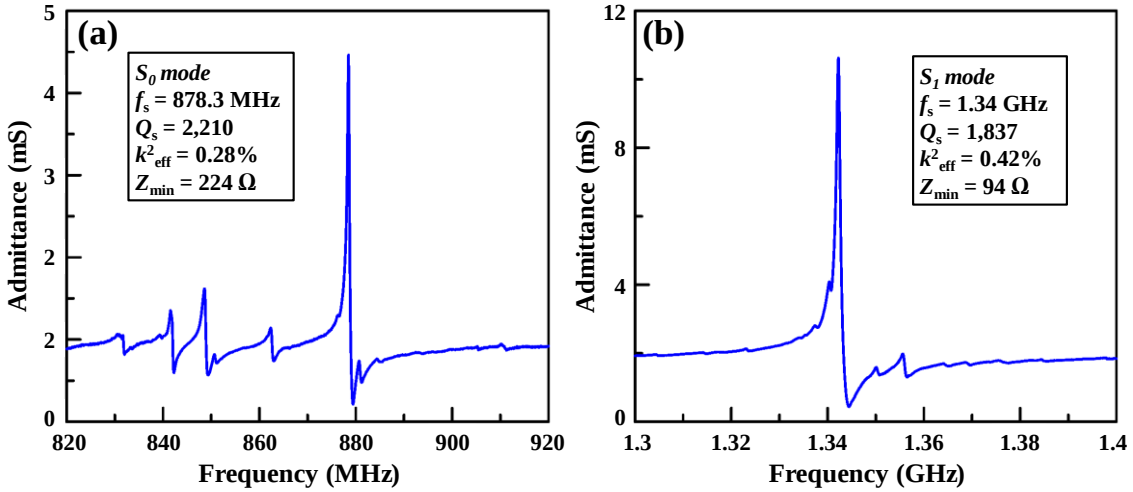

Figure 7-8. The measured frequency spectrum of the Lamb wave resonator on a 4-μm-thick AlN plate.

°C. The AlN film was examined by XRD and the 4-μm-thick AlN film shows a FWHM value of 1.13°, implying the AlN film owns excellent crystallinity.

The AlN Lamb wave resonators in this study were fabricated using a two-mask fabrication process flow which was previously published in [34]. The AlN Lamb wave resonator has 13 strips of 100-nm-thick Pt IDT electrodes, the electrode width is 3 μm, and the IDT aperture is 180 μm.

Figure 7-7 depicts the measured broadband frequency spectrum of the AlN Lamb wave resonator measured from 200 MHz to 2 GHz. COMSOL FEA multiphysics software was used to simulate the resonance mode shapes of the Lamb wave modes propagating in the AlN plate and the corresponding resonance mode shapes are inserted as insets in Figure 7-7. The experimental results show that the S_1 mode has a Z_{min} lower than the other three modes.

Figure 7-8 shows the measured admittance spectrum of the Lamb wave resonator using the S_0 mode in the 4-μm-thick AlN plate and it shows a low k^2_{eff} of 0.28%, a Q of 2,210, and a Z_{min} of 224 Ω at 878.3 MHz. However, there are several unwanted spurious modes occurring around the S_0 Lamb wave mode and the sources of these spurious modes are still under investigation.

In addition, as shown in Figure 7-7, the Lamb wave resonator utilizing the S_1 mode in the 4-μm-thick AlN plate shows a larger k^2_{eff} of 0.42%, a slightly lower Q of 1,837, a smaller Z_{min} of 94 Ω, and a higher f_s of 1.34 GHz than the S_0 Lamb wave mode. The experimental results show that the S1 mode exhibits a superior performance over the S_0 mode while the h_{AlN}/λ is equal to 0.333. Moreover, in comparison to the previous work in [38], the piezoelectric resonator using the S_1 mode shows a clean frequency spectrum in this work as the S_1 mode has a positive group velocity at h_{AlN}/λ = 0.333. It should be noted that the Q and k^2_{eff} reported herein are not optimal and can be improved to a large extent. For example, the Q of the S_1 Lamb wave mode can be boosted by reducing the anchor loss [34], [100] or interface loss [124].

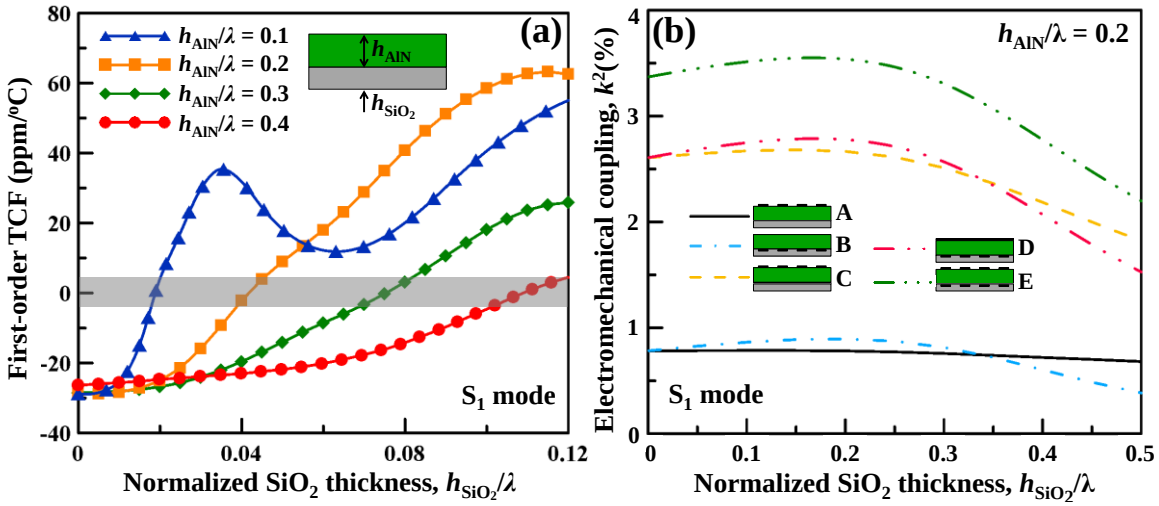

Figure 7-9. Simulated (a) first-order *TCF* and (b) electromechanical coupling strength of the S_1 mode in AlN/SiO_2 composite plates.

7.5 Temperature Compensation of the S_1 mode

By adding a compensating layer of SiO_2 with an appropriate thickness, a Lamb wave resonator based on a stack of AlN and SiO_2 layers can achieve a zero first-order *TCF*. By calculation the electromechanical coupling coefficient and the group velocity at of the S_1 Lamb wave mode, a relatively thin AlN and SiO_2 thickness combination can be chosen that offers a low-*TCF*, large k^2 and a positive group velocity simultaneously. This new SiO_2/AlN structure utilizing the S_1 Lamb wave mode simultaneously offers superior temperature stability, high f_s, large k^2, and low spurious mode level.

Figure 7-9 shows the k^2 and first-order *TCF* at different AlN and SiO_2 thickness combinations. By designing the SiO_2/AlN thickness ratio a near-zero *TCF* at room temperature can be obtained. For example, for $h_{AlN}/\lambda \sim 0.2$, a thickness for SiO_2 of $h_{SiO2}/\lambda \sim 0.04$ can be chosen, as shown in Figure 7-9(a). What's more, from Figure 7-9(b), the electrode configuration C, which has a top IDT on the AlN layer and an electrode at the interface, offers large k^2 at the preferred AlN and SiO_2 thickness combination and also a simple fabrication process, since the IDT electrode is not in the interface. These simulation results lay the foundation for temperature-compensated, high-f_s and k^2 SiO_2/AlN Lamb wave resonators utilizing the S_1 mode.

7.6 Conclusions

The use of high-order Lamb wave modes in the AlN plate is an alternative approach to achieve a high f_s for the piezoelectric resonators. Recently the S_1 Lamb wave mode in the AlN thin plate has been demonstrated have a high phase velocity exceeding 20,000 m/s; however, the S_1 mode showed three resonance peaks because they exhibit a negative group velocity when the AlN plate thickness (h_{AlN}) normalized to the wavelength is equal to 0.167 [38]. In addition, the Q of 1100 in the S_1 mode is not satisfied. In this work, in order to achieve a larger electromechanical coupling coefficient and a positive group velocity for the S_1 Lamb wave mode, the 4-μm-thick AlN layer and 3-μm-wide finger electrodes are employed in the Lamb wave resonators, creating a normalized AlN thickness (h_{AlN}/λ) equal to 0.333. The experimental results show that the Lamb wave resonator utilizing the S_1 mode presents a Z_{min} = 94 Ω at 1.34 GHz, smaller than the Z_{min} = 224 Ω of that utilizing the S_0 mode at 878.3 MHz.

In addition, the compensation technique for the Lamb wave resonators using the S_1 mode is explained and the simulation result is presented.

Chapter 8

Conclusions

The piezoelectric AlN LWRs present a promising resonator technology which offers post-CMOS compatibility, multiple frequencies on a single chip, small size, low motional impedance, medium k_{eff}^2 and medium Q. The AlN LWRs show prospects to revolutionize the current wireless communication systems, such as the application in the frequency references or bandpass filters. Enjoying the merits of both SAW resonator and FBAR, the low deposition temperature of the AlN thin film and the Si-based fabrication processes of the LWRs show potential integration with the CMOS circuits, and the AlN LWRs can offer multiple frequencies on one die for future realization of a single chip RF front-end. Moreover, the LWRs present a superior in low motional resistances to the electrostatic resonators, allowing interfacing with the standard 50 Ω RF systems. In order to enhance the performance of the electronic system, the integration of micromechanical resonators directly onto the circuitry is an excellent approach to avoid unnecessary energy loss. However, the performance parameters needs to be further improved to further enable the low-loss, thermally stable, and wide bandwidth filters, and the low-loss, precise and stable oscillators. This dissertation addresses a number of issues and demonstrated the high-performance (high-f_s., large-k^2, high-Q, low-TCF, and low-resonance impedance (Z_{min})) piezoelectric AlN LWRs to fulfill the technical requests for the RF front-end.

The selection of electrode materials and thicknesses has large impact on the performance of micro-acoustic resonators. Although the effect of electrode materials and thicknesses has been intensively studied for the SAW resonators and FBARs, the dispersive characteristic of the Lamb wave makes it complicated and different from SAW resonators or FBARs, and there is yet no systematic study for the Lamb wave resonators. For the first time, this study adopts the finite element analysis to investigate the influence of electrodes on the Lamb wave resonators using the S_0 mode. Four types of electrode configurations for the AlN Lamb wave resonators are considered here and compared for the pure AlN structure. For each electrode configuration, the effect of metal electrodes on the phase velocities and effective coupling coefficients are calculated and analyzed. The phase velocity is directly related to the density and equivalent phase velocity in the metal, while the coupling coefficients depend on the density and acoustic impedance of the metal. Large-Z material is preferred for the IDT and light material is favored for the bottom electrode to optimize the effective coupling coefficient. The impact of the electrode thickness is also analyzed: thicker metal for the IDT loads the k^2_{eff} more when AlN is thin and enhance k^2_{eff} more when AlN is relatively thick. These results reveal the

potential of high-f_s and large–k^2_{eff} AlN Lamb wave resonators by careful selection of electrodes for frequency selection applications.

A new design approach for improving the anchor loss of the Lamb wave resonators is presented. By using the butterfly-shape AlN plate, the displacement in the tethers is efficiently suppressed and the energy loss via the tethers is then reduced. The 59˚ butterfly-shaped resonator enables an unloaded Q up to 4,758, showing a 1.42× enhancement over the conventional resonator. In addition, the experimental results are in good agreement with the simulated predictions by the 3D PML-based FEA model, confirming that the butterfly-shaped AlN thin plate can efficiently eliminate the anchor dissipation. The Q of the Lamb wave resonators is expected to be significantly increased using the butterfly-shaped plate if the interfacial loss can be minimized by well-controlled interface stresses under optimized metal deposition conditions. In addition, the butterfly-shaped plate didn't introduce spurious modes on a wide spectrum, compared to other Q increase techniques. By employing the butterfly-shape AlN plates with rounded tether-to-plate transition which has smaller tether-to-plate angle, the suppression in the anchor loss and enhancement in the Q is even more effective. The simulated displacement profiles show that the butterfly-shaped plate significantly reduces the displacement at the plane center, and the rounded one offers a better efficiency on the displacement suppression at the plane center. The simulated Q_{anchor} using the 3D PML-based FEA model also confirm that the rounded butterfly-shape plates can successfully minimize the anchor loss and boost the Q_{anchor}. The butterfly-shaped resonator with 45˚ beveled tether-to-plate transition yields a Q of 1,979 which upwards 30% over a conventional rectangular resonator; another AlN LWR on the butterfly-shaped plate with rounded tether-to-plate transition yields a Q of 2,531, representing a 67% improvement. By comparing the performances with different number of electrodes it is found that the butterfly shape shows constant enhancement on Q and a reduction on Z_{min}. When the *NE* becomes larger, the Z_{min} becomes smaller and the loaded Q decreases because the lower R_m causes an obvious electrical loading effect on the Q. When *NE* becomes too large (> 40), there are strong spurious modes due to internal reflection of the IDTs, which is not preferable.

We also presented the theoretical investigation on the acoustic characteristics of the thermally stable SiO_2/AlN/SiO_2 LWRs utilizing the S_0 mode for high temperature applications. The symmetrical SiO_2/AlN/SiO_2 sandwiched plate experiences the less temperature-induced bending deformation than the conventional AlN/SiO_2 bilayer plate when the operation temperature arises from room temperature to 600°C. The symmetrical SiO_2/AlN/SiO_2 sandwiched plate also enables the pure S_0 mode which shows the higher v_p and larger k^2 than the QS_0 mode in the AlN/SiO_2 bilayer plate. In the SiO2/AlN/SiO2 sandwiched membrane, the single IDT with the bottom electrode configuration offers a simple process flow and a large k^2 at the relatively thin h_{AlN} region (h_{AlN} = 0.1λ). The double-sided IDTs configuration provides a large k^2 up to 4% at the relatively thick hAlN region (h_{AlN}/λ = 0.4λ) even when the thick SiO_2 layers are employed for thermal compensation at high temperatures. Based on the correct choices of the AlN and SiO2 thicknesses in the symmetrical SiO_2/AlN/SiO_2 sandwiched membrane, the LWRs can be thermally stable and retain a large k^2 at high temperatures.

The use of high-order Lamb wave modes in the AlN plate is an alternative approach to achieve a high f_s for the piezoelectric resonators. Recently the S_1 Lamb wave mode in the AlN thin plate has been demonstrated have a high phase velocity exceeding 20,000 m/s; however, the S_1 mode showed three resonance peaks because they exhibit a negative group velocity when the AlN plate thickness (h_{AlN}) normalized to the wavelength is equal to 0.167. In addition, the Q of 1100 in the S_1 mode is not satisfied. In this work, in order to achieve a larger electromechanical coupling coefficient and a positive group velocity for the S_1 Lamb wave mode, the 4-μm-thick AlN layer and 3-μm-wide finger electrodes are employed in the Lamb wave resonators, creating a normalized AlN thickness (h_{AlN}/λ) equal to 0.333. The experimental results show that the Lamb wave resonator utilizing the S_1 mode presents a Z_{min} = 94 Ω at 1.34 GHz, smaller than the Z_{min} = 224 Ω of that utilizing the S0 mode at 878.3 MHz. In addition, the compensation technique for the Lamb wave resonators using the S_1 mode is explained and the simulation result is presented.

Bibliography

1. G. Piazza, *Piezoelectric Aluminum Nitride Vibrating RF MEMS for Radio Front-End Technology*, Ph. D. dissertation, Department of Electrical Engineering and Computer Science, University of California, Berkeley, California, USA, 2005.
2. C.-M. Lin, *Temperature-Compensated and High-Q Piezoelectric Aluminum Nitride Lamb Wave Resonators for Timing and Frequency Control Applications*, Ph. D. dissertation, Department of Mechanical Engineering, University of California, Berkeley, California, USA, 2013.
3. T.-T. Yen, *Experimental Study of Fine Frequency Selection Techniques for Piezoelectric Aluminum Nitride Lamb Wave Resonators*, M. S. dissertation, Department of Electrical Engineering and Computer Sciences, University of California, Berkeley, California, USA, 2012.
4. C. T.-C. Nguyen, "MEMS technology for timing and frequency control," *IEEE Trans. Ultrason. Ferroelectr. Freq. Control*, vol. 54, pp. 251-270, Feb. 2007.
5. J. Wang, Z. Ren, and C. T.-C. Nguyen, "1.156-GHz self-aligned vibrating micromechanical disk resonator," *IEEE Trans. Ultrason. Ferroelectr. Freq. Control*, vol. 51, pp. 1607-1628, Dec. 2004.
6. V. Yantchev and I. Katardjiev, "Micromachined thin film plate acoustic resonators utilizing the lowest order symmetric Lamb wave mode," *IEEE Trans. Ultrason. Ferroelectr. Freq. Control*, vol. 54, pp. 87-95, Jan. 2007.
7. D. Weinstein and S. A. Bhave, "Internal dielectric transduction in bulk-mode resonators," *J. Microelectromech. Syst.*, vol. 18, pp. 1401-1408, Dec. 2009.
8. S. Gong, N.-K. Kuo, and G. Piazza, "GHz high-*Q* lateral overmoded bulk acousticwave resonators using epitaxial SiC thin film," *J. Microelectromech. Syst.*, vol. 21, pp. 253-255, Apr. 2012.
9. V. Kaajakari, T. Mattila, A. Oja, J. Kiihamäki, and H. Seppä, "Square-extensional mode single-crystal silicon micromechanical resonator for low-phase-noise oscillator applications," *IEEE Electron Device Lett.*, vol. 25, pp.173-175, Apr. 2004.
10. Y.-W. Lin, S. Lee, S.-S. Li, Y. Xie, Z. Ren, and C. T.-C. Nguyen, "Series-resonant VHF micromechanical resonator reference oscillators," *IEEE J. Solid-State Circuits*, vol. 39, pp.2477-2491, Dec. 2004.
11. C. Zuo, J. Van der Spiegel, and G. Piazza, "1.05-GHz CMOS oscillator based on lateral-field-excited piezoelectric AlN contour-mode MEMS resonators," *IEEE Trans. Ultrason. Ferroelectr. Freq. Control*, vol. 57, pp. 82-87, Jan. 2010.

12. M. Rinaldi, C. Zuo, J. Van der Spiegel, and G. Piazza, "Reconfigurable CMOS oscillator based on multi-frequency AlN contour-mode resonators," *IEEE Trans. Electron Devices*, vol. 58, pp. 1281-1286, May 2010.

13. J. Hu, L. Callaghan, R. Ruby, and B. P. Otis, "A 50ppm 600MHz frequency reference utilizing the series resonance of an FBAR," in *Tech. Dig. IEEE Radio Frequency Integrated Circuits Symp.*, 2010, pp.325-328. 151

14. R. C. Ruby, M. Small, F. Bi, D. Lee, L. Callaghan, R. Parker, and S. Ortiz, "Positioning FBAR technology in the frequency and timing domain," *IEEE Trans. Ultrason. Ferroelectr. Freq. Control*, vol. 59, pp. 334-345, Mar. 2012.

15. J. T. M. van Beek and R. Puers, "A review of MEMS oscillators for frequency reference and timing applications," *J. Micromech. Microeng.*, vol. 22, 013001, Jan. 2012.

16. C. T.-C. Nguyen, "Vibrating RF MEMS for next generation wireless applications," in *Proc. IEEE Custom Integrated Circuits Conf.*, 2004, pp. 257-264.

17. S.-S. Li, Y-W. Lin, Z. Ren, and C. T.-C. Nguyen, "Self-switching vibrating micromechanical filter bank," in *Proc. IEEE Intl. Freq. Control Symp.*, 2005, pp. 135-141.

18. S.-S. Li, Y-W. Lin, Z. Ren, and C. T.-C. Nguyen, "A micromechanical parallel-class disk-array filter," in *Proc. IEEE Intl. Freq. Control Symp.*, 2007, pp. 1356-1361.

19. L.-W. Hung and C. T.-C. Nguyen, "*Q*-boosted AlN array-composite resonator with $Q > 10000$," in *Tech. Dig. IEEE Intl. Electron Devices Mtg.*, 2010, pp. 162-165.

20. G. Piazza, P. J. Stephanou, and A. P. Pisano, "Single-chip multiple-frequency AlN MEMS filters based on contour-mode piezoelectric resonators," *J. Microelectromech. Syst.*, vol. 16, pp. 319-328, Apr. 2007.

21. L. Rayleigh, "On waves propagated along the plane surface on an elastic solid," *Proc. London Math. Soc.*, vol. 17, pp. 4-11, Nov. 1885. 152

22. R. M. White and F. W. Voltmer, "Direct piezoelectric coupling to surface elastic waves," *Appl. Phys. Lett.*, vol. 7, pp. 314-316, Dec. 1965.

23. R. Weigel, D. P. Morgan, J. M. Owens, A. Ballato, K. M. Lakin, K. Hashimoto, and C. C. W. Ruppel, "Microwave acoustic materials, devices, and applications," *IEEE Trans. Microw. Theory Tech.*, vol. 50, pp. 738-749, Mar. 2002.

24. P. D. Bradley, R. Ruby, A. Barfknecht, F. Geefay, C. Han, G. Gan, Y. Oshmyansky, and J. D. Larson, m, "A 5 mm x 5 mm x 1.37 mm hermetic FEAR duplexer for PCS handsets with wafer- cale packaging," in *2002 IEEE Ultrasonics Symposium. Proceedings (Cat. No.02CH37388), 2002.*

25. R. Ruby, P. Bradley, J. Larson, m, Y. Oshmyansky, and D. Figueredo, "Ultra miniature high-Q filters and duplexers using FEAR technology," *2001 IEEE Intemational SolidState Circuits Conference. Digest of Technical Papers. ISSCC (Cat. No.01CH37177),* Jan., 2001.

26. R. Lanz and P. Muralt, “Bandpass filters for 8 GHz using solidly mounted bulk acoustic wave resonators,” *IEEE Transactions on Ultrasonics Ferroelectrics and Frequency Control,* vol. 52, pp. 936-946, Jun 2005.

27. W. E. Newell, “Face-mounted piezoelectric resonators,” *Proc. IEEE*, pp. 575-581, Jun. 1965.

28. K. Hashimoto, Ed., *RF Bulk Acoustic Wave Filters for Communications*, Norwood: Artech House, 2009.

29. K. M. Lakin, G. R. Kline and K. T. McCarron, “High-*Q* microwave acoustic resonators and filters,” *IEEE Trans. Microw. Theory Tech.*, vol. 41, pp. 2139-2146, Dec. 1993.

30. K. Toda, “Lamb-wave delay lines with interdigital electrodes,” *J. Appl. Phys.*, vol. 44, pp. 56-62, Jan. 1973.

31. D. S. Ballantine, R. M. White, S. J. Martin, A. J. Ricco, G. C. Frye, E. T. Zellers, and H. Wohltjen, *Acoustic Wave Sensors: Theory, Design, and Physico-Chemical Applications*, San Diego: Academic Press, 1997.

32. R. M. White and S. W. Wenzel, “Fluid loading of a Lamb wave sensor,” *Appl. Phys. Lett.*, vol. 52, pp. 1653-1655, May 1988.

33. S. Gong, and G. Piazza, “Design and analysis of lithium-niobate-based high electromechanical coupling RF-MEMS resonators for wideband filtering,” *IEEE Trans. Microw. Theory Tech.*, vol. 61, pp. 403-414, Jan. 2013.

34. J. Zou, C.-M. Lin, and A. P. Pisano, “Quality factor enhancement in Lamb wave resonators utilizing butterfly-shaped AlN plates”, in *Proc. IEEE Intl. Ultrasonics Symp.*, 2014, pp. 81-84.

35. J. Bjurström, I. Katardjiev, and V. Yantchev, “Lateral-field-excited thin-film Lamb wave resonator,” *Appl. Phys. Lett.*, vol. 86, 154103, Apr. 2005.

36. J. Bjurström, I. Katardjiev, and V. Yantchev, “Thin film Lamb wave resonant structure – the first approach,” *Solid-State Electron.*, vol. 50, pp. 322–326, Mar. 2006.

37. V. Yantchev, J. Enlund, J. Bjurström, and I. Katardjiev, “Design of high frequency piezoelectric resonators utilizing laterally propagating fast modes in thin aluminum nitride (AlN) films,” *Ultrason.*, vol. 45, pp. 208–212, Dec. 2006.

38. V. Yantchev, L. Arapan, and I. Katardjiev, “Micromachined thin film plate acoustic resonators (FPAR): Part II,” *IEEE Trans. Ultrason. Ferroelect. Freq. Control*, vol. 56, pp. 2701–2710, Dec. 2009.

39. P. J. Stephanou and A. P. Pisano, “800 MHz low motional resistance contour extensional aluminum nitride micromechanical resonators,” in *Tech. Dig. Solid-State Sens. Actuators Microsyst. Workshop*, pp. 60-61.

40. G. Piazza, P. J. Stephanou, and A. P. Pisano, "One and two port piezoelectric higher order contour-mode MEMS resonators for mechanical signal processing," *Solid-State Electron.*, vol. 51, pp. 1596-1608, Nov.-Dec. 2007.

41. M. Rinaldi, C. Zuniga, C. Zuo, and G. Piazza, "Super-high-frequency two-port AlN contour-mode resonators for RF applications," *IEEE Trans. Ultrason. Ferroelect. Freq. Control*, vol. 57, pp. 38-45, Jan. 2010.

42. C. Zuo, N. Sinha, J. Van der Spiegel, and G. Piazza, "Multifrequency Pierce oscillator based on piezoelectric AlN contour-mode MEMS technology," *J. Microelectromech. Syst.*, vol. 19, pp. 570-580, Jun. 2010.

43. C.-M. Lin, Y.-J. Lai, T.-T. Yen, J.-C. Hsu, Y.-Y. Chen, D. G. Senesky, and A. P. Pisano, "Quality factor enhancement in Lamb wave resonators utilizing AlN plates with convex edges," in *Tech. Dig. Intl. Conf. Solid-State Sens. Actuators Microsyst.*, 2011, pp. 1512-1515.

44. C.-M. Lin, Y.-J. Lai, J.-C. Hsu, Y.-Y. Chen, D. G. Senesky, and A. P. Pisano, "High-*Q* aluminum nitride Lamb wave resonators with biconvex edges," *Appl. Phys. Lett.*, vol. 99, 143501, Oct. 2011.

45. V. Yantchev and I. Katardjiev, "Thin film Lamb wave resonators in frequency control and sensing applications: a review," *J. Micromech. Microeng.*, vol. 23, 043001, Apr. 2013.

46. G. Piazza, P. J. Stephanou, and A. P. Pisano, "Piezoelectric aluminum nitride vibrating contour-mode MEMS resonators," *J. Microelectromech. Syst.*, vol. 15, pp. 1406-1418, Dec. 2006.

47. C.-M. Lin, V. Yantchev, Y.-Y. Chen, V. V. Felmetsger, and A. P. Pisano, "Characteristics of AlN Lamb wave resonators with various bottom electrode configurations," in *Proc. IEEE Intl. Freq. Control Symp.–Eur. Freq. Time Forum*, 2011, pp. 505-509.

48. I. A. Viktorov, *Rayleigh and Lamb Waves: Physical Theory and Applications*, New York: Plenum Press, 1967.

49. G. Wingqvist, L. Arapan, V. Yantchev, and I. Katardjiev, "A micromachined thermally compensated thin film Lamb wave resonator for frequency control and sensing applications," *J. Micromech. Microeng.*, vol. 19, 035018, Mar. 2009.

50. M. A. Schmidt and R. T. Howe, "Silicon resonant microsensors," *Ceram. Eng. Sci. Proc.*, vol. 8, pp. 1019-1034, Oct. 1987.

51. W. C. Tang, T.-C. H. Nguyen, and R. T. Howe, "Laterally driven polysilicon resonant microstructures," *Sens. Actuators*, vol. 20, pp. 25-32, Nov. 1989.

52. F. D. Bannon III, J. R. Clark, and C. T.-C. Nguyen, "High-Q HF microelectromechanical filters," *IEEE Journal of Solid-State Circuits*, vol. 35, pp. 512-526, Apr. 2000.

53. C. T.-C. Nguyen and R. T. Howe, "An integrated CMOS micromechanical resonator high-*Q* oscillator," *IEEE J. Solid-State Circuits*, vol. 34, pp.440-455, Apr. 1999.

54. J. R. Clark, W.-T. Hsu, and C. T.-C. Nguyen, "High-*Q* VHF micromechanical contour-mode disk resonators," in *Tech. Dig. IEEE Intl. Electron Devices Mtg.*, 2000, pp. 493-496.

55. J. R. Clark, W.-T. Hsu, M. A. Abdelmoneum, and C. T.-C. Nguyen, "High-*Q* UHF micromechanical radial-contour mode disk resonators," *J. Microelectromech. Syst.*, vol. 14, pp. 1298-1310, Dec. 2005.

56. B. A. Auld, *Acoustic Fields and Waves in Solids*, New York: Wiley, 1973.

57. H. Iwanaga, A. Kunishige, and S. Takeuchi, "Anisotropic thermal expansion in wurtzite-type crystals," *J. Mater. Sci.*, vol. 35, pp. 2451-2454, May 2000.

58. C. Galassi, Ed., *Piezoelectric Materials Advances in Science Technology and Applications,* Springer Netherlands, 2000.

59. T. Ikeda, *Fundamentals of Piezoelectricity*, Oxford University Press, 1990.

60. K. Tsubouchi, K. Sugai and N. Mikoshiba, "AIN material constants evaluation and SAW properties on AIN/Al_2O_3 and AlN/Si," *IEEE Ultrasonics Symposium Proceedings,* pp. 375-380, 1981.

61. K. Tsubouchi and N. Mikoshiba, "Zero-temperature-coefficient SAW devices on AlN epitaxial films," *IEEE Trans. Sonics Ultrason.*, vol. SU-32, pp. 634-644, Sep. 1985.

62. L. E. McNeil, M. Grimsditch, and R. H. French, "Vibrational spectroscopy of aluminum nitride," *J. Am. Ceram. Soc.*, vol. 76, pp. 1132-1136, May 1993.

63. J. F. Rosenbaum, *Bulk Acoustic Wave Theory and Devices,* Artech House, Inc., 1988.

64. K. Hashimoto, *Surface Acoustic Wave Devices in Telecommunications: Modelling and Simulation*, Germany: Springer-Verlag, 2000.

65. S. G. Joshi and Y. Jin, "Excitation of ultrasonic Lamb waves in piezoelectric plates," *J. Appl. Phys.*, vol. 69, pp. 8018-8024, Jun. 1991.

66. J. H. Kuypers and A. P. Pisano, "Green's function analysis of Lamb wave resonators," in *Proc. IEEE Int. Ultrasonics Symp.*, 2008, pp. 1548-1551.

67. Y.-Y. Chen, "Exact analysis of Lamb waves in piezoelectric membranes with distinct electrode arrangements," *Jpn. J. Appl. Phys.*, vol. 48, art. no. 07GA06, Jul. 2009.

68. C.-M. Lin, T.-T. Yen, Y.-J. Lai, V. Felmetsger, M. A. Hopcroft, J. H. Kuypers, and A. P. Pisano, "Temperature-compensated aluminum nitride Lamb wave resonators," *IEEE Trans. Ultrason. Ferroelect. Freq. Control*, vol. 57, pp. 524-532, Mar. 2010

69. J Bjurström, G Wingqvist, V Yantchev and I Katardjiev, "Temperature compensation of liquid FBAR sensors," *J. Micromech. Microeng.*, vol. 17, pp. 651-658, Mar. 2007.

70. J. D. Larson, P. D. Bradley, S. Wartenberg, and R. C. Ruby, "Modified Butterworth-Van Dyke circuit model for FBAR resonators and automated measurement system," in *Proc. IEEE Int. Ultrason. Symp.*, 2000, pp. 863–868.

71. R. Aigner, "Bringing BAW technology into volume production the ten commandments and the seven deadly sins," in *Proc. 3rd Int. Symp. Acoust. Wave Devices Future Mobile Commun. Syst.*, 2007, pp. 85–91.

72. C. -M. Lin, V. Yantchev, J. Zou, and A. P. Pisano, "Micromachined one-port aluminum nitride Lamb wave resonators utilizing the lowest-order symmetric mode," *J. Microelectromech. Syst.*, vol. 23, pp. 78-91, Feb. 2014.

73. J. H. Kuypers, C.-M. Lin, G. Vigevani, and A. P. Pisano, "Intrinsic temperature compensation of aluminum nitride Lamb wave resonators for multiple-frequency references," in *Proc. IEEE Int. Frequency Control Symp.*, 2008, pp. 240–249

74. J. Zou, C.-M., Y.-Y. Chen, and A. P. Pisano, "Theoretical study of thermally stable SiO_2/AlN/SiO_2 Lamb wave resonators at high temperatures, " *J. Appl. Phys.*, vol. 115, 094510, Mar. 2014.

75. N. Dewan, K. Sreenivas, and V. Gupta, "Anomalous elastic properties of RF sputtered amorphous TeO_{2+x} thin film for temperature-Stable SAW device applications," *IEEE Trans. Ultrason. Ferroelect. Freq. Control*, vol. 55, pp. 552-558, Mar. 2008.

76. W. Pan and F. Ayazi, "Thin-film piezoelectric-on-substrate resonators with *Q* enhancement and TCF reduction," in *Tech. Dig. IEEE Intl. Conf. Micro Electro Mech. Syst.*, 2010, pp. 727–730.

77. A. K. Samarao and F. Ayazi, "Temperature compensation of silicon resonators via degenerate doping," *IEEE. Trans. Electron Devices*, vol. 59, pp. 87–93, Jan. 2012.

78. S. Matsuda, M. Hara, M. Miura, T. Matsuda, M. Ueda, Y. Satoh, and K. Hashimoto, "Use of fluorine-doped silicon oxide for temperature compensation of radio frequency surface acoustic wave devices," *IEEE Trans. Ultrason. Ferroelect. Freq. Control*, vol. 59, pp. 135-138, Jan. 2012.

79. V. V. Felmetsger, P. N. Laptev, and S. M. Tanner, "Innovative technique for tailoring intrinsic stress in reactively sputtered piezoelectric aluminum nitride films," *J. Vac. Sci. Technol. A*, vol. 27, pp. 417-422, May-Jun. 2009.

80. M. Ohring, *Materials Science of Thin Films*, Academic Press, 2011.

81. http://nanolab.berkeley.edu/.

82. Auld, B.A., *Acoustic Fields and Waves in Solids, Vol. 2*, Krieger Publishers, 1990.

83. J. Segovia-Fernandez, N.-K. Kuo, and G. Piazza, "Impact of metal electrodes on the figure of merit (kt 2 ·Q) and spurious modes of contour mode AlN resonators," ," in *Proc. IEEE Int. Ultrasonics Symp.*, 2012, pp. 299-302.

84. T. Yokoyama, T. Nishihara, S. Taniguchi, M. Iwaki, and Y. Satoh, "New electrode material for low-loss and high-Q FBAR filters," in *Proc. IEEE Int. Ultrasonics Symp.*, 2004, pp. 429-432.

85. G. F. Iriarte, J. Bjurstrom, J. Westlinder, F. Engelmark, and I. V. Katardjiev, "Synthesis of c-axis-oriented AlN thin films on high-condcuting layers: Al, Mo, Ti, TiN, and Ni," *IEEE Trans. Ultrason. Ferroelectr. Freq. Control*, vol. 52, pp. 1170-1174, Jul. 2005.

86. M. Ueda, T. Nishihara, J. Tsutsumi, S. Taniguchi, T. Yokoyama, S. Inoue, T. Miyashita, and Y. Satoh, "High-Q resonators using FBAR/SAW technology and their applications," *IEEE Microwave Symp.*, 2005, pp. 209-212.

87. E. Iborra, M.Clement, J. Olivares, J. Sangrador, N. Rimmer and A. Rastogi, "Aluminum nitride bulk acoustic wave devices with iridium bottom electrodes," in *Proc. IEEE Int. Ultrasonics Symp.*, 2007, pp. 616-619.

88. C.-M. Lin, Y.-Y. Chen, V. V. Felmetsger, D. G. Senesky, and A. P. Pisano, "AlN/3C-SiC composite plate enabling high-frequency and high-Q micromechanical resonators," *Adv. Mater.*, vol. 24, pp. 2722-2727, May 2012.

89. S. Ghaffari, S. A. Chandorkar, S. Wang, E. J. Ng, C. H. Ahn, V. Hong, Y. Yang, and T. W. Kenny, "Quantum limit of quality factor in silicon micro and nano mechanical resonators," *Sci. Rep.*, vol. 3, 3244, Nov. 2013.

90. Z. Hao and B. Liao, "An analytical study on interfacial dissipation in piezoelectric rectangular block resonators with in-plane longitudinal mode vibrations," *Sens. Actuators A: Phys.*, vol. 163, pp.401-409, Sep. 2010.

91. T.-T. Yen, A. P. Pisano, and C. T.-C. Nguyen, "High-Q capacitive-piezoelectric AlN Lamb wave resonators," in *Proc. IEEE Int. Conf. Micro Electro Mech. Syst.*, 2013, pp. 114-117.

92. A. Frangia, M. Cremonesia, A. Jaakkolab, and T. Pensala, "Analysis of anchor and interface losses in piezoelectric MEMS resonators," *Sens. Actuators A: Phys.*, vol. 190, pp.127-135, Feb. 2013.

93. L. Wu, M. Akgul, Z. Ren, Y. Lin, W.-C. Li, and C. T.-C. Nguyen, "Hollow stems for higher micromechanical disk resonator quality factor", in *Proc. IEEE Intl. Ultrason. Symp.*, 2011, pp. 1964-1967.

94. W. Pang, H. Zhang, S. Whangbo, and E.S. Kim, "High Q film bulk acoustic resonator from 2.4 to 5.1 GHz," in *Proc. IEEE Int. Conf. Micro Electro Mech. Syst.*, 2004, pp. 805-808.

95. B. P. Harrington and R. Abdolvand, "In-plane acoustic reflectors for reducing effective anchor loss in lateral-extensional MEMS resonators," *J. Micromech. Microeng.*, vol. 21, 085021, Aug. 2011.

96. C.-M. Lin, Y.-J. Lai, J.-C. Hsu, Y.-Y. Chen, D. G. Senesky, and A. P. Pisano, "High-Q aluminum nitride Lamb wave resonators with biconvex edges," *Appl. Phys. Lett.*, vol. 99, 143501, Oct. 2011.

97. J. Zou, C.-M. Lin, and A.P. Pisano, "Anchor loss suppression using butterfly-shaped plates for AlN Lamb wave resonators," in *Proc. IEEE Int. Freq. Contr. Symp. & the Eur. Freq. Time Forum (FCS).*, 2015, pp. 432-435.

98. Y.-Y. Chen, Y.-T. Lai, and C.-M. Lin, "Finite element analysis of anchor loss in AlN Lamb wave resonators," in *Proc. IEEE Int. Freq. Contr. Symp.*, 2014, pp. 132-136.

99. C. Cassella, J. S. Fernandez, M. Cremonesi, A. Frangi, and G. Piazza, "Reduction of anchor losses by etched slots in aluminum nitride contour mode resonators," in *Proc. Eur. Freq. Time Forum & IEEE Int. Freq. Contr. Symp.*, 2013, pp. 926-929.

100. C.-M. Lin, J.-C. Hsu, D. G. Senesky, and A. P. Pisano, "Anchor loss reduction in AlN Lamb wave resonators using phononic crystal strip tethers", in *Proc. IEEE Int. Freq. Contr. Symp.*, 2014, pp. 371-375.

101. D. S. Bindel and S. Govindjee, "Elastic PMLs for resonator anchor loss simulation," *Int. J. Numer. Meth. Engng.*, vol. 64, pp. 798-818, Oct. 2005.

102. R. C. Turner, P. A. Fuierer, R. E. Newnham, and T. R. Shrout, "Materials for high temperature acoustic and vibration sensors: A Review," *Appl. Acoust.*, vol. 41, pp. 299-324, Issue 4, 1994.

103. C.-M. Lin, W.-C. Lien, V. V. Felmetsger, M. A. Hopcroft, D. G. Senesky, and A. P. Pisano, "AlN thin films grown on epitaxial 3C-SiC (100) for piezoelectric resonant devices," *Appl. Phys. Lett.*, vol. 97, 141907, Oct. 2010.

104. P. M. Davulis and M. Pereira da Cunha, "High-temperature langatate elastic constants and experimental validation up to 900°C," *IEEE Trans. Ultrason. Ferroelectr. Freq. Control*, vol. 57, pp. 59-65, Jan. 2010.

105. T. Aubert, J. Bardong, O. Legrani, O. Elmazria, M. B. Assouar, G. Bruckner, and A. Talbi, "In situ high-temperature characterization of AlN-based surface acoustic wave devices," *J. Appl. Phys.*, vol. 114, 014505, Jul. 2013.

106. C.-M. Lin, Y.-Y. Chen, V. V. Felmetsger, W.-C. Lien, T. Riekkinen, D. G. Senesky, and A. P. Pisano, "Surface acoustic wave devices on AlN/3C–SiC/Si multilayer structures," *J. Micromech. Microeng.*, vol. 23, 025019, Jan. 2013.

107. T.-T. Yen, C.-M. Lin, X. Zhao, V. V. Felmetsger, D. G. Senesky, M. A. Hopcroft, and A. P. Pisano, "Characterization of aluminum nitride Lamb wave resonators operating at 600°C for harsh environment RF applications," in *Proc. IEEE Int. Conf. Micro Electro Mech. Syst.*, 2010, pp. 731-734.

108. C.-M. Lin, T.-T. Yen, V. V. Felmetsger, M. A. Hopcroft, J. H. Kuypers, and A. P. Pisano, "Thermal compensation for aluminum nitride Lamb wave resonators operating at high temperature," in *Proc. IEEE Int. Freq. Contr. Symp.*, 2010, pp. 14-18.

109. C.-M. Lin, T.-T. Yen, V. V. Felmetsger, M. A. Hopcroft, J. H. Kuypers, and A. P. Pisano, "Thermally compensated aluminum nitride Lamb wave resonators for high temperature applications," *Appl. Phys. Lett.*, vol. 97, 083501, Jul. 2010.

110. C.-M. Lin, T.-T. Yen, Y.-J. Lai, V. V. Felmetsger, M. A. Hopcroft, J. H. Kuypers, and A. P. Pisano, "Experimental study of temperature-compensated aluminum nitride Lamb wave resonators," in *Proc. IEEE Intl. Freq. Contr. Symp. & Eur. Freq. Time Forum*, 2009, pp. 5–9.

111. A. Artieda and P. Muralt, "High-Q AlN/SiO_2 symmetric composite thin film bulk acoustic wave resonators," *IEEE Trans. Ultrason. Ferroelectr. Freq. Control*, vol. 55, 2463-2468, Nov. 2008.

112. J. Zou, C.-M. Lin, D. G. Senesky, and A. P. Pisano, "Thermally stable SiO_2/AlN/SiO_2 Lamb wave resonators utilizing the lowest-order symmetric mode at high temperatures," in *Proc. IEEE Intl. Ultrason. Symp.*, 2013, pp. 1077–1080.

113. E. L. Adler, "Matrix methods applied to acoustic waves in multilayers," *IEEE Trans. Ultrason. Ferroelectr. Freq. Control*, vol. 37, pp. 485-490 1990.

114. C.-M. Lin, Y.-Y. Chen, and A. P. Pisano, "Theoretical investigation of Lamb wave characteristics in AlN/3C-SiC composite membranes" *Appl. Phys. Lett.*, vol. 97, 193506, Nov. 2010.

115. C.-M. Lin, Y.-Y. Chen, V. V. Felmetsger, G. Vigevani, D. G. Senesky, and A. P. Pisano, "Micromachined aluminum nitride acoustic resonators with an epitaxial silicon carbide layer utilizing high-order Lamb wave modes," in *Proc. IEEE Int. Conf. Micro Electro Mech. Syst.*, 2012, pp. 733–736.

116. F. Di Pietrantonio, M. Benetti, D. Cannata, R. Beccherelli, and E. Verona, "Guided lamb wave electroacoustic devices on micromachined AlN/Al plates," *IEEE Trans. Ultrason. Ferroelectr. Freq. Control*, vol. 57, 1175-1182, May 2010.

117. G. Bu, D. Ciplys, M. Shur, L. J. Schowalter, S. Schujman, and R. Gaska, "Surface acoustic wave velocity in single-crystal AlN substrates," *IEEE Trans. Ultrason. Ferroelectr. Freq. Control*, vol. 53, pp. 251-254, Jan. 2006.

118. V. Yantcheva and I. Katardjiev, "Quasistatic transduction of the fundamental symmetric Lamb mode in longitudinal wave transducers," *Appl. Phys. Lett.*, vol. 88, 214101, May 2006.

119. Q. Zou, D. Lee, F. Bi, R. Ruby, M. Small, S. Ortiz, Y. Oshmyansky, and J. Kaitila, "High coupling coefficient Temperature compensated FBAR resonator for oscillator application with wide pulling range," in *Proc. of IEEE Intl. Freq. Contr. Symp.*, 2010, pp. 646-651.

120. T.-T. Yen, C.-M. Lin, Y.-J. Lai, D. Wittwer, M. A. Hopcroft, and A. P. Pisano, "Fine frequency selection techniques for aluminum nitride Lamb wave resonators", in *Proc. IEEE IEEE Int. Freq. Contr. Symp.*, 2010, pp. 9–13.

121. J. Zou, C.-M. Lin, Y.-Y. Chen, and A. P. Pisano, "High-frequency and low-resonance-impedance Lamb wave resonators utilizing the S1 mode," in in *Tech. Dig. Intl. Conf. Solid-State Sens. Actuators Microsyst. (Transducers)*, 2015.

122. M. Rinaldi, C. Zuniga, C. Zuo, and G. Piazza, “Super-high-frequency two-port AlN contour-mode resonators for RF applications”, *IEEE Trans. Ultrason. Ferroelectr. Freq. Control*, vol. 57, pp. 38-45, Jan. 2010.

123. V. Yantchev, L. Lilia, I. Katardjiev, and V. Plessky, “Thin- film zero-group-velocity Lamb wave resonator”, *Appl. Phys. Lett.*, vol. 99, 033505, Jul. 2011.

124. R. A. Schneider and C. T.-C. Nguyen, “On/off switchable high-Q capacitive-piezoelectric AlN resonators”, in *Proc. IEEE Int. Conf. Micro Electro Mech. Syst.*, San Francisco, CA, Jan. 2014, pp. 1265-1268.